

**Exploring the Interaction of Light and Matter on an
Ultrafast Timescale Using Plasma Spectroscopy**

BY

JOHN S. PENCZAK
B.S., Illinois State University, 2006

THESIS

Submitted as partial fulfillment of the requirements
for the degree of Doctor of Philosophy in Physical Chemistry
in the Graduate College of the
University of Illinois at Chicago, 2013

Chicago, Illinois

Defense Committee:

Robert Gordon, Chair and Advisor
Timothy Keiderling, Physical Chemistry
Richard Schaller, Argonne National Lab
Preston Snee, Physical Chemistry
Michael Trenary, Physical Chemistry

*To my fiancée, Heather, and my children, Alexandria and Cameron,
whose love and inspiration give endless motivation to succeed*

ACKNOWLEDGEMENTS

I would first like to thank my advisor, Dr. Robert Gordon, for his ceaseless support and prolific insight, guidance, and instruction that made the completion of this research and thesis possible. I would also like to thank Dr. Richard Schaller for all the help he gave in conducting experiments in his lab at Argonne National Laboratory that provided an important new perspective to problems we had been studying for so long. I would also like to thank the rest of the members of my thesis defense committee Dr. Timothy Kiederling, Dr. Michael Trenary, and Dr. Preston Snee for their support, guidance, and inspiring lectures, as well as the rest of the UIC faculty, who so often helped every step along the way. I'm am extremely grateful to the people that have helped me in the lab, Dr. Yaoming Liu, Dr. Sima Singha, and Dr. Youbo Zhao, providing hands-on assistance and training in all of the different aspects of our research.

TABLE OF CONTENTS

<u>CHAPTER</u>	<u>PAGE</u>
I. INTRODUCTION TO THE INTERACTION OF LIGHT AND MATTER	1
1.1 Introduction.....	1
1.2 Creating Intense Femtosecond Pulses.....	4
1.3 Single-Particle Interaction with Electromagnetic Waves	8
1.4 Ionization of Matter Using Electromagnetic Radiation	10
1.5 Plasma Generation	14
1.6 Plasma Hydrodynamics	17
1.7 Plasma Absorption Mechanisms.....	20
1.8 Thermal Processes	30
II. Mechanism for Continuum Polarization in Laser-Induced Breakdown Spectroscopy of Si(111).....	33
2.1 Introduction.....	33
2.2 Experimental Methods	36
2.3 Results.....	40
2.4 Discussion.....	52
III. Investigation of Second Harmonic Generation in Laser Produced Plasmas Using Dual Femtosecond Pulses.....	61
3.1 Introduction.....	61
3.2 Experimental Methods	67
3.3 Results.....	69
3.4 Discussion.....	80
IV. Femtosecond Laser-Induced Breakdown Spectroscopy Using Temporally Delayed Pulses	88
3.1 Introduction.....	88
3.2 Experimental Methods	90
3.3 Results.....	91
3.4 Discussion.....	105
CONCLUSION	111
CITED LITERATURE	113
VITA	125

LIST OF TABLES

<u>TABLE</u>		<u>PAGE</u>
I.	ELECTRONIC TRANSITIONS OF SILICON	42
II.	ELECTRONIC TRANSITIONS OF ALUMINUM AND SILVER.....	94
III.	ADDITIONAL ELECTRONIC TRANSITIONS OF SILVER.....	96

LIST OF FIGURES

<u>FIGURE</u>	<u>PAGE</u>
1. Schematic drawing of the experimental apparatus for LIBS polarization experiment	37
2. LIB spectra with s- and p-polarized femtosecond laser using polarizer to block s- or p-polarized emission.....	41
3. LIB spectra with s- and p-polarized nanosecond laser using polarizer to block s- or p-polarized emission.....	42
4. Malus plot of signal intensity at 460 nm versus polarizer angle.....	45
5. Polarization and polarization angle spectra using s- and p-polarized femtosecond laser	46
6. Polarization and polarization angle spectra using s- and p-polarized nanosecond laser	47
7. Time-resolved data taken at Argonne National Lab of signal intensity, polarization, and polarization angle.....	50
8. Fluence dependence of the polarization using s- and p-polarized nanosecond laser.....	51
9. Schematic drawing of the reflected and directly detected plasma emission.....	53
10. Polarization of the 488 nm emission as a function of detection angle, theoretical reflectivity, and predicted polarization	57
11. Polarization spectrum comparison to calculated wavelength dependence.....	58
12. Schematic drawing of the experimental apparatus for SHG experiment	68
13. SH signal intensity dependence on delay between double pulses detected at the specular and 30° from the specular angle	70
14. SH signal intensity dependence on delay between double pulses with BK7 glass target	71
15. Ratio of SH signal intensity using double or single pulses of varying intensity.....	72
16. Intensity dependence of the optimum delay for SH emission.....	73
17. Intensity dependence of the SH signal intensity for single and double pulses detected at the specular angle, and double pulses detected at 30° from the specular angle.....	75
18. Angular distribution of the SH emission.....	77
19. Intensity dependence of the SH emission divergence angle for s- and p-polarized pulses.....	78
20. Intensity dependence of the wavelength shift of the SH emission.....	79
21. SH emission wavelength shift versus double pulse delay for s- and p-polarized pulses	80

LIST OF FIGURES(continued)

<u>FIGURE</u>		<u>PAGE</u>
22.	Fluence dependence of the LIB signal for Al and Ag.....	92
23.	Comparison of LIB spectra using single pulses or double pulses with 104 ps delay	94
24.	LIB spectra using s- and p-polarized single or double pulses with 104 ps delay	96
25.	Enhancement ratio of Al and Ag spectral lines versus delay.....	98
26.	Fluence dependence of the maximum enhancement ratio for Al and Ag	99
27.	Enhancement ration versus delay for pure Al.....	101
28.	Fluence dependence of the maximum enhancement ratio for Al and Ag in the low fluence regime.....	101
29.	Fluence dependence of the time constant for enhancement ratio as a function of delay	103
30.	Comparison of LIB spectra of Ag/Al bilayer using double pulses with a delay of 104 ps or >1 s	104

LIST OF ABBREVIATIONS

ANL	Argonne National Laboratory
AOM	Acoustic-Optic Modulator
ATI	Above Threshold Ionization
BSI	Barrier Suppression Ionization
CPA	Chirped Pulse Amplification
FS	Femtosecond
FWHM	Full Width at Half Maximum
LIBS	Laser-Induced Breakdown Spectroscopy
MPI	Multi-Photon Ionization
NIST	National Institute of Standards and Technology
NS	Nanosecond
OFI	Optical Field Ionization
OTBI	Over-the-Barrier Ionization
PIC	Particle-in-Cell
PS	Picosecond
RA	Resonant Absorption
SHG	Second Harmonic Generation
TI	Tunnel Ionization
UIC	University of Illinois at Chicago

SUMMARY

Shortly after the invention of the laser, spectroscopists began evaluating its potential uses. Early experiments showed that a laser could create a plasma, and that the light given off by this plasma could be used for analytical detection. This founded the basis for laser-induced breakdown spectroscopy (LIBS), but the fundamental processes occurring, such as absorption, ablation, and a variety of complex plasma processes, are still under experimental scrutiny today. The LIBS technique is an important analytical tool used in a variety of analytical applications in industries such as hazardous chemicals detection, art, environmental, metallurgy, and it has even been used on the 2009 Mars rover. The development of intense, sub-picosecond lasers has created a new realm of study concerning the interaction of light and matter. The basic characteristics of this interaction include the rapid ionization of matter, resulting in plasma formation, the interaction of the laser with this plasma, and the deposition of energy into a material on a timescale shorter than the thermal relaxation of the system. In this thesis, a theoretical discussion is first presented to familiarize the reader with the fundamental properties of the interaction of light and matter. The subsequent experimental sections include collection of studies attempting to elucidate some of the mechanisms for the phenomena that occur during this interaction under the extreme conditions of a ~ 50 fs laser pulse, with an intensity ranging from 10^{13} - 10^{16} W/cm², by spectroscopically analyzing the light given off by the plasma. Further attention is given to the interaction of the light with the laser-generated plasma itself, which dictates the development of many of the different processes.

In the first experiment, the light emitted from the plasma, either in the form of discrete electronic transitions, or a continuum background, is analyzed to determine the mechanism for

SUMMARY (continued)

the partial polarization of the continuum emission. It is found that the continuum background is polarized up to ~20% depending on the intensity and angle of incidence of the incident laser, along with wavelength and detection geometry of the emitted light. This polarization is shown to be due to a reflection of a fraction of the plasma emission at the liquid surface of the target, following the Fresnel formulae, which predict a preferential reflection of s-polarized light, dependent on the aforementioned parameters.

The next experiment deals exclusively with the interaction of the laser with the plasma. In this experiment, the laser pulse is split into two sub-pulses, separated in time by a variable delay up to ~100 ps, such that the second pulse is able to interact with a plasma at different stages of its development. The second harmonic of the fundamental laser radiation is monitored as a function of pulse delay and intensity to determine the optimum plasma conditions for the generation of this second harmonic emission. It is found that two such maxima exist, corresponding to two different mechanisms for the second harmonic generation, preferring very different electron densities, providing a means of studying the evolution of the plasma.

Finally, the last set of experiments focuses on the ablation efficiency and plasma emission signal intensity, to determine the mechanism for dual-pulse material ablation, again using temporally-delayed pulses, up to ~100 ps. It is found that the signal intensity increases significantly as the time between the pulses is increased, but that this is not a result of an increase in ablated material. Instead, the increase in signal intensity is explained by the second pulse interacting with and “reheating” the plasma, resulting in an increase in the number density of excited species, and an increase in the temperature of the plasma allowing a longer lifetime of emission.

1. Introduction to the Interaction of Light and Matter

1.1 Introduction

The idea of light, its properties, and its interaction with the world around us, have intrigued countless scientific minds. From the beginning of recorded history, people have strived to understand exactly what light is. The ancient Greeks initiated the study of geometrical optics, explaining the reflection of light and the casting of shadows in terms of rays. Much later, in the seventeenth century, Snell's deduction of the law of refraction and Newton's demonstration of the dispersion of different frequencies of light founded the basis of geometrical optics. The debate then turned to whether light should be described in terms of the corpuscular theory, proposed by Pierre Gassendi and developed by Newton, in which light is made of tiny discrete particles, or if light should be considered a wave as theorized by Huygens. Coulomb's law for point charges and magnetic dipoles was established in the eighteenth century, as well as the idea that electric current was due to the movement of electric charges. The nineteenth century was a period of great discoveries concerning light, starting with Thomas Young's proposal of the principles of interference and diffraction based on the wave theory of light. Malus and Brewster developed the ideas of polarization by reflection, and Fresnel completed a more comprehensive theory of diffraction. At this point, when the wave theory had been firmly established, light was still thought to be a longitudinal wave, and it was not until 1817, when Thomas Young proposed that light was made up of purely transverse waves, that the different theories started to fit together. Shortly after, the works of Oersted, Ampere, and Faraday helped to connect the phenomena of electricity, magnetism, and optics, which were rigorously expressed in mathematical terms by Maxwell [1, 2].

The discovery of the electron in 1897 by J. J. Thomson, and Lorentz's subsequent development of the theory of electromagnetism, based on the microscopic properties of atoms containing elastically bound electrons, completed the classical description of light. The work of Planck, Einstein, Compton, as well as many others, helped to develop the quantum theory of light, including its wave-particle duality, which describes the current understanding of light we have today.

In the twentieth century, the different branches of scientific study concerning light grew rapidly. Two of these branches are of particular interest to this thesis. The first is the interaction of intense electromagnetic radiation with matter, exemplified by experiments like those of Volkov [3], who used the idea of a "dressed state" to describe the inertia of an electron oscillating in an electromagnetic field, or Schwinger [4], who analyzed the radiation produced by electrons accelerated in a synchrotron. The second, and more pertinent branch, is related to the study of plasmas.

Irving Langmuir compared the fluid in the blood left over after removal of corpuscular material, known as plasma, to the entraining medium of the particles within an ionized gas, hence coining the term. Unfortunately, this name was a misnomer since no actual substance exists other than the electrons, ions, and neutral atoms of this ionized gas. Research in the field of plasma science was motivated by the propagation of radio waves in the ionospheric plasma as well as the gaseous electron tubes used in electronics. The theory of hydromagnetic waves was proposed by Hannes Alfvén [5] in the 1940s, and work by researchers such as Akheizer, Polovin, Dawson, and Davidson provided the fundamental basis for the interaction of high-intensity electromagnetic waves in plasmas and the behavior of large-amplitude electrostatic plasma waves. After the invention of the laser in the 1960's, the ability to create and study plasmas and

their interaction with light became much more available, and research in the field became even more diverse. One of the driving forces for these studies was the idea of inertially confined fusion, proposed by Nuckolls in 1972 [6], which suggested that fusion could be accomplished by the compression of micrometer-sized pellets of deuterium and tritium, using ultra-intense laser beams focused symmetrically onto its surface. Forty years later, scientists are still trying to make this technology commercially practical, and they remain optimistic that it can become a viable energy source.

The invention of ultrashort pulse lasers, usually defined as having a time span on the order of femtoseconds (10^{-15} s), renewed interest in the field of plasma science, due to the fact that these pulses can create a plasma with electron densities near that of a solid and interact with this plasma before it has significant time to expand. The interaction of light with matter, the creation of plasmas, and the subsequent interaction of light with that plasma has provided an abundance of scientific explorations in a wide variety of applications that span all types of fields including, industry, medicine, military, astronomy, energy production, as well as a diverse assortment of fundamental scientific projects [7].

The previous discussion is in no way meant to provide a comprehensive history of the study of light or plasmas, as such a description would fill many volumes, just as the books containing these findings could fill nearly endless shelves. Instead, this thesis intends to concentrate on a concise collection of phenomena all related by the concepts of plasma science. The remainder of the first chapter of this thesis will serve as an attempt to introduce the fundamental concepts involved in the interaction of intense, ultrashort light and matter, and the properties of a laser-produced plasma. The subsequent, experimentally-based, chapters will focus on explaining some of the specific areas encountered in this complex field. Chapter 2

explores the properties of light emitted from plasmas, concentrating on the characterization of its spectral and polarization features. The third chapter focuses on the interaction of light with an expanding plasma and the ability to generate second harmonic radiation from the fundamental beam. Finally, Chapter 4 attempts to further understand the mechanisms of dual-pulse laser ablation and the role of plasma formation in this process.

1.2 Creating Intense Femtosecond Pulses

Before delving into the complex processes that occur when intense, ultrashort electromagnetic radiation interacts with matter, it is instructive to present a brief description of how this light is generated. The basic theoretical considerations for the laser were outlined by Einstein [8] in 1917, where he described the process as being based on the probability coefficients (Einstein coefficients) of absorption, spontaneous emission, and stimulated emission of electromagnetic radiation. In short, the absorption of light by an atomic system is governed by some probability that is characteristic of the system. Absorption of the radiation can cause an electronic transition, promoting an electron to an excited state, E_2 . The excited atom can then decay spontaneously to a lower level, E_1 , emitting a photon with energy equal to the difference in the energy of the two states ($E_2 - E_1$). This process results in emission of a photon with frequency, ν_{12} , corresponding to the transition ($h\nu_{12} = E_2 - E_1$). The photons created through this process have no definite relationship of phase or direction with one another. The atom can also decay non-radiatively, with the energy of the transition being lost in some other way (e.g. transferring kinetic energy to another atom by collision). Alternatively, an excited atom can be stimulated to decay by a photon with a frequency, ν_{12} , resulting in the emission of a pair of photons that are identical to the incident one in phase, frequency, and direction. The ability to

amplify the light emission, i.e. creating a laser, is dependent on having a larger number of atoms in the excited state rather than in the lower state, known as a population inversion.

Laser technology has come a long way since Einstein's theoretical predictions, its successful demonstration by Maiman in 1960 [9], and the development of Ti:Sapphire ultrashort pulse lasers by Moulton in 1986 [10]. The Ti:Sapphire femtosecond laser system used in this thesis actually consists of a number of lasers and amplification systems used to achieve the intense, ultrashort pulses we desire. The first part of the laser system is the Spectra Physics *Millenia Vs*TM, which employs the output from a diode laser to pump (excite) Nd³⁺ ions doped in a yttrium vanadate crystalline matrix (Nd:YVO₄). The Nd³⁺ ion has principal absorption bands in the red and near infrared. Once the electrons are pumped to the initial excited state they quickly decay to a metastable state, E_2 , the upper level of the lasing transition, where they remain for a relatively long time ($\sim 60 \mu\text{s}$). The electron then drops to a lower excited level, E_1 , which quickly decays to the ground state. The ability of the excited electrons to remain in the higher state, E_2 , for a time much longer than the electrons in E_1 , provides the population inversion necessary for lasing. To sustain lasing action, the gain medium (Nd:YVO₄) must be placed in a resonant cavity where the light can be repeatedly transmitted through the crystal. This is done by placing the Nd:YVO₄ crystal between two parallel mirrors, where only photons emitted parallel to the resonant cavity axis will remain in the cavity and be able to interact with the medium. One of the mirrors transmits a fraction of this radiation and this becomes the output beam of the laser. The resulting 1064 nm laser output is then converted into visible wavelengths (532 nm) via frequency doubling in a temperature-tuned, lithium triborate (LBO), nonlinear crystal.

The *Millenia Vs*TM is able to supply up to 5W of optical pumping power at 532 nm to the next stage of the laser system, the femtosecond oscillator, Spectra Physics *Tsunami*TM. Within the *Tsunami*TM is a Ti:sapphire crystalline material produced by substituting Ti³⁺ ions for a small percentage of the Al³⁺ ions within sapphire (Al₂O₃). These Ti³⁺ ions have a broad range of absorption wavelengths from 400 to 600 nm that can be pumped by the 532 nm output of the *Millenia Vs*TM. The usable fluorescence band for lasing extends from 670 to 1100 nm. Lasing is achieved by placing the Ti:sapphire rod in a resonant cavity, but because this is a mode-locked laser, as opposed to the continuous wave (cw) source of the *Millenia Vs*TM, some special equipment is necessary. In the laser cavity, the electric field of the oscillating optical frequencies must repeat itself after one round trip within the cavity to survive. This restriction dictates that the oscillating wavelengths must satisfy the condition of a standing wave, such that an integral number of half-wavelengths must exactly fit between the two end mirrors. The frequencies that satisfy this condition are known as the longitudinal modes of the laser. To create a single pulse, it is necessary to “lock” the longitudinal modes in phase such that the waves interfere constructively at one point and destructively elsewhere. In the *Tsunami* this is accomplished by the use of an acousto-optic modulator (AOM). The AOM consists of a high optical quality quartz crystal with two highly polished surfaces, parallel to the direction of light propagation, one of which is attached to a piezoelectric transducer driven at radio frequencies. A standing acoustic wave is established within the material inducing a time-dependent refractive index grating perpendicular to the axis of light propagation. As the light interacts with this grating, a portion of it is diffracted and shifted in frequency, keeping the different modes locked in phase. Since light is diffracted out of the cavity only when the acoustic grating is present, driving the

AOM at the laser repetition rate ($c/2L$), where L is the laser cavity length, results in output pulses with a repetition rate of 80-82 MHz.

These output pulses have a central wavelength of ~ 800 nm, and a pulse duration of ~ 35 fs. The ability to create pulses with such a short duration relies on the fact that the usable fluorescence band for lasing from Ti^{3+} in sapphire is very broad. According to the time-energy uncertainty relationship, decreasing the duration of the pulse results in a spreading of the energy spectrum. This is due to the principle that the Fourier-transform-limited pulse duration is inversely proportional to its spectral width. When pulse durations, τ_p , in the femtosecond regime are considered, this requires the photon frequency, ν , ($E = h\nu$) to have a large bandwidth, $\Delta\nu$, such that the product $\Delta\nu\tau_p$ is larger than some fundamental value. This value is dependent on the exact shape of the pulse. In our case we use Gaussian shaped pulses, and a Fourier analysis determines that the product $\Delta\nu\tau_p$ must be larger than 0.441. For 35 fs pulses this results in a laser bandwidth requirement of ~ 28 nm measured at the full-width at half-maximum (FWHM) of the pulse. A pulse with $\tau_p \sim 1/\Delta\nu$ is said to be transform-limited. In our system, the bandwidth of the laser is ~ 40 nm, so the 35 fs pulse is only nearly transform-limited.

The femtosecond laser pulses at this point are of relatively low energy, on the order of a few nanojoules. The last stage of the laser system, Spectra Physics *Spitfire*TM, allows the production of pulses with much higher energy. The difficulty in amplifying these short pulses is that at even low energies they have relatively high intensities, capable of causing non-linear effects, which can destroy the beam quality as well as cause damage to the optical equipment. This problem was circumvented by the use of the chirped pulse amplification (CPA) technique, developed in 1960 for the amplification of radar signals [11], and then transformed for laser

technology by Strickland and Mourou in the 1980's [12]. The general idea of the CPA technique is to stretch the duration of the pulse, reducing its peak intensity, so that it can be amplified and then recompressed to near its original shape. In our system, the stretching of the pulse is accomplished by means of a diffraction grating configured so that the higher frequencies must travel a longer distance through the stretching component's optical path than the lower frequencies. This longer pulse, on the order of hundreds of picoseconds, is then amplified by a regenerative amplifier. The amplifier is able to pick out a single pulse through the use of a Pockel's cell, quarter-wave plate, and polarizer combination. The Pockel's cell is able to change the polarization state of the pulse due to Pockel's effect, which causes a birefringence change in an electro-optic crystal when a voltage is applied. In this configuration, the Pockel's cell acts as an optical shutter, which can be controlled to allow only one pulse into the amplifier cavity. This single pulse is directed through a Ti:sapphire rod, which has been optically excited by a Nd:YLF laser and allowed to pass through the gain medium many times, resulting in an amplification factor of $\sim 10^6$. The pulse is then recompressed by a second diffraction grating, performing the exact opposite function of the stretching grating, resulting in a pulse with a duration of ~ 55 fs, and an energy of over 1 mJ.

1.3 Single-Particle Interaction with Electromagnetic Waves

It is now imperative to discuss exactly how the laser light pulse will interact with the target. First, one must understand how the light will affect the motion of electrons, which move much more freely in the electromagnetic field than the heavier ions. Consider an electromagnetic wave with an amplitude of E_0 , traveling in the $+x$ -direction, with an angular frequency ω_0 and wave vector k . According to the wave equation, the electric field, E , of this wave follows the simple equation $E = E_0 \cos(kx - \omega_0 t)$. The intensity of this field is given by

the relation $I_o = \frac{c\varepsilon_0}{2} |E|^2$, where, ε_0 , is the vacuum permittivity, and c is the speed of light. The magnetic field produced by this wave follows the same relation, replacing E_0 with B_0 , where $\frac{E_0}{B_0} = c$, and following the condition that the electric and magnetic fields lie in planes perpendicular to each other. The motion of a charged particle in an electromagnetic field is governed by the Lorentz force

$$\vec{F} = q \left[\vec{E} + \frac{1}{c} (\vec{v} \times \vec{B}) \right], \quad (1.1)$$

where q is the charge of the particle and v is its velocity. Since the mass of an ion is so much larger than that of an electron, it is usually found that the motion of ions in an electromagnetic field is negligible. Therefore, we will concentrate on the motion of electrons.

At the intensities used in our experiments ($I_o = 10^{13}$ - 10^{16} W/cm²), the velocity of an electron is non-relativistic, and the $\vec{v} \times \vec{B}$ term can be neglected. This results in a simplified equation of motion for an electron

$$m_e \frac{\partial^2 \vec{r}_e(t)}{\partial t^2} = eE_o \cos(\omega t), \quad (1.2)$$

where m_e and e are the electron mass and charge, respectively, and $\vec{r}_e(t)$ is the time dependent position of the electron. It is clear that this motion represents an oscillation of the electron in the time domain. The maximum oscillation distance, known as the quiver amplitude, is given by

$$x_{\text{osc}} = \frac{eE_0}{m_e \omega_0^2}, \quad (1.3)$$

and the quiver velocity is given by

$$v_{\text{osc}} = \frac{eE_0}{m_e \omega_0}, \quad (1.4)$$

which are found by successive integration of Eq. 1.2 and finding the maximum value. For our laser operating at an intensity of 1×10^{16} W/cm² and a wavelength $\lambda_0 = \frac{2\pi c}{\omega_0}$, the quiver properties can be written as $x_{osc}[\text{nm}] = 13.7\sqrt{I_{16}}(\lambda_0)^2$ and $v_{osc}[\text{m/s}] = 0.086c\sqrt{I_{16}}(\lambda_0)$, where I_{16} is the laser intensity in units of 10^{16} W/cm² and λ_0 is in μm . The cycle-averaged kinetic energy gained by the quivering electron, known as the ponderomotive energy (U_p), is given by

$$U_p = \frac{1}{2}m_e v_{osc}^2 = \frac{e^2 E_0^2}{4m_e \omega_0^2}. \quad (1.5)$$

All of the previous equations were derived under the plane wave approximation, but for fs pulses, focused to small spot sizes on the order of a few micrometers, this description is inadequate. Due to the inhomogeneity in the electric field, the spatial distribution of the laser intensity is characterized by a strong gradient. In this type of field the electron is also subject to a nonlinear drift force known as the ponderomotive force, F_p . The magnitude of this force is given by

$$\vec{F}_p = -\frac{e^2}{4m_e \omega_0^2} \nabla \vec{E}^2, \quad (1.6)$$

which causes electrons to drift toward the weaker field area, resulting in electrons being pushed away from the laser axis.

1.4 Ionization of Matter Using Electromagnetic Radiation

To put the intensities used in this thesis in perspective, one can look at the electric field of the H nucleus on its electron. Assuming the distance between the proton and electron is the Bohr radius ($a_0 \approx 5.3 \times 10^{-11}$ m), the electric field, according to Coulomb's law, is

$E_a = \frac{e}{4\pi\epsilon_0 a_0^2} \approx 5.1 \times 10^9$ V/m. This corresponds to an intensity of $I_a \approx 3.51 \times 10^{16}$ W/cm² known as the atomic intensity. A laser with this intensity will overcome the Coulombic field of the atom, resulting in the electron being released into the continuum. While I_a represents the high-end limit of the intensities in this thesis, there are a number of ionization processes that occur at much lower intensities, circumventing the need to directly overcome the Coulomb barrier. These mechanisms depend strongly on the type of target material, as well as the parameters of the laser.

The first step in ionizing bulk matter is the production of free electrons. While metals usually have a sufficient number of free electrons in the conduction band at room temperature, semiconductors and dielectrics do not. Therefore, it is necessary to generate these electrons through optical field ionization (OFI). There are four main OFI processes relevant to our intensity range. The first is multi-photon ionization (MPI), which relies on the fact that the energy difference between the valence and conduction bands, known as the band gap, of most materials is larger than the energy of our laser photons. With a wavelength of 800 nm, corresponding to a photon energy of 1.54 eV, single photons from our Ti:sapphire laser are not typically capable of promoting an electron from the valence to the conduction band. Instead, it is possible for a material to absorb multiple photons simultaneously, resulting in a total energy high enough to promote a bound valence electron into the conduction band. The first experimental evidence for this process was found in the 1960's with gas phase atoms [13, 14]. Perturbation theory can adequately describe the rate of multi-photon absorption by,

$$\Gamma_{\text{MPI}} = \sigma I_0^n, \quad (1.7)$$

where σ is the cross-section for the process, and n is the number of photons required to overcome the band gap. The leftover energy of the process is converted into kinetic energy of

the free electron, such that $U_{e,\text{MPI}} = n\hbar\omega_0 - V_0$, where V_0 is the ionization potential. This process was found to become important at intensities greater than 10^{13} - 10^{14} W/cm².

The second OFI process is closely related to MPI. As the available intensity of lasers increased, researchers found electrons whose kinetic energy was greater than that of electrons created by MPI and were separated at intervals of $\hbar\omega_0$ [15, 16, 17]. Since, as required by the conservation of energy and momentum, it is not possible for a free electron to absorb a photon, the accepted explanation for this observation is that the electron's ion is acting as the necessary "momentum reservoir" for the absorption of photons by the electron. This process results in absorption of more photons than strictly necessary to free the electron, which is suggested by the name of this ionization process, "above-threshold ionization" (ATI). While it seems like ATI is merely a continuation of the MPI process, experiments suggest that this is a non-perturbative process and the ionization rates found for MPI no longer apply [18]. The intensity range where ATI becomes significant, though, is similar to that for MPI.

Perturbative analysis of ionization by an electromagnetic field begins to breakdown as the laser intensity approaches the atomic intensity, I_a . In this regime the electric field of the laser can sufficiently distort the atomic Coulomb potential such that the barrier between the continuum and bound state is significantly reduced, increasing the probability of the electron to tunnel through it. The electric field of the laser will cause the height and inclination of the barrier to oscillate at the frequency of the laser, therefore, the electron must tunnel through the barrier before the polarity of the field is reversed. Since the laser intensity essentially controls the change in the height and width of the barrier, and its frequency determines the available time for tunneling, they both become important factors controlling the ionization process known as tunnel ionization (TI). To define the boundary between the MPI and TI regimes, Keldysh [19]

developed a theory based on the characteristics of the laser electric field and ionization potential of the atom. This theory resulted in the introduction of the Keldysh parameter,

$$\gamma = \sqrt{\frac{V_0}{2U_p}} = \frac{\omega_0 \sqrt{2m_e V_0}}{eE_0}, \quad (1.8)$$

where V_0 is the ionization energy. MPI processes are favored for $\gamma > 1$, and TI for $\gamma < 1$. Essentially, TI prefers strong electromagnetic fields with lower frequencies. In terms of laser intensity and wavelength it is found that TI is more efficient than MPI for $I_0 [\text{W}/\text{cm}^2] \geq 5.36 \times 10^{12} \frac{V_0 [\text{eV}]}{(\lambda [\mu\text{m}])^2}$. For the intensity range and wavelength in this thesis (10^{13} - 10^{16} W/cm^2 and 800 nm), it is found that the TI regime is preferred at the peak intensity, but this does not rule out the MPI process occurring at the leading edge of the pulse.

The final OFI process is a natural extension of the tunneling process. If the intensity of the pulse is high enough, it can suppress the Coulomb barrier below the ionization energy so that the electron can escape spontaneously. This process is known as over-the-barrier ionization (OTBI) or barrier suppression ionization (BSI). Consider the potential experienced by an electron in this situation,

$$V(r, t) = -\frac{Ze^2}{r} - eE(t)r. \quad (1.9)$$

The first term represents the Coulomb field, and the second is due to the field imparted by the sinusoidally oscillating electric field of the laser. To determine the required intensity of the electromagnetic wave, we find the maximum of $V(r, t)$ and set it equal to V_0 . This results in a threshold intensity for OTBI for ions created with a charge Z of,

$$I_{th,OTBI} = \frac{cI_p^4}{128\pi Z^2 e^6}. \quad (1.10)$$

For the hydrogen atom ($V_0=13.6$ eV), this corresponds to a minimum intensity of $\sim 10^{14}$ W/cm². Experimental evidence supporting this explanation was found using 1 ps pulses with intensities up to 10^{16} W/cm² [20, 21].

OFI only constitutes the beginning of the ionization processes that occur when intense electromagnetic radiation interacts with bulk matter. At moderate intensities and pulse widths ($I_0 < 10^{15}$ W/cm² and $\tau_p > 50$ fs) the OFI processes only provide seed electrons which can directly interact with the laser field. These electrons will then follow the equations of motion described in section (1.3). Specifically, the electromagnetic wave will cause the electrons to oscillate in a sinusoidal motion. The energy gained by the electromagnetic wave is only transient, and will be lost by the electrons unless they find a way to convert this energy into some other form. The mechanism for this conversion is collisional absorption, in which an energetic electron collides with and imparts enough energy to another atom to ionize it, a process known as electron impact ionization, resulting in two free electrons. These electrons can then be heated by the laser photons, via a free-free absorption process known as “inverse bremsstrahlung”, and go on to free more electrons. This process occurs at a geometric rate during the laser pulse, resulting in an “avalanche” of electron production [22].

1.5 Plasma Generation

Through a combination of the initial ionization processes, a dense cloud of electrons is formed at the target surface during the leading edge of the pulse. This dense cloud of electrons and the resulting background of positive ions constitute a plasma. A necessary condition for a

collection of electrons and ions to constitute a plasma is that its dynamics are predominantly characterized by collective processes. Two important parameters are necessary to describe plasma behavior. The first parameter is the Debye length, λ_{De} , which defines the radius of a “sphere of influence”, known as the Debye sphere. A charged particle within the Debye sphere is shielded by electric fields originating outside of this sphere. To understand this concept, first consider a particle with charge q , placed at rest within a uniform electron density, n_0 , and assume that the ions exist as a fixed, neutralizing background. The highly mobile electrons will then redistribute to reach a thermally equilibrated electron density n_e described by the Boltzmann distribution,

$$n_e = n_0 e^{e\phi/k_B T_e}, \quad (1.11)$$

where e is the electron charge, k_B is the Boltzmann constant, T_e is the electron temperature, and ϕ is the electric potential determined by solving Poisson’s equation, giving

$$\phi = \frac{q}{r} e^{-r/\lambda_{De}}, \quad (1.12)$$

where the Debye length is given by

$$\lambda_{De} = (k_B T_e / 4\pi n_0 e^2). \quad (1.13)$$

This is the distance over which the redistribution of electrons occurs.

The second fundamental parameter governing plasma behavior is the plasma frequency, ω_p . An exact formula for this behavior is obtained by analyzing the motion of the electrons when they have been moved from their original equilibrium position. The Coulomb force acts as a restoring force, pulling the electrons back. The inertia of the electrons will cause them to

overshoot their equilibrium position, causing them to oscillate around their equilibrium position. In the approximation of a cold plasma, in which thermal motions of the electrons can be ignored and ions exist as a stationary positive background, we can consider the plasma frequency as being the frequency at which the electrons oscillate when they are disturbed from their equilibrium positions. It can be shown from the equation of motion of the electrons that this fluctuation in charge distribution will oscillate at the frequency,

$$\omega_p = \sqrt{\frac{4\pi n_e e^2}{m_e}}. \quad (1.14)$$

To be considered a plasma the collection of charged particles must meet several criteria. Firstly, the size of the plasma must exceed its characteristic Debye length. Since it is only within the Debye sphere that significant charge separation can occur, it is necessary that the plasma be large enough that these small changes in charge distribution do not affect the overall assumption of quasi-neutrality within the plasma. Secondly, the plasma should have a lifetime greater than the characteristic plasma time scale ($1/\omega_p$). This is the time scale governing the response time of the plasma in which any relevant plasma dynamics occur. Since the Debye shielding effect assumes a Boltzmann distribution of charged particles, it is also necessary that the Debye sphere has enough particles within it for the distribution function to be statistically valid [23, 24]. The number of particles can be approximated by estimating the parameters in the laser-created plasma. For a laser with an intensity of 10^{16} W/cm², typical values for the plasma are $n_e=10^{22}$ cm⁻³ and $T_e=500$ eV [22]. Using Eq. 1.13, this gives a Debye length of 1.7 nm. The number of particles within a Debye sphere is

$$N_D = \frac{4}{3}\pi n_e \lambda_{De}^3, \quad (1.15)$$

which for our parameters yield $N_D = 190$, easily satisfies the requirement that $N_D \gg 1$. The final condition is that the plasma is not overly dominated by collisions between oppositely charged species. The collision frequency, ν_{ei} , is classically calculated using the Spitzer formula [23, 25]

$$\nu_{ei} = \frac{e^4 Z n_e \ln \Lambda}{3(2\pi)^{3/2} \epsilon_0^2 m_e^{1/2} (k_B T_e)^{3/2}} = 2.9 \times 10^{-6} n_e Z T_e^{-3/2} \ln(\Lambda) \quad (1.16)$$

where $\ln(\Lambda)$ is the Coulomb logarithm with $\Lambda = \frac{b_{max}}{b_{min}}$, where b_{max} and b_{min} are the maximum and minimum impact parameters normally defined as the Debye length and the classical point of closest approach, respectively. This gives a value of

$$\Lambda = \frac{3(k_B T_e)^{3/2}}{Z(4\pi n_e)^{1/2} e^3} = \frac{9N_D}{Z}. \quad (1.17)$$

For the previous plasma parameters the collision frequency is $1.2 \times 10^{14} \text{ s}^{-1}$. Eq. 1.16 shows that the collision frequency is actually a *decreasing* function of temperature, due to the fact that the collisions between electrons and ions are facilitated by their mutual Coulombic attraction, which can be mitigated when the particles have high thermal velocities. It also shows the more obvious result that collisions increase with higher electron densities.

1.6 Plasma Hydrodynamics

The physical parameters describing the plasma are the electron density, temperature, and pressure, which are related by an equation of state. The hydrodynamic evolution of the plasma is typically described by the Vlasov equation, which is a phase space distribution function. Vlasov introduced this equation to deal with the difficulties faced in using the standard kinetic approach, based on the Boltzmann equations, when applied to systems with long range Coulombic

interactions [26]. Vlasov started with the continuity equation, neglecting collisional processes, given by,

$$\frac{\partial f_j}{\partial t} + \frac{\partial}{\partial x} \cdot \left(\frac{\partial x}{\partial t} f_j \right) + \frac{\partial}{\partial v} \cdot \left(\frac{\partial v}{\partial t} f_j \right) = 0, \quad (1.18)$$

where $f_j(x, v, t)$ is the spatial distribution function of the plasma characterizing the location of species j in phase space (x, v) . From the laws of motion, we have $\frac{\partial x}{\partial t} = v$ and

$\frac{\partial v}{\partial t} = \frac{q_j}{m_j} (E + v \times B)$. Substituting $\frac{\partial x}{\partial t}$ and $\frac{\partial v}{\partial t}$ into Eq. 1.18 we arrive at the Vlasov equation:

$$\frac{\partial f_j}{\partial t} + v \cdot \frac{\partial f_j}{\partial x} + \frac{q_j}{m_j} (E + v \times B) \cdot \frac{\partial f_j}{\partial v} = 0. \quad (1.19)$$

Instead of using the collision-based kinetic description of a plasma, Vlasov used a collective field created by the charged particles. By taking successive velocity moments of the Vlasov equation, where the n^{th} moment of f_j is found by integrating $v^n f_j$ over velocity, one may obtain the equations of motion for the plasma [23]. By taking the first moment, the continuity equation for the number density of species j is derived,

$$\frac{\partial n_j}{\partial t} + \frac{\partial}{\partial x} \cdot (n_j u_j) = 0, \quad (1.20)$$

which describes the time evolution of the density, n_j , where u_j is the mean velocity. The second moment of the Vlasov equation, known as the force equation, describes the time-dependence of the velocity,

$$n_j \left(\frac{\partial u_j}{\partial t} + u_j \cdot \frac{\partial u_j}{\partial x} \right) = \frac{n_j q_j}{m_j} (E + u_j \times B) - \frac{1}{m_j} \frac{\partial p_j}{\partial x}, \quad (1.21)$$

where m_j and q_j are the mass and charge of the particle j , and p_j is the pressure. The pressure can be determined from an isothermal equation of state for processes with the characteristic frequency (ω) and wave number (k) when $\omega/k \ll v_j$, which gives

$$p_j = n_j k_B T_j. \quad (1.22)$$

Instead, when $\omega/k \gg v_j$, we must use an adiabatic equation of state

$$\frac{p_j}{n_j^\gamma} = \text{constant} \quad (1.23)$$

where $\gamma = \frac{2+N}{N}$ and N is the number of degrees of freedom. It is common to use a two-fluid model which treats the ions and electrons separately in these equations. In order to account for inelastic events, we add a collision term to the right hand side of the Vlasov equation, resulting in

$$\frac{\partial f_j}{\partial t} + v \cdot \frac{\partial f_j}{\partial x} + \frac{F}{m} \frac{\partial f_j}{\partial v} = \sum_k \left(\frac{\partial f_{jk}}{\partial t} \right)_C, \quad (1.24)$$

where $\left(\frac{\partial f_{jk}}{\partial t} \right)_C$ represents the rate of change of f_j due to collisions with a charged species k .

Solving the fluid equations and assuming free, isothermal expansion results in an exponential density profile for the plasma, such that

$$n_e = n_{\text{sol}} \exp(-z/L), \quad (1.25)$$

where n_{sol} is solid electron density (10^{23} cm^{-3}), and L is the scale length, given by $L = c_s t$,

where t is time, and $c_s = (Z k_B T_e / M)^{1/2}$, is the ion acoustic speed of an ion with mass M and

charge Z , and T_e is the electron temperature. The spatial coordinate, z , is zero at the target surface and increases in the normal direction.

1.7 Plasma Absorption Mechanisms

Since the leading edge of the pulse is sufficiently intense to create a dense plasma at the target surface, it is important to explore how the rest of the pulse interacts with this plasma. To understand how light interacts with the plasma, it is necessary that we determine the plasma dielectric function. To do this we must first determine the motion of the electron within the plasma, which can be described under the same formulation as the Drude model for an electron gas in a metal. For a metal, the Drude model assumes that electrons in the conduction band behave like a gas carrying heat and current, and that the movement of electrons is slowed by stochastic collisions with the ions. In the presence of an electromagnetic field, the electron motion can be treated as a damped one-dimensional harmonic oscillator,

$$m \frac{d^2x}{dt^2} + \gamma \frac{dx}{dt} = -eE. \quad (1.26)$$

The damping constant can be evaluated in the limit of zero acceleration and is defined as $\gamma = \frac{m_e}{\tau_{ei}}$, where $\tau_{ei} = \nu_{ei}^{-1}$, is the collisional relaxation time constant. The conductivity of the material, σ , is related to τ_{ei} , by $\sigma = \frac{n_e e^2 \tau_{ei}}{m_e}$ [22]. For a sinusoidally varying electromagnetic field with a frequency ω_0 , a trial solution for Eq. 1.26 is $x = x_0 e^{i\omega_0 t}$, which yields

$$x = \frac{E}{\frac{m\omega_0^2}{e} + i\frac{m\omega_0}{\tau_{ei}}}. \quad (1.27)$$

The dielectric constant is defined as,

$$\epsilon = 1 + \chi_e = 1 + \frac{P}{\epsilon_0 E}, \quad (1.28)$$

where χ_e is the electric susceptibility, ϵ_0 is the permittivity, and P is the polarization, given by $P = -n_e e x$. Substituting Eq. 1.27 into the value for P in Eq. 1.28, and using Eq. 1.14, gives an expression for the dielectric constant,

$$\epsilon = 1 - \frac{\omega_p^2}{\omega_0^2 + i \frac{\omega_0}{\tau_{ei}}} = 1 - \frac{\omega_p^2 \left(\omega_0^2 - i \frac{\omega_0}{\tau_{ei}} \right)}{\omega_0^4 + \frac{\omega_0^2}{\tau_{ei}^2}}. \quad (1.29)$$

The complex index of refraction is given by $n = \eta_r + i\kappa = (\epsilon)^{1/2}$, where n_r is the real part of the refractive index and κ is the extinction coefficient, describing absorption by the material.

Assuming that the frequency of the light is much higher than the damping frequency ($\omega_0 \tau_{ei} \gg 1$), and decomposing this function into its real and imaginary components, we obtain an expression for the real part of the dielectric function

$$\epsilon_r \approx 1 - \frac{\omega_p^2}{\omega_0^2}, \quad (1.30)$$

resulting in the real part of the refractive index $\eta_r = \left(1 - \frac{\omega_p^2}{\omega_0^2} \right)^{1/2}$. Eq. 1.30 gives a dispersion relation for the light in the plasma,

$$k^2 c^2 = \omega_0^2 \epsilon = \omega_0^2 - \omega_p^2, \quad (1.31)$$

where k is the wave vector of the light in the plasma, whose magnitude is given by $|k| = \frac{2\pi}{\lambda}$.

From this expression we see that when the frequency of the light is larger than the plasma

frequency, k is real and the plasma is transparent. Instead, when $\omega_0 < \omega_p$, k is imaginary and the plasma is completely absorbing. At $\omega_0 = \omega_p$, $k = 0$, and the light wave is totally reflected.

Since the plasma frequency is solely dependent on n_e , we are able to determine the electron density at which $\omega_0 = \omega_p$. By rearranging Eq. 1.14, this density, known as the critical density, is given by

$$n_c = \frac{m_e \omega_0^2}{4\pi e^2}. \quad (1.32)$$

At densities greater than n_c the plasma is considered to be overdense, and it is underdense for densities less than the critical density. For our Ti:sapphire pulses, operating at a wavelength of 800 nm, the critical density is $1.7 \times 10^{21} \text{cm}^{-3}$, which is typically 1-2 orders of magnitude less than the solid electron density of the target material. Using the definition of n_c and ω_p it is possible to redefine the real part of the refractive index as $\eta_r = (1 - n_e/n_c)^{1/2}$.

The basis for collisional absorption in a plasma is outlined in sections 1.4 and 1.5. The Spitzer formula (Eq. 1.16) sufficiently describes the collision frequency within a plasma. Because the collision frequency is proportional to the electron density, and since light cannot penetrate past the critical density, the maximum of collisional absorption should occur at n_c [23]. Consider a plane wave propagating in the z -direction, into a plasma with an electron density that decreases linearly with $(n_e = n_c z/L)$. The wave equation for the electric field is

$$\frac{d^2 E}{dz^2} + \frac{\omega_0^2}{c^2} \epsilon(z) E = 0. \quad (1.33)$$

Neglecting the dependence of τ_{ei} on the electron density and approximating its value by its value at the critical density (τ_{ei}^*), the dielectric function from Eq. 1.29 follows as

$$\epsilon(z) = 1 - \frac{z}{L \left(1 + i \frac{1}{\tau_{ei}^* \omega_0} \right)}. \quad (1.34)$$

where the assumption that $\omega_p^2 = 4\pi n_c z e^2 / L m_e$ (found by substituting $n_e = n_c z / L$ into Eq. 1.14) and the definition of n_c from Eq. 1.32, are used to simplify the expression. Substituting this expression back into Eq. 1.33, and using an appropriate change of variables, the solution of the wave equation is an Airy function, which can be evaluated at the asymptotic limit to find the amplitude of the absorbed wave. This gives a fractional absorption for the collisional process of [23]

$$f_{A,coll.} = 1 - \exp\left(-\frac{8L}{3c\tau_{ei}^*}\right), \quad (1.35)$$

which can be modified for oblique incidence, at an angle θ , by multiplying the exponent by a factor of $\cos^3\theta$.

As mentioned previously, collisional absorption becomes less effective at higher temperatures. This is actually due to two factors. First is the reduction in the collision frequency, which scales as $T_e^{-3/2}$. Numerical simulation of the heat transport equation has shown that T_e scales roughly as $I_0^{4/9} \tau_p^{2/9}$, so that the collision frequency scales as $I_0^{-2/3} \tau_p^{-1/3}$ [22]. Also, as the electron quiver velocity, v_{osc} , becomes comparable to the electron thermal velocity, $v_{th} = (k_B T_e / m_e)^{1/2}$, the collision frequency is reduced, resulting in an effective collision frequency of [22]

$$v_{eff} = v_{ei} \frac{v_{te}^3}{(v_{th}^2 + v_{osc}^2)^{3/2}}. \quad (1.36)$$

The consequence of these effects is that collisional absorption becomes ineffective for intensities greater than $\sim 10^{15}$ W/cm².

Fortunately, absorption of light at higher intensities is facilitated by a number of other mechanisms. One of the most prevalent and widely established mechanisms is that of resonant absorption. For the case of an obliquely incident light wave, the electric field can be resolved into a superposition of two waves with a polarization vector that lies either parallel or perpendicular to the plane of incidence, known as p- or s-polarized components, respectively. For all waves that are not completely s-polarized, a portion of the electric field vector lies normal to the surface, in the direction of the plasma density gradient, and causes electrons to oscillate along this gradient. This oscillation results in fluctuations of the charge density, ultimately resulting in the generation of a longitudinal electrostatic wave (plasma wave) at the same frequency as the electromagnetic wave [23].

Consider a plasma with a density gradient varying only in the z -direction, with a light wave incident obliquely, lying in the y - z plane. The angle of incidence, θ , is defined as the angle between the propagation wave vector, k , and the z -axis. Since this wave now varies with both the y - and z -coordinates, the wave equation shown in Eq. 1.33 can then be adapted as

$$\frac{d^2 E}{dy^2} + \frac{d^2 E}{dz^2} + \frac{\omega_0^2}{c^2} \epsilon(z) E = 0. \quad (1.37)$$

Since the dielectric function is purely dependent on z , the wave vector, k_y , must be conserved.

For s-polarized light this gives the equation for the electromagnetic field

$$E_s = E(z) \exp\left(\frac{i\omega_0 y \sin\theta}{c}\right), \quad (1.38)$$

which, when substituted back into Eq. 1.37, yields

$$\frac{d^2 E(z)}{dz^2} + \frac{\omega^2}{c^2} (\epsilon(z) - \sin^2 \theta) E(z) = 0. \quad (1.39)$$

Neglecting collisions, the dielectric function can be approximated by Eq. 1.30 as $\epsilon(z) \approx 1 -$

$\frac{\omega_p^2(z)}{\omega_0^2}$. For a normally incident beam this predicts that the wave will be reflected at the critical

density, where $\omega_p = \omega_0$, but for obliquely incident light the reflection point is shifted to a lower

density, occurring when $\epsilon(z) = \sin^2 \theta$, or consequently when $\omega_p = \omega_0 \cos \theta$.

For p-polarized light it is simpler to first deal with the wave equation in terms of the magnetic field using Maxwell's equations. Here the magnetic field will be

$$B_s = B(z) \exp\left(\frac{i\omega_0 y \sin \theta}{c}\right), \quad (1.40)$$

From this representation we obtain

$$\frac{d^2 B(z)}{dz^2} + \frac{\omega^2}{c^2} (\epsilon(z) - \sin^2 \theta) B(z) - \frac{1}{\epsilon(z)} \frac{d\epsilon}{dz} \frac{dB(z)}{dz} = 0, \quad (1.41)$$

where the third term now contains a spatial derivative of the magnetic field as well as the dielectric function. Using Maxwell's equations again, this can be transformed into a wave equation for p-polarized light in the plasma,

$$\frac{d^2 E(z)}{dz^2} + \frac{\omega^2}{c^2} (\epsilon(z) - \sin^2 \theta) E(z) + \frac{\partial}{\partial z} \left(E_z \frac{d \ln(\epsilon(z))}{dz} \right) = 0. \quad (1.42).$$

The third term is the source for the charge separation, exclusive to p-polarized light, which is responsible for the generation of the electrostatic plasma wave. This term is negligible, except

near the critical density where the factor of $\frac{1}{\epsilon(z)}$ becomes infinite, due to the fact that the resonant

condition dictates $\omega_p = \omega_0$.

Technically, since the third term is negligible, the reflection point for p-polarized light is nearly the same as that for s-polarized light, but the electric field can penetrate past this point in the form of an exponentially decaying, evanescent wave. This wave tunnels up to the critical surface, generating charge density fluctuations at the same frequency at which the plasma resonantly responds, exciting a plasma wave [23]. To determine the amount of absorption this process is responsible for, it is necessary to calculate the magnitude of the electric field that reaches the critical density. To do this, we first assume a linearly varying plasma density gradient with a scale length much larger than the laser wavelength. Using the electric field at the turning point, estimated from an Airy function solution to Eq. 1.39 for s-polarized light, and using the fact that the wave will decay exponentially after the turning point, we can obtain an equation for the driving field of the resonance

$$E_d = \frac{E_{fs}}{\sqrt{2\pi\omega L/c}} \phi(\tau), \quad (1.43)$$

where E_{fs} is the electric field in free space, $\tau = (\omega L/c)^{1/3} \sin\theta$, and

$\phi(\tau) \cong 2.3\tau \exp(-2\tau^3/3)$. Here L is defined as the plasma density gradient scale length as

$L^{-1} = \frac{1}{n_e} \frac{\partial n_e}{\partial z}$. Eq. 1.43 establishes an optimum angle for resonant absorption, which is given as

$\theta_{\max} = \sin^{-1}[0.8(c/\omega L)^{1/3}]$. The physical origin of this dependence arises from two

competing factors. At small angles of incidence only a small component of the incident field lies in the direction of the density gradient, and hence does not have a significant ability to transfer energy to the plasma oscillations. For larger angles of incidence the distance between the reflection point and the critical density region is so large that the exponential decay of the wave results in a significantly reduced electric field at the critical density. The fractional absorption,

defined as the ratio of the absorbed energy to the total energy of the light, of the incident electromagnetic wave into the plasma electrostatic wave can be estimated by determining the absorbed energy flux due to the driving electric field, E_d , resulting in a fractional absorption,

$$f_{A,RA} \approx \phi^2(\tau)/2. \quad (1.44)$$

Numerical simulations, using a linear density profile, have shown that the maximum absorption for this mechanism can be as high as 50% [27, 28, 29].

While the resonant excitation of plasma waves results in a direct increase in the energy within the plasma, these waves are eventually damped by transferring their energy to the other plasma particles. The waves that are generated by resonant absorption are known as Langmuir waves, named after the discoverer [30]. The dispersion relation for waves in a plasma given in Eq. 1.31 is derived under the assumption of a “cold” plasma, in which electron thermal motions are ignored. In the laser-produced plasmas this condition is not satisfied, and to understand how plasma waves behave, a modified dispersion relation is necessary. By including the thermal velocity of the electrons, $v_{te} = \sqrt{\frac{k_B T_e}{m_e}}$, the dispersion relation for these waves can be described by [23]

$$\omega_0^2 = \omega_p^2 + 3k^2 v_{te}^2. \quad (1.45)$$

In the lower intensity regime ($I_0 < 10^{15} \text{ W/cm}^2$), the oscillating electrons in the wave can collide with ions translating the coherent motion of the wave into random thermal energy. A second, collisionless damping mechanism was first proposed by Landau [31] and is known as Landau damping. Landau damping occurs when electrons with velocities slightly less than the phase velocity of the wave, $v_p = \frac{\omega_0}{k}$, interact with the wave. The plasma wave accelerates these

particles, trying to match their velocity with its own phase velocity. A physical interpretation of this mechanism is similar to waves in water. If an object is moving slightly slower than a wave, the wave will push on the object and cause it to accelerate. If the velocity of the object is negligible compared to that of the wave, the object will simply bob up and down as the wave passes over, gaining little energy from the wave. A third mechanism for damping of plasma electrostatic waves is wave breaking, which only occurs at intensities greater than $\sim 10^{16} \text{ W/cm}^2$. If the amplitude of the plasma wave is large enough, it is possible to bring any particle into resonance with it, which results in a strong nonlinear damping. The amplitude of an electrostatic wave is known to be limited by wave breaking, which occurs when the electron quiver velocity exceeds the phase velocity, $v_\phi = \omega_p/k_p$. In the “cold” plasma approximation, this gives a limit for the amplitude of the electrostatic wave, $E_{\text{wb}} = \frac{m\omega_p v_p}{e}$ [32].

When the scale length of the plasma, L , is very small ($\sim 0.1\lambda_0$), resonance absorption is very inefficient, due to the fact that the electron quiver amplitude is larger than the spatial dimensions of the plasma, and plasma waves cannot be generated. Technically, Equations 1.43 and 1.44 are not even valid for $L/\lambda_0 < 0.08$, but the fractional absorption due to the resonance absorption mechanism has been shown to be significant even for plasmas with spatial dimensions on the order of $L/\lambda_0 = 0.1$ [29]. In the steeper regime of $L/\lambda_0 < 0.1$, a new mechanism for absorption begins to dominate. An electron near the plasma-vacuum boundary, interacting with the p-polarized component of the incident electromagnetic wave, can be pulled out of the plasma at a distance greater than the Debye length, and, during the next half cycle, accelerated back into the plasma. This mechanism was first proposed by Brunel in 1987 [33], and is known as either Brunel heating or vacuum heating. Although the laser is only able to penetrate up to the skin depth, $l_s \sim c/\omega_p$, of these overdense plasmas, the distance that electrons

are driven back into the plasma can far exceed this depth, so that they are able to interact collisionally with a much denser region of the plasma. This results in a direct heating of the plasma. The driving field of these electrons is

$$E_d = 2E_0 \sin\theta, \quad (1.46)$$

which results in an electron velocity of $2v_{osc} \sin\theta$. Brunel determined the fractional absorption of this mechanism to be [33]

$$f_{A,VH} = \left(\frac{\eta}{2\pi c}\right) \left(\frac{e}{m_e \omega_0 \cos\theta}\right) \frac{E_d^3}{E_0^2}, \quad (1.47)$$

where $\eta = 1.75(1 + 2v_{th}/v_{osc})$. Eq. 1.47 must be modified appropriately at higher intensities to account for relativistic velocities of the electrons and imperfect reflectivity, reducing the driving field [22]. For very steep density gradients ($L/\lambda_0 \sim 0.04$), vacuum heating is efficient at intensities as low as 10^{13} - 10^{14} W/cm² [34, 35, 36]. For the more modest density gradients, ($L/\lambda_0 \sim 0.1$), typically encountered under the conditions in this thesis, vacuum heating was found to be most efficient in the range of 10^{15} - 10^{16} W/cm², with a fractional absorption maximum of $\sim 60\%$ [34]. Interestingly, although Eq. 1.47 predicts that this mechanism should be maximized at grazing angles of incidence, numerical simulations show that an angle of incidence of 45° is preferred by this mechanism [34, 37]. The reason for this is that Brunel's model neglected the DC current set up along the surface of the target, which generates a magnetic field that would deflect returning electrons away from the plasma.

The final absorption mechanism relevant to our intensity regime is known as the anomalous skin effect (ASE). The normal skin effect is simply the process of collisional absorption which occurs within the skin depth, l_s . When the electron mean free path, $\lambda_{mfp} =$

v_{te}/v_{ei} , exceeds the skin depth, electrons heated by the laser can penetrate beyond l_s , effectively increasing the skin depth. To calculate the enhanced absorption due to this mechanism one must first determine the effective collision frequency, modified for this enlarged skin layer [22].

Using the formalism of Weibel [38], who first developed the theory of ASE in plasmas, the effective collision frequency is given by

$$v_{eff} = v_{te}/l_a, \quad (1.48)$$

where l_a is the modified skin layer approximated as

$$l_a \sim \left(\frac{c^2 v_{te}}{\omega_0 \omega_p^2} \right)^{1/3}. \quad (1.49)$$

This process dominates over the normal skin effect at intensities greater than 10^{17} W/cm², but it has been shown to account for ~10% absorption at intensities slightly less than this value [39].

Assuming a Maxwellian electron distribution and lower intensity regime ($v_{osc} \ll v_{th}$), the fractional absorption can be estimated as [40]

$$f_{A,ASE} \approx 0.6 \left(\frac{\omega_0}{\omega_p} \right)^{2/3} \left(\frac{v_{th}}{c} \right)^{1/3}. \quad (1.50)$$

This value is sensitive to the angle of incidence, laser polarization, and anisotropy of the electron velocity distribution, favoring grazing incidence, p-polarized light, and a highly anisotropic velocity distribution [39].

1.8 Thermal Processes

After the laser pulse has completed its interaction with the target, a hot, dense plasma is established, with a highly non-equilibrium temperature distribution. Femtosecond lasers make

creation of this state possible, without further interaction with the laser. The first process to occur in this state is thermalization of the electrons. This is accomplished by electron-electron scattering, until an equilibrium electron temperature is reached within the plasma. This equilibrium is reached fairly quickly, on the order of tens to a few hundreds of femtoseconds [41]. After the electrons have reached a common equilibrium temperature, energy transport is dominated by electron-ion relaxation via phonon generation. A phonon is simply a collective excitation of the lattice vibrational modes. Through the electron-phonon scattering process, the energy of the electrons is transferred to the lattice ions. This process is typically described by the “Two-Temperature Model”, in which the temperature of the electrons, T_e , and the lattice ions, T_i , are treated separately in a set of coupled differential equations, taking the form

$$C_e(T_e) \frac{\partial T_e}{\partial t} = \nabla(K_e \nabla T_e) - g_{e-ph}(T_e - T_i) + S, \quad (1.51)$$

$$C_i \frac{\partial T_i}{\partial t} = g_{e-ph}(T_e - T_i), \quad (1.52)$$

where $S = AI_0 \alpha \exp(\alpha z)$, is the laser heating term, with an absorption fraction A , the absorption coefficient is α , and z is in the direction of the target normal. C_e and C_i are volumetric heat capacities of the electrons and ions, K_e is the thermal conductivity of the electrons, and g_{e-ph} is the electron phonon coupling constant. Although electron-electron and electron-phonon scattering occur concurrently, the emitted phonons carry little energy, and therefore the electron-ion relaxation process requires many scattering processes, usually taking several picoseconds before the lattice and electrons reach equilibrium [41]. For example the relaxation time for the electrons in Al is, $\tau_e = C_e/g_{e-ph} \approx 100$ fs, and for the ions it is $\tau_l = C_l/g_{e-ph} \approx 6$ ps [42].

Although, at this point, the electrons and the lattice are in equilibrium, there are more free ions and electrons than allowed by the conditions of thermal equilibrium. These excess particles

are removed either by recombination of electrons and ions, or by diffusion into the rest of the material. When an electron and ion recombine, they can do so radiatively, in which the excess energy of the electron is given up to create a photon, or they can go through non-radiative processes such as Auger recombination, where the excess electron energy is used to promote a bound electron into a higher state. Contrastingly, diffusion of ions and electrons away from the excited region also occurs, but this does not actually reduce their number, and instead just redistributes them driven by the propensity to restore an equilibrium distribution.

The quick and extreme heating of the target causes rapid vaporization and expansion, resulting in ablation of the target, beginning on the order of tens of picoseconds and lasting for tens of nanoseconds [43, 44]. The temperature of the lattice ions, is estimated by [45]

$$T_i \approx \frac{F_a \alpha}{c_i} \exp(-\alpha z), \quad (1.53)$$

where $F_a = I_o \tau_p$, is the absorbed fluence. Significant evaporation of the target begins when $C_i T_i > \rho \Omega$, where ρ is the density and Ω is the specific heat of evaporation per unit mass. Using Eq. 1.53, the ablation depth per pulse follows a logarithmic dependence given by [45]

$$L_d \approx \alpha^{-1} \ln(F_a / F_{th}), \quad (1.54)$$

where $F_{th} \cong \rho \Omega / \alpha$. The material removed in this process constitutes the ablation plume, full of excited atoms that can decay radiatively, emitting light from electronic transitions characteristic of the atomic species. This light forms the basis for plasma spectroscopy.

2. Mechanism for Continuum Polarization in Laser-Induced Breakdown Spectroscopy of Si(111)

2.1 Introduction

Laser-induced breakdown spectroscopy (LIBS) is a powerful analytical technique that uses an intense laser pulse as a means of simultaneously ablating, atomizing, and exciting a sample material. Since only the small area that the focused laser ablates is affected, the technique is considered minimally destructive. Moreover, this ability permits the study of different regions of the same sample, enabling spatial resolution of chemical analysis. LIBS also requires very little to no sample preparation since it is a completely optical technique. The flexibility of LIBS makes it suitable for many applications such as hazardous material identification, biomedical, space exploration, and use in other environments where on-site human control may not be possible [46, 47, 48].

The LIBS technique begins with the ablation of the sample material. The ablation process results in a plasma plume emerging from the irradiated zone containing excited atomic and ionic species. At very early times the plasma emits a continuum of radiation that is usually attributed to two processes. The first is electron-ion recombination, in which free electrons are captured into a vacant orbital of an ion. A photon is then emitted having an energy that is the sum of the initial electronic kinetic energy and the binding energy of the bound state. The second process is known as bremsstrahlung and is due to the interaction of electrons and atomic nuclei causing a deceleration of the charged particle. The total energy of the system is conserved by emitting a photon of energy equal to the loss of kinetic energy of the decelerated charged particle. Also, electronically excited neutral and ionic species de-excite by emitting discrete radiation, characteristic of the material. These processes result in LIB spectra, which generally consist of sharp peaks riding on a continuous background [7, 49]. The continuum emission is

not spectroscopically useful for determining chemical composition and is usually suppressed by using a time-gated detector, effectively waiting for the short-lived continuum emission to diminish, allowing a larger signal/background ratio for detection of the discrete signal.

A novel technique for reducing the continuum background signal was introduced several years ago by Liu et al. [50] They found that ablation of Si(111) by 45 fs, 800 nm, pulses generated by a Ti:Sapphire laser system produced a plasma with a continuum background that was strongly polarized, while the discrete emission was at most weakly polarized. The polarization of the continuum emission was found to be strongest at their shortest detectable wavelengths, increasing to over 90% below 350 nm. They explained the polarization as a result of an anisotropic velocity distribution of the recombining electrons in the plasma. Their idea was to use a polarizer to block the polarized continuum emission, which would not affect the unpolarized discrete signal. Further studies generalized the phenomenon, indicating that polarized continuum emission occurred for metals [51, 52] and dielectrics [52]. Later, it was found that the polarized continuum could be generated by nanosecond (Nd:YAG laser, 532 nm) pulses as well [53, 54]. Asgill et al. [55] found contradicting results using 10 ns, 1.064 μm , pulses at a fluence of 1,020 J/cm^2 . In their studies they ablated a Cu sample and found only a small amount of polarization (<5%) of the plasma emission. Their explanation of the mechanism of the polarized emission was preferential reflection of s-polarized light in accordance with the Fresnel equations. Penczak et al. [56] attempted to reconcile the differences in the experiments by examining the fluence dependence of the polarization with an Al sample. They found in the fluence range of $\sim 5\text{-}500 \text{ J}/\text{cm}^2$ that the magnitude of the polarization decreased monotonically with fluence and claimed that the results from all the experiments could be correct because the phenomenon was dependent on the fluence used.

While the results seemed consistent, the explanation of the mechanism for continuum polarization was not. The experiments at lower fluences showed considerably larger polarizations that cannot be explained by the Fresnel reflection effect proposed by Asgill. Furthermore, experiments performed by the Gordon group [50, 51, 52, 53, 56] found that the polarization vector of the continuum emission followed that of a dipole emission in which p- or s-polarized incident light would result in p- or s-polarized continuum, respectively, while intermediate polarizations would follow a simple projection onto the observation plane. They also found that the light was confined to a cone around the direction of specular reflection (i.e. equal incidence and reflection angles), but their observation of increasing polarization at shorter wavelengths seemed to rule out a simple reflection or scattering mechanism. Instead they proposed multiple explanations involving either some sort of alignment within the plasma or a frequency up-conversion of the incident laser. Although Majd et al. [54] found similar polarization values, they asserted that the polarization was only s-polarized, irrespective of the incident laser polarization. They also proposed that this effect was caused by some kind of alignment occurring within the plasma.

The purpose of our latest study is to determine the mechanism for the polarization of the continuum light. We believe that if the plasma alignment or frequency up-conversion mechanisms are correct, then their effect must be very short-lived, presumably on a time scale comparable to the duration of the laser pulse. This hypothesis was tested using an ultrafast streak camera to quantify the time-dependence of the polarized emission. If the Fresnel mechanism is correct, we should see a polarized emission reflecting the predictions of the Fresnel equations.

2.2 Experimental Methods

Three sets of experiments were performed, each with its own apparatus. In all the experiments, Si(111) wafers were ablated in air with single laser shots, and the emitted light was collected and analyzed with a spectrograph. The first set of experiments was performed at the University of Illinois at Chicago (UIC), using the apparatus depicted in Figure 1. Laser pulses of ~65 fs duration were generated by a Ti:Sapphire laser (Spectra Physics Tsunami oscillator and Spitfire amplifier). The output of the regenerative amplifier had a peak intensity at 805 nm and a bandwidth of 24 nm (full width at half maximum), falling to 1% at 770 and 830 nm. A half-wave plate and polarizer were used to reduce the pulse energy, E , to within the range of 10 - 100 μJ , with a shot-to-shot variation of less than 3%. The polarization state of the laser was varied using a second half-wave plate. The laser beam was focused onto the sample with a microscope objective (10x, $NA=0.25$). The radius of the focused beam, ω_0 , was measured with a scanning knife edge and was found to have a value of $1.8 \pm 0.2 \mu\text{m}$. This quantity is the Gaussian radius of the electric field, corresponding to an irradiance of

$$I(r) = I_0 e^{-2r^2/\omega_0^2}, \quad (2.1)$$

and a peak fluence of

$$F = 2E \cos \theta_{in} / \pi \omega_0^2, \quad (2.2)$$

where θ_{in} is the angle of incidence. A polished Si(111) wafer was mounted on an automated sub- μm precision xyz translation stage. The stage advanced 100 μm between laser shots to expose a fresh surface for each pulse, with an average of 20 shots taken for each data point. The angles of incidence and detection (θ_{det}) were manually adjusted by moving the translation stage and laser beam optics. A notch filter (Chroma Technology, E690SPUV6) was used to block scattered

laser light. The filter transmitted $>85\%$ of the emitted light between 390 nm and 595 nm and rejected the laser light with transmittances of 1×10^{-6} , 2.3×10^{-6} , and 2.3×10^{-5} at 770, 800, and 830 nm, respectively.

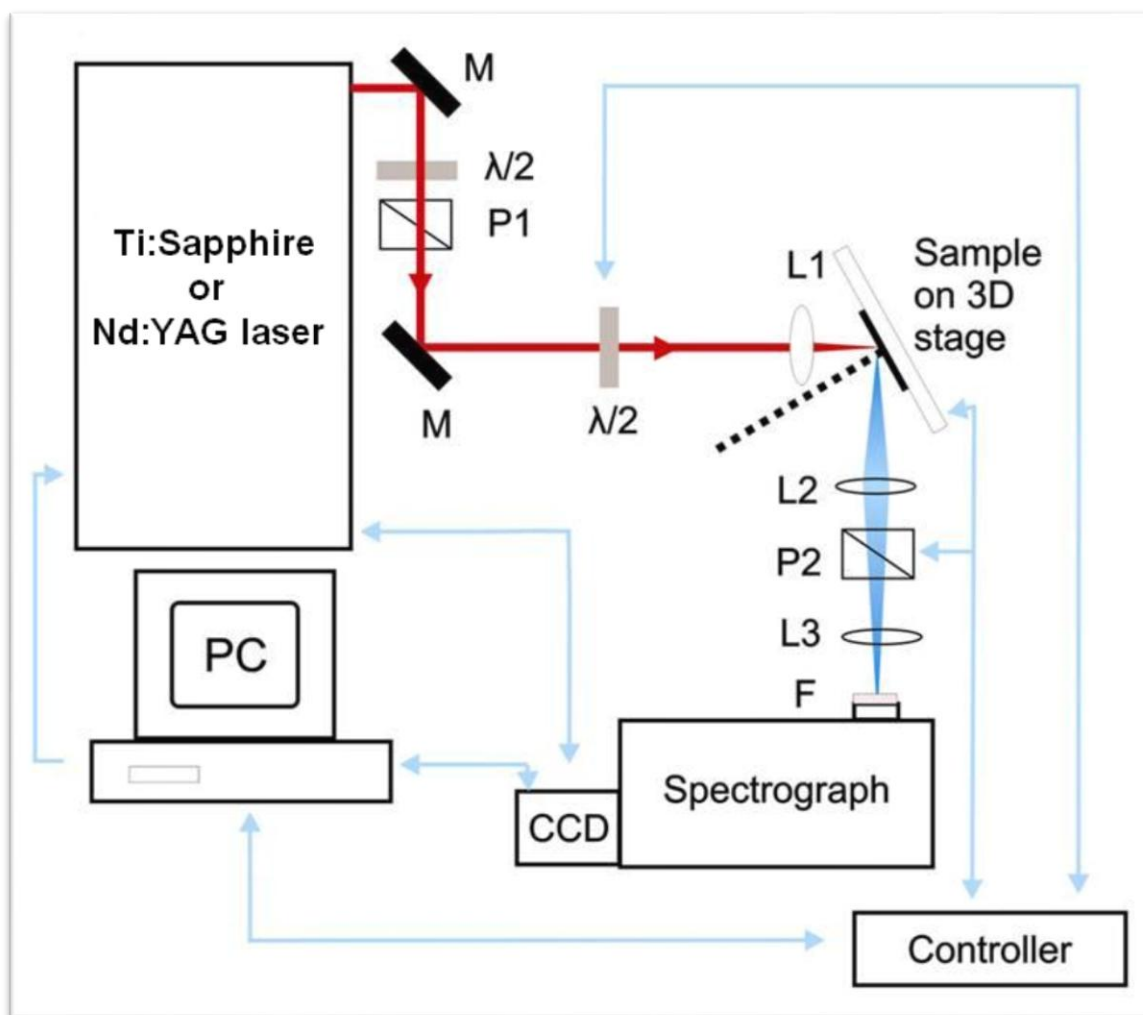


Figure 1 Schematic drawing of the apparatus used at UIC, including half wave plates ($\lambda/2$), polarizers (P1 and P2), lenses (L1, L2, and L3), and interference filter (F).

The ablating pulse generated a plume, consisting of electrons, ground state and electronically excited atoms and ions, molecules, and particulates. Light emission from this plume was focused onto the 600 μm entrance slit of a spectrograph (Spectrapro 2300i, Princeton Instruments), in which the spectrum was dispersed by a 300 lines/mm grating blazed at 500 nm, and was recorded with a non-gated, thermoelectrically cooled CCD (PIXIS 400, Princeton Instruments) camera. A Glan-Thompson polarizer (Red Optronics, GMP-6015), mounted on a motorized rotation stage, was inserted in front of the entrance slit of the spectrograph to measure the polarization of the plasma emission.

The second set of experiments was performed at the Center for Nanoscale Materials at Argonne National Laboratory (ANL). The primary difference between the apparatus at ANL and UIC is that the ANL setup used an ultrafast streak camera (Hamamatsu C5680) mounted on a spectrograph (Acton SP2150) to measure the emitted light as a function of time, with a resolution of 1.5% of the temporal gate (e.g. 750 ps for a time window of 50 ns, and a maximum resolution of 3 ps for a 140 ps window) and a slit width of 60 μm . As before, a Ti:Sapphire laser (Spectra-Physics MaiTai oscillator and Spitfire Pro amplifier, 35 fs pulse width) was used to ablate the sample. The laser was triggered at a rate of 18 Hz, while the sample was translated continuously at a speed great enough to ensure that the irradiated spots were separated by a minimum of 100 μm . The pulse energy was set between 50 and 100 μJ by means of a variable neutral density filter. The same notch filter and sample controller were used as in the UIC setup.

The third set of experiments, performed at UIC, used the second harmonic of a Nd:YAG laser (Continuum Surelite, 532 nm, 4 ns pulse width) to ablate the sample. A variable neutral density filter was placed before the focusing optics to set the pulse energy of the beam between 9 μJ and 4 mJ. The laser was focused onto the sample by a 100 mm focal length convex lens.

The focused laser beam had a radius of $\omega_0 = 22.6 \pm 1.4 \mu\text{m}$, which was measured with a scanning knife edge. An interference filter (Thorlabs, FES0500) was mounted directly in front of the entrance slit to block scattered laser light. This filter has a transmission range of 380 to 500 nm and a transmittance of 1.3×10^{-5} at 532 nm. The sample controller and spectrograph were the same as in the first apparatus, except that the slit width of the spectrograph was decreased to 200 μm .

Special precautions were taken to ensure that the signal was not contaminated by artifacts such as scattered laser light or polarization contributed by the detection optics. The polarization preference of the spectrometer grating was calibrated using an unpolarized white light source, such that we could account for any effects caused by differences in diffraction efficiencies of s- and p-polarization. As an additional precaution, an experiment was performed using a 2 m long, single-mode fiber (Ocean Optics, QP600-2-UV-VIS) placed in the optical path between the polarizer and spectrometer to act as a depolarizer. The degree of linear polarization of the laser source was 99.8%. We found that our particular fiber optics geometry resulted in the depolarization of the laser source by ~93%. The polarization of the emitted light was then measured with the fiber placed between the polarizer and spectrograph. We obtained nearly identical results as those using the grating calibration without the fiber, thereby ruling out the possibility that the monochromator/detector affected the polarization measurements. We also carefully checked the polarization properties of the optics (lenses and filter) in the detection path to confirm that they did not have any polarization preference. The entrance slit of the spectrometer was widened to 600 μm so that any misalignment of the polarizer would not result in part of the signal being lost on the edge of the slit. We also verified the results using a

photomultiplier tube (Hamamatsu R212), utilizing interference filters for different wavelength selections in the same range as the CCD measurements.

2.3 Results

Figures 2 and 3 show typical LIB spectra of Si recorded at UIC using a Ti:Sapphire or Nd:YAG laser, respectively. In both figures either an s-polarized (upper panel) or p-polarized (lower panel) incident laser was used. The two spectra in each panel represent the signal acquired with the use of a polarizer set to transmit only s-polarized light (upper trace) or p-polarized light (lower trace). It is evident from these spectra that s-polarized light is preferentially emitted from the plasma regardless of the 5 orders of magnitude difference in pulse duration. The identification of the most prominent peaks determined from the NIST atomic spectra database [57] is provided in Table I.

Features ‘a’, ‘b’, and ‘d’ are easily discernible in both spectra and are unequivocally assigned. Interestingly, the relative peak heights are very different for the two different laser systems. In the case of fs ablation, peak ‘b’ is nearly twice as intense as ‘a’, while in the ns spectra they are nearly equal. Also, peak ‘d’ is the dominant feature in the ns ablation spectra, while it is not nearly as prominent in the fs spectra. These differences can be qualitatively explained by the vast difference in pulse duration, which alters the energy absorption and excitation mechanisms within the ablation plume. Peaks ‘f’ and ‘g’ found only in the fs spectra are also known transitions that do not appear in the ns spectra simply because the filter used to block the fundamental light also blocks these wavelengths.

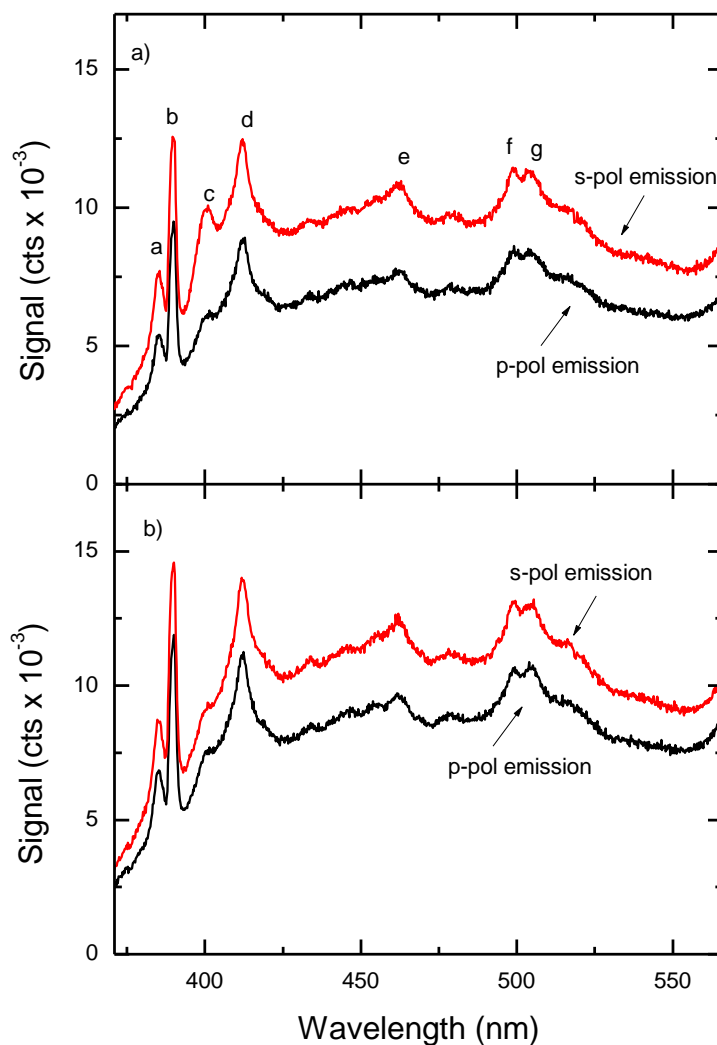


Figure 2 Laser-induced breakdown spectra obtained with an (a) s-polarized and (b) p-polarized fs laser at a fluence of 505.4 J/cm^2 and an angle of incidence of 30° . The upper (red) and lower (black) curves correspond to spectra taken with the polarizer set to admit s-polarized or p-polarized light, respectively. The peaks were assigned to neutral and ionic transitions (given in Table I), using the NIST atomic line database.

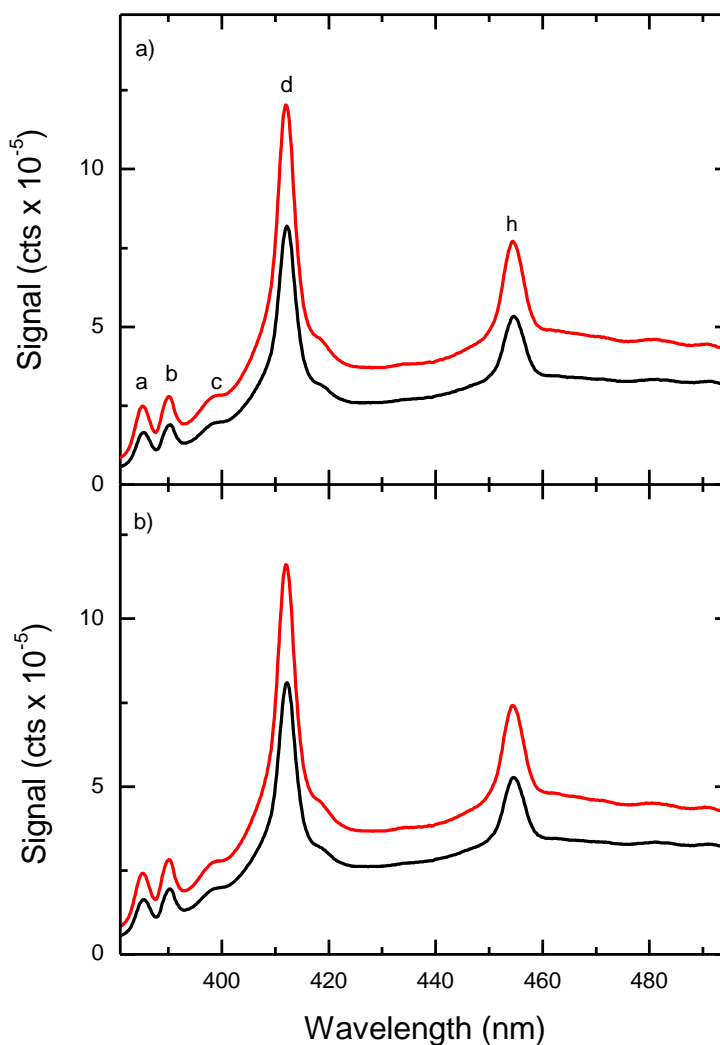


Figure 3 Laser-induced breakdown spectra obtained with an (a) s-polarized and (b) p-polarized ns laser at a fluence of 27.0 J/cm^2 and an angle of incidence of 30° . The upper (red) and lower (black) curves correspond to spectra taken with the polarizer set to admit s-polarized or p-polarized light, respectively. The peaks were assigned to neutral and ionic transitions (given in Table I), using the NIST atomic line database.

TABLE I ELECTRONIC TRANSITIONS OF SILICON

Label	$\lambda(\text{nm})$	Assignment	Label	$\lambda(\text{nm})$	Assignment
a	385.6	Si I $3s3p^2-3s4p$	e	462.1	Si II $3s^24d-3s^27f$
b	390.6	Si I $3s^23p^2-3s^23p4s$	f	500.6	Si I $3s^23p4s-3s^23p6p$
c	400	Second Harmonic of Ti:Sapphire laser	g	505.6	Si II $3s^24p-3s^24d$
d	413.1	Si II $3s^23d-3s^24f$	h	455	H'-X (5,0) band of the Si dimer (?)

Feature 'c', located near a wavelength of 400 nm, is not so easily assignable. More extensive studies designed to identify this peak revealed that for fs ablation it is the second harmonic of the fundamental laser frequency. The experimental findings will be discussed in Chapter 3. The ns spectra show a shoulder which we have also assigned as 'c' but cannot be explained by second harmonic generation. The most likely explanation is that it is due to the several weak Si^+ lines that coincidentally lie in this region.

Peaks 'e', seen only in the fs spectra, and 'h', seen only in the ns spectra, are also more difficult to identify. Although peak 'e' does have an assigned transition according to the NIST database, it is not immediately clear as to why it is absent in the ns spectrum. This emission is due to a transition of a highly excited Si^+ state, lying at $122,655 \text{ cm}^{-1}$. In order to populate this state, ten 800 nm photons or seven 532 nm photons are required. The fs laser has an irradiance 6 orders of magnitude higher than the ns laser, providing a much higher photon density and significantly increasing the probability of exciting this state. The assignment of peak 'h' is even more elusive. The NIST database does have a transition in that region with a large Einstein coefficient, but the energy of the upper level ($175,336 \text{ cm}^{-1}$) is even higher than the one responsible for the transition for peak 'e'. Using the previous argument, it is unlikely that this feature would be excited with the ns laser and not with the fs laser. A recent study performed by Ojha, Bajpai, and Gopal [58] found several new electronic states of the silicon dimer which were populated by 532 nm ablation of Si. In their findings, the most intense peak recorded matches our peak at 455 nm. Although we do not have a definite explanation as to why this occurs only with the ns excitation, it is known that the clustering process within the ablation plume are highly sensitive to the temporal properties of the pulse [59, 60].

The polarization of the plasma emission was carefully investigated by using a polarizer placed in front of the spectrometer. Spectra were recorded with the polarizer rotated in 20° intervals. The intensities at each wavelength were fitted to the Malus function,

$$A + B\cos^2(\alpha - \alpha_o) \quad (2.3)$$

where α is the polarizer angle, α_o is the angle of the polarization vector in the detection frame, and A and B are fitting parameters corresponding to the unpolarized and polarized signal, respectively. A typical result of this fitting is shown in Figure 4. It was found that a value of $\alpha_o = 44^\circ$ corresponds to s-polarization, using the laser to calibrate the polarizer. The polarization, P, is calculated as

$$P = (I_{max} - I_{min}) / (I_{max} + I_{min}) \quad (2.4)$$

where I_{max} and I_{min} are the maximum and minimum signal intensities. Using the fitted value of the Malus function, P is given by $B / (2A + B)$. With this analysis, the resulting values of P and α_o are plotted in Figures 5 and 6 for fs and ns excitation, respectively.

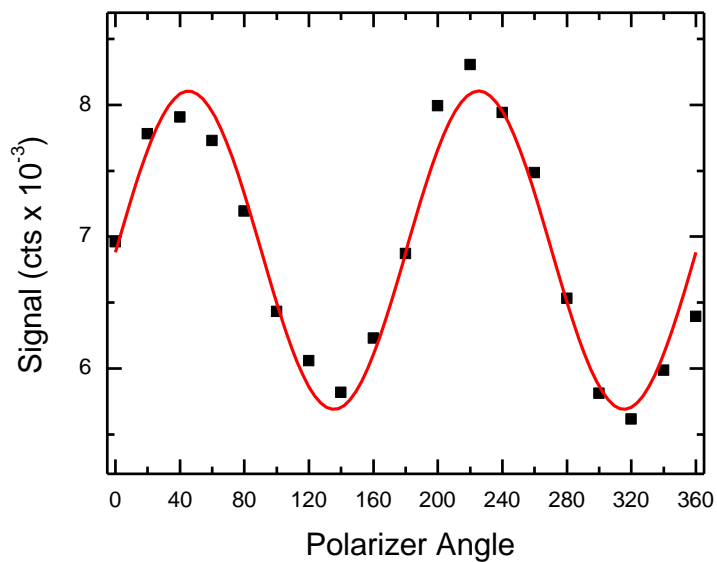


Figure 4 A typical plot of the emission intensity as a function of polarizer angle, using the UIC apparatus. The signal was recorded at 460 nm, using an s-polarized laser with a fluence of 503.6 J/cm^2 , an angle of incidence of 30° , and with the detector positioned perpendicular to the incident beam. The curve is a least squares fit of the Malus function.

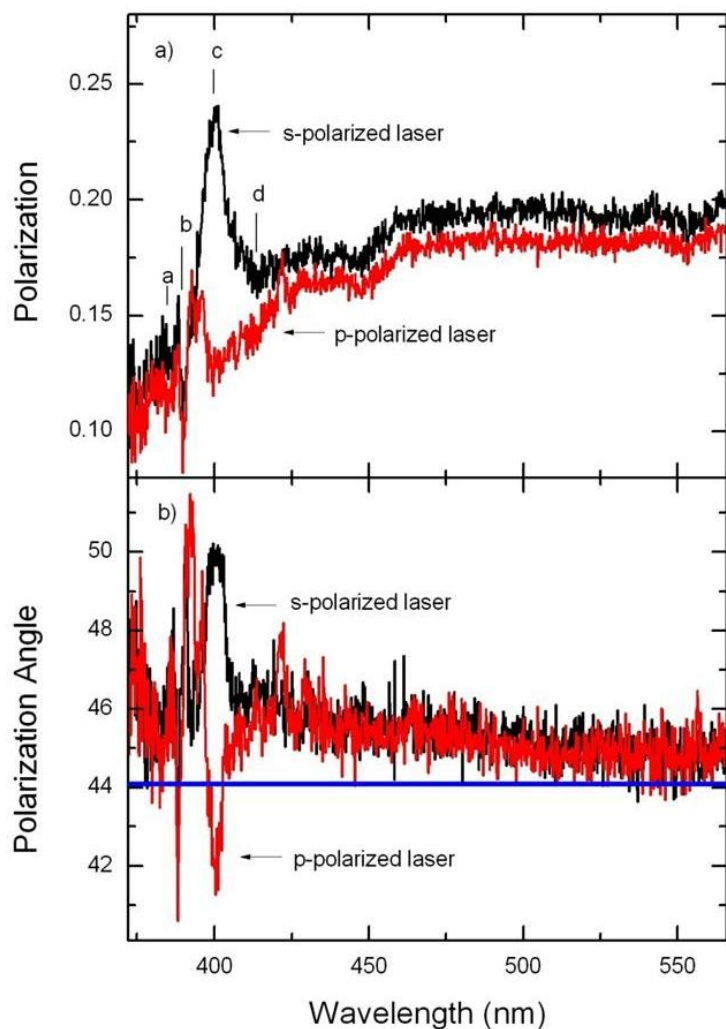


Figure 5 Polarization (panel (a)) and polarization angle (panel (b)) spectra showing the magnitude and angle of the polarization measured at each wavelength under the same conditions as in Figure 2 for fs excitation. The labels a-d in panel (a) mark the position of the peaks assigned in Figure 2. The horizontal line in panel (b) corresponds to s-polarized emission.

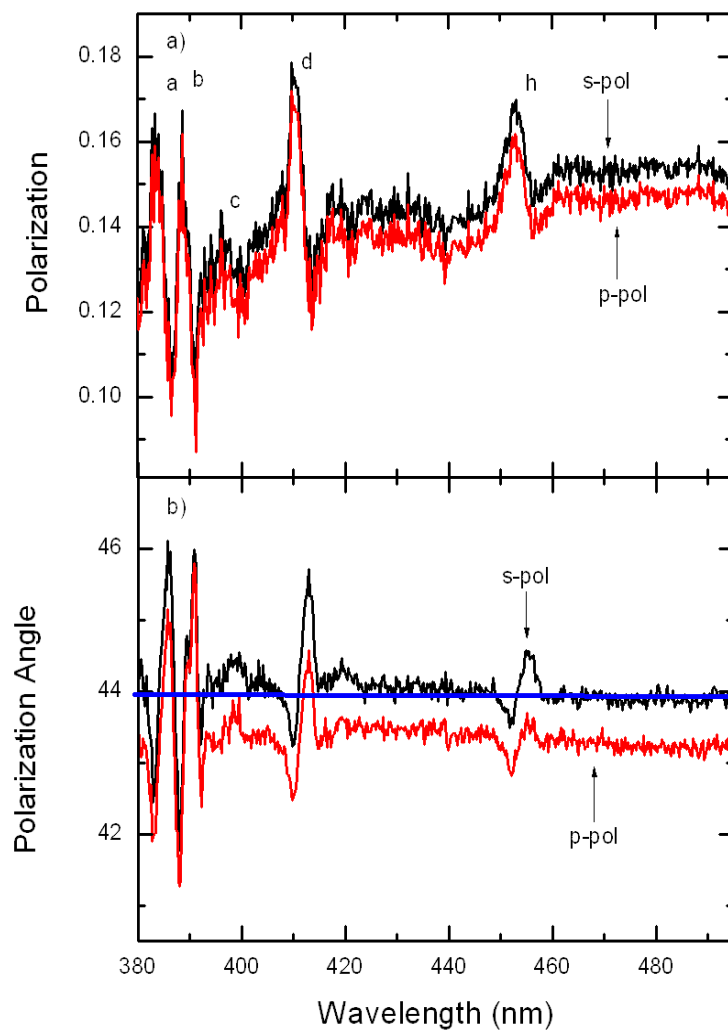


Figure 6 Polarization (panel (a)) and polarization angle (panel (b)) spectra recorded under the same conditions as Figure 3 for ns excitation. The labels a-d, h in panel (a) mark the positions of the peaks assigned in Figure 3. The horizontal line in panel (b) corresponds to s-polarized emission.

For fs excitation the spectra show that the continuum emission is polarized between 12 and 20%, increasing with wavelength. The small difference between s and p-polarized excitation is not statistically significant and varied in repeated experiments with an uncertainty of $\pm 1.5\%$. There are also structural features superposed on the background corresponding to the most intense transitions seen in the normal LIB spectra. The slight change in the polarization of these lines shows that some other mechanism is responsible for the discrete transitions. The strong feature at 'c' gives further evidence to our assignment of this peak as being due to the second harmonic. Second harmonic generation is found to be strongly polarized, and in our experiments this polarization preserves that of the incident laser. For s-polarized excitation the second harmonic adds to the s-polarized background while the opposite is true for the second harmonic generated by a p-polarized laser, resulting in the peak or dip features in the polarization spectra. Figure 5b shows the polarization angle spectrum calculated from the fitting to the Malus function. It is seen that α_0 lies within a few degrees of the s-plane, gradually decreasing with increasing wavelength. Some of the spectral structure is also evident, especially at the position of the second harmonic signal.

For ns excitation the same general trend in polarization is seen. The polarization of the continuum emission varies from 12 to 15%, slightly increasing with wavelength. The polarization angle is also found to lie within a few degrees of the s-plane. The labeled features within the spectra again correspond to the peaks in the LIB spectra. The larger variation in the polarization and polarization angle spectra at these features is attributed to the larger discrete signal compared to the background continuum emission. As opposed to fs excitation, peak 'c' is found to contribute very little to the polarization spectra, further confirming that in the case of ns excitation this peak is merely a weak discrete Si transition. Closer examination reveals

asymmetric profiles in both the P and α_0 spectra, with the inflection point centered at the maximum intensity of the transition. A hint of this asymmetry is also evident in the fs spectra, but the poorer signal-to-noise ratio makes it difficult to discern. The explanation for this asymmetry is still unclear.

Figure 7 displays time-resolved measurements of the emission intensity, polarization, and polarization angle obtained with a streak camera at ANL. These data are a representative portion of the continuum signal, centered at 480 nm. In Figure 7a the continuum emission intensity rises sharply to a maximum within 2.9 ns falling to $1/e$ of that value approximately 1.0 ns later. The middle panel shows the polarization remaining fairly constant (5-10%) for the first 8 ns and then slowly rising to a maximum value (15-25%) at 45 ns. The polarization angle, shown in Figure 7c, is shown to vary within $\pm 5^\circ$ of the s-plane throughout the entire range of the experiment. The variation in the polarization angle is only a measure of the noise in the measurement and does not represent any actual temporal trend.

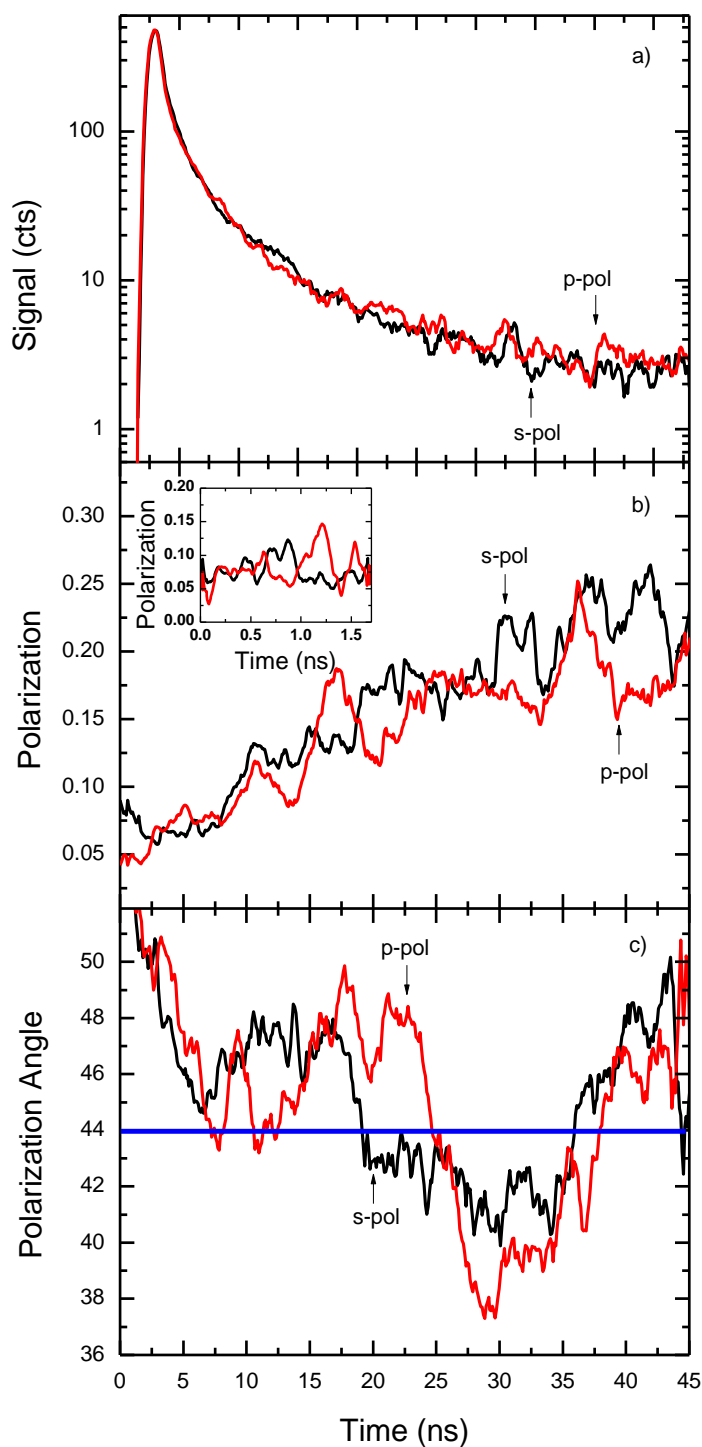


Figure 7

Time-resolved polarization data taken with the ANL fs laser at a fluence of 1700 J/cm^2 and an angle of incidence of 30° . The data are for a wavelength of 480 nm. The panels show (a) the signal intensity, (b) the magnitude of the polarization, and (c) the polarization angle. The inset in (b) is a higher resolution scan of the polarization for the first 2 ns of the emission. The horizontal line in panel (c) corresponds to s-polarized emission.

Using the ns laser at UIC, the dependence of the polarization on laser fluence was tested. It was found that at low fluences in the range of $\sim 1\text{-}30\text{ J/cm}^2$ the polarization remained fairly constant, but that at higher fluences the polarization dropped monotonically. Figure 8 shows a representative sample of the amount of polarization recorded at a wavelength of 460 nm. Here the polarization remains near 15% in the low fluence range and drops to $\sim 5\text{-}7\%$ at the highest fluence of 432 J/cm^2 . This result agrees well with the amount of polarization found in previous studies at similar fluence and wavelength ranges performed by Majd et al. and Asgill et al. [54, 55].

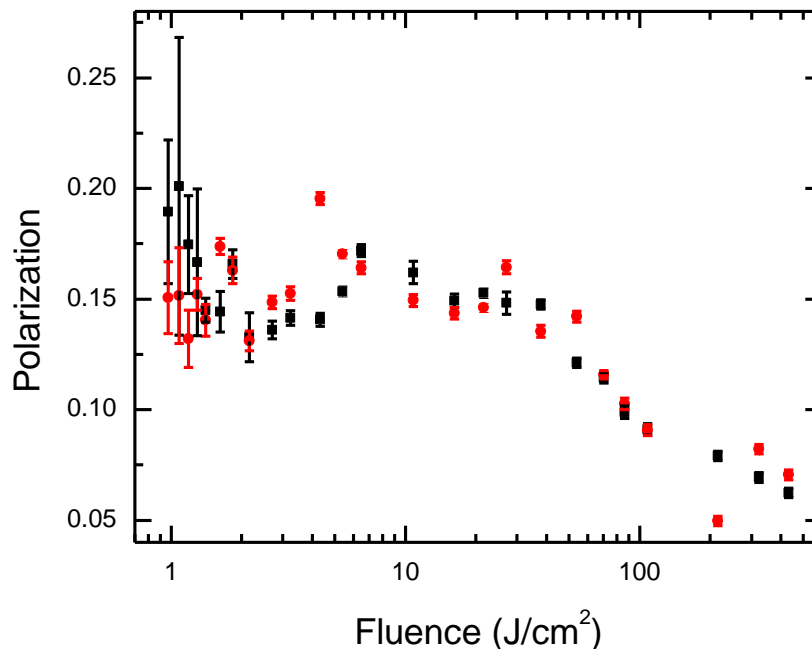


Figure 8 Fluence dependence of the polarization using either an s- (black squares) or p-polarized (red circles) ns laser. The data were recorded at an angle of incidence of 30° , with the detector positioned perpendicular to the incident laser beam. The error bars are a single standard deviation of the polarization measurement.

2.4 Discussion

There are a number of mechanisms that may lead to polarized emission from a plasma. One of the more likely, albeit trivial, mechanisms would be scattering of the fundamental beam. While the notch filter most likely is enough to block all scattered laser light, there are two additional reasons why this is unlikely to be the explanation. Polarized light due to laser scatter would only be evident on the timescale of the incident pulse, whereas the time-resolved measurements performed at ANL show that the polarization is long-lived (>45 ns), and actually increases with time. Also, the polarization state of the light would be expected to follow that of the laser, while instead it was found that the polarized component of the emission is always in the s-polarized direction. Another possibility is frequency up-conversion of the fundamental beam, conceivably due to self-phase modulation, but this mechanism can also be ruled out by the previous time dependence and polarization state arguments. The third mechanism is based on the anisotropic velocity distribution of electrons in the plasma. When these electrons recombine with ions, their directed motion can result in polarized emission [61]. Our finding that the polarization lasts for so long and, more importantly, increases with time makes it difficult to invoke this plasma alignment mechanism. It is unlikely that this alignment could be sustained for the observed duration without some external means.

This leaves the mechanism due to selective reflection of the plasma emission from the sample surface. Time-resolved microscopy experiments have revealed the formation of a highly reflective liquid phase that persists for nanoseconds [62]. Other experiments utilizing a pump-probe technique yielded time-resolved measurements of the reflectance of semiconductors in the melting and ablative regime [63, 64, 65, 66, 67]. The development of a highly reflective surface would result in the preferential reflection of s-polarized light in accordance with the Fresnel

formulae. In our model, we assume that the recorded signal is a combination of the light emitted directly from the plasma as well as the light that first strikes the sample surface and is reflected towards the detector. The geometrical considerations are displayed in Figure 9.

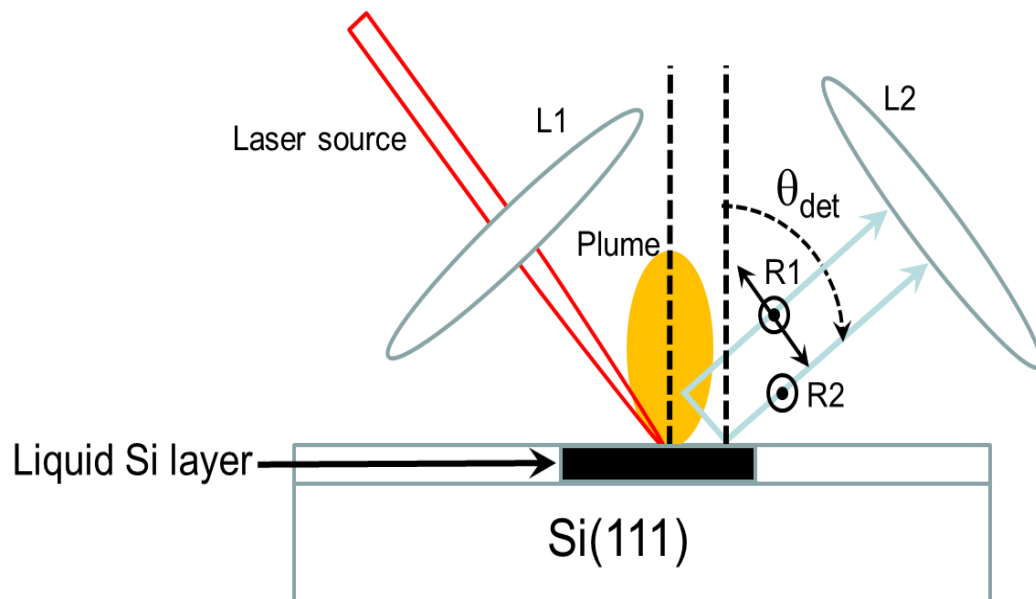


Figure 9 Schematic drawing of the light emitted from the plasma plume and detected at an angle θ_{det} . Rays R1 and R2 represent light emitted directly from the plasma without reflection and light emitted from the plasma and subsequently reflected by the liquid Si surface layer, respectively. Electric field orientation vectors are shown for rays R1 and R2 to illustrate either unpolarized (R1) or s-polarized (R2) character of the respective rays, the latter caused by the Fresnel effect upon reflection. The positions of lenses L1 and L2 correspond to the same optical setup illustrated in Figure. 1.

Using Maxwell's equations, one can determine the composition of a reflected and transmitted wave with respect to the incident wave. The boundary conditions derived from these equations dictate that the normal and parallel components of these waves must be continuous across the boundary. With these considerations and introducing the complex index of refraction, $n = \eta_r + i\kappa$, where η_r is the real refractive index and κ the extinction index, the Fresnel equations give the coefficients of reflection for s- and p-polarized light,

$$r_s = \frac{n_1 \cos \phi - n_2 \cos \theta}{n_1 \cos \phi + n_2 \cos \theta} \quad (2.5)$$

and

$$r_p = \frac{n_1 \cos \theta - n_2 \cos \phi}{n_1 \cos \theta + n_2 \cos \phi}, \quad (2.6)$$

where θ and ϕ are the angles of incidence and refraction, respectively, of the plasma emission [68]. The subscripts 1 and 2 apply to the medium of the incident wave and the absorbing/reflecting surface, respectively. The reflectance coefficients, R_s and R_p , are equal to the square of the magnitude of r_s or r_p .

As is well known, for a transparent material the Fresnel equations predict that the reflectance of p-polarized light actually reaches zero at a certain angle $\theta = \theta_B$, called the Brewster angle. By setting the numerator of Eq. 2.6 to zero and applying Snell's law it is possible to show that $\tan \theta_B = \frac{n_2}{n_1}$. For absorbing materials such as metals and semiconductors, the extinction index, κ , can no longer be assumed to be zero, and instead R_p reaches a minimum at this angle. Since the difference between R_s and R_p is not a constant, the amount of polarization of the reflected wave should change with the angle of incidence. Equations 2.5 and 2.6, along

with Snell's law, indicate that the reflected wave will always have a dominating s-polarized component.

Assuming the initial plasma emission is unpolarized, we can substitute the reflectance R_s and R_p into Eq. 2.4 as the maximum and minimum intensity signals, respectively, yielding a reflected wave with polarization

$$P = \frac{R_s - R_p}{R_s + R_p}. \quad (2.7)$$

As indicated in Figure 9, the signal measured by the detector is a combination of the light reflected from the sample surface as well as the light that reaches the detector directly from the plasma. Therefore, the total signal can be broken up into the two components f_r and f_d , arising from reflected and direct paths, respectively, where $f_r + f_d = 1$. If we assume that the fraction f_d is unpolarized and remains constant with incident angle, the maximum signal is just $f_d + f_r R_s$ and the minimum signal is $f_d + f_r R_p$. Plugging this into Eq. 2.4 yields the observed polarization

$$P' = \frac{f_r(R_s - R_p)}{2f_d + f_r(R_s + R_p)}. \quad (2.8)$$

Here we assume that the coherent interference of the direct and reflected rays averages to zero such that their intensities can be simply added together. This assumption is justified because of spatial averaging of the emission originating from adjacent regions of the plume.

Since we assume that the plasma plume always expands normal to the surface, it is not possible to control the angle of incidence directly. Instead, with the knowledge that the light is specularly reflected, we may choose to observe light at different incidence angles by changing

the angle of detection, θ_{det} . Using the ns apparatus, we measured the polarization while varying θ_{det} from 0 to 90° with respect to the sample normal. Figure 10 shows the results as well as the calculated values of R_s , R_p , P , and P' . Here we assumed that direct and reflected light reached the detector in equal proportions, (i.e. $f_r = f_d = 0.5$). The values of R_s and R_p were calculated using the complex index of refraction of liquid Si at 488 nm ($n = 2.89 + 4.98i$) [69]. While the quantitative agreement between the measured and calculated polarization values is most likely fortuitous, due to the arbitrary choice of f_d and f_r , and the assumption that n_2 does not vary with time, the agreement of the trend is nevertheless obvious. A minimum in the polarization is observed at $\theta_{det} = 0^\circ$, where R_s and R_p are equal, whereas a maximum is found near the Brewster angle of $\sim 80^\circ$, where the reflectance of p-polarized light drops to less than half of that of s-polarized light. The complex refractive index of liquid Si varies with the wavelength of the light. This dependence is shown in Figure 11 as well as the measured polarization spectrum recorded at the Brewster angle using the ns apparatus. The calculated and measured polarization both show a gradual increase as the wavelength of the light is increased.

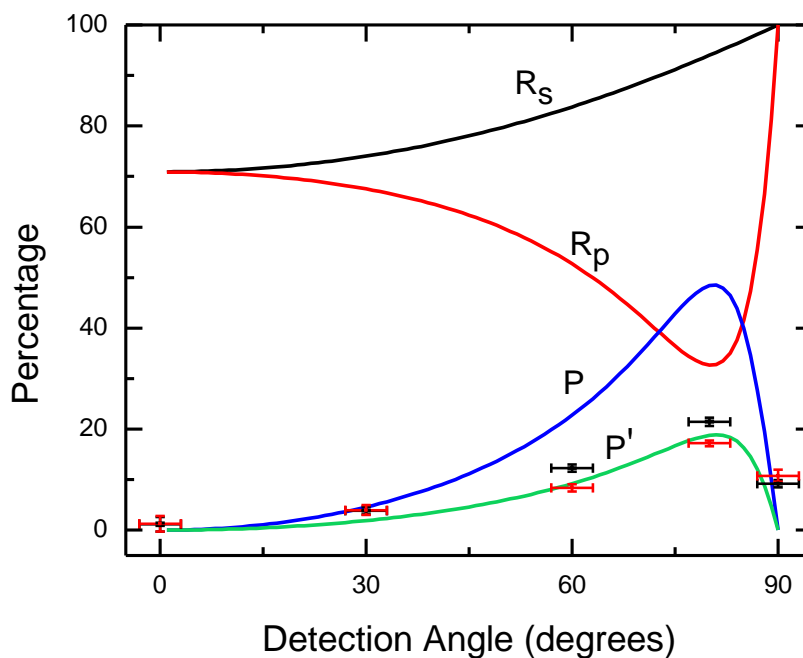


Figure 10 Polarization of the 488 nm emission as a function of detection angle measured with the ns apparatus, using either an s- (black symbols) or p-polarized (red symbols) laser. Data are recorded at a fluence of 21.6 J/cm^2 and an angle of incidence of 40° . The detection angle is measured with respect to the surface normal. Vertical error bars are a single standard deviation of the polarization measurement, and the horizontal error bars are an estimate of the experimental uncertainty in the measurement. The curves are calculated using the complex index of refraction from reference [69] and Equations 2.5-2.8.

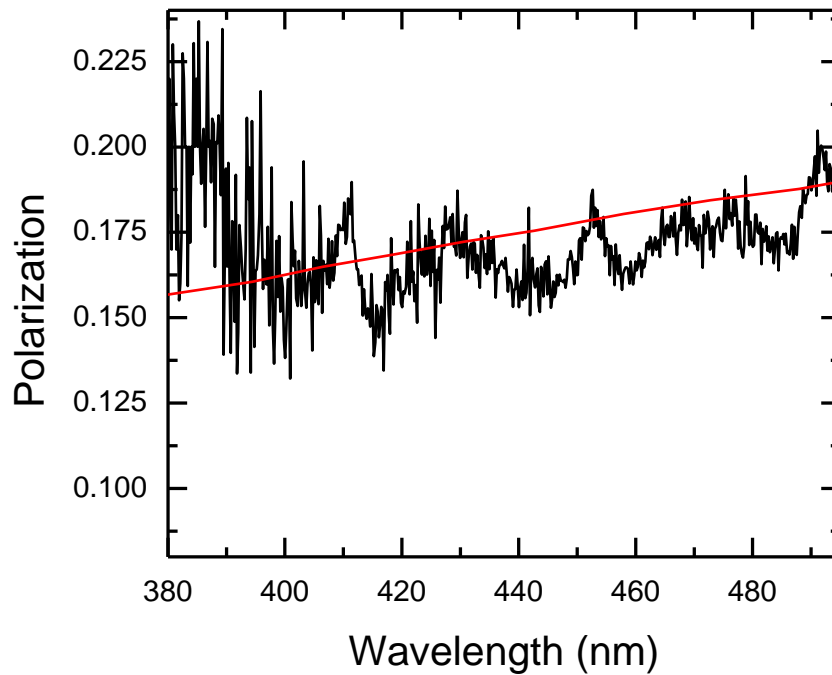


Figure 11 Polarization spectrum measured with ns apparatus with the same conditions as Figure 3 but with $\theta_{det} = 80^\circ$. The smooth curve is the calculated value of P' using an equal fraction of reflected and directly detected light.

The Fresnel formulae show how the angle of incidence and the complex index of refraction dictate the characteristics of the reflection of light at an interface. Specifically, the theory shows that s-polarized light has a higher reflectance than p-polarized light. Also, since the reflectance is dependent on the angle of incidence, the ratio between the reflected s- and p-polarized components will vary as the angle of incidence is changed. Furthermore, since the complex index of refraction is dependent on the wavelength of light, this ratio will vary also with wavelength. The strong agreement of the data and the Fresnel predictions for the polarization of

the continuum as well as its dependence on the angle of incidence and the index of refraction strongly support the Fresnel mechanism.

The results for ns and fs excitation are consistent as there is no explicit dependence on laser wavelength dictated by the Fresnel equations other than time dependent considerations of the complex refractive index of the liquid phase. While the exact mechanism for the drop in polarization with increasing fluence is uncertain, it is possible that the fraction of reflected light reaching the detector is decreased at higher fluence. This could be a result of the formation of a denser plasma which then blocks the surface-reflected light more efficiently. Another possibility could be that the more intense incident beam could disrupt the liquid layer, causing the light to be scattered non-specularly. This explanation resolves the discrepancies between the amount of polarization measured in the high fluence regime by Asgill et al. [55] and that measured in our lower fluence regime.

The structure in our polarization spectra at discrete transitions is very similar to that observed by Majd et al [54]. It is possible that the light from these electronic transitions is created at a different place in the plasma and that the ratio between the reflected and directly detected light is affected. It is also very likely that the evolution of the plasma and the liquid surface layer results in different conditions when each of these processes occurs. It is well known that the continuum emission is short-lived, on the order of tens of nanoseconds, whereas the discrete electronic emission lasts for a much longer time. On these timescales the reflectivity of the surface as well as the density of the plasma will change dramatically. While this explains a difference in the polarization compared to that of the continuum emission, it does not explain the asymmetry in the polarization and polarization angle profiles. This phenomenon and the evolution of the polarized emission in time are still ripe for experimental investigation. An

explanation of these processes may give a much better understanding of what is occurring in the plasma and in the target during laser-induced breakdown conditions.

3. Investigation of Second Harmonic Generation in Laser Produced Plasmas Using Dual Femtosecond Pulses

3.1 Introduction

Harmonic generation (HG) from laser-induced plasmas has been studied for over thirty years. Some of the first measurements were made by Burnett et al. [70] and Carman et al. [71, 72] with nanosecond CO₂ lasers. With the development of ultrashort lasers and the Chirped Pulse Amplification (CPA) technique, a new realm of plasma formation is available, in which lasers can interact with a plasma before it has time to expand. The ability to create extremely dense plasmas with electron densities approaching solid density ($\sim 10^{23} \text{ cm}^{-3}$) not only allows studies of HG in plasmas with steep electron density gradients but also provides the opportunity to probe the effects of different stages of hydrodynamic plasma expansion on HG. Early experiments with femtosecond lasers have shown that the interaction of ultrashort laser pulses with an expanding plasma involves an abundance of complex processes on a sub-picosecond timescale [73, 74]. Interest in HG in plasmas is driven by the desire to create ultrashort, high-order harmonics in the UV to X-ray regime [22, 75, 76], attosecond pulses [77, 78], and diagnostic tools for studying plasma properties [79, 80, 81, 82].

In the non-relativistic intensity regime ($I < 10^{18} \text{ W/cm}^2$) there are two potentially significant mechanisms for second harmonic generation (SHG) in plasmas. Using the continuity and force equations, derived in Section 1.6 (Equations 1.20 and 1.21), to describe the plasma motion during the interaction with light, we can use successive approximations of the electron density and velocity to obtain a dependence of the second order current density responsible for second harmonic (SH) emission. Expanding the electron density and velocity as $n_e = n_e^{(0)} + n_e^{(1)} + \dots$ and $\vec{v} = \vec{v}^{(0)} + \vec{v}^{(1)} + \dots$, where $n_e^{(i)}$ and $\vec{v}^{(i)}$ are the i th order approximations,

respectively, and using the fact that the current density $\vec{J} = -en_e \vec{v}$, the second order current density can be approximated by [83],

$$\vec{J}_{2\omega} = -e\left(n_e^{(0)}\vec{v}^{(2)} + n_e^{(1)}\vec{v}^{(1)}\right). \quad (3.1)$$

Substituting $\vec{J}_{2\omega}$ back into equations 1.20 and 1.21 and using Maxwell's equations, one can obtain $\vec{J}_{2\omega}$ as a function of the electric field, given by

$$\vec{J}_{2\omega} = \frac{in_e^{(0)}e^3}{4m_e^2\omega_0^3} \nabla(\vec{E} \cdot \vec{E}) + \frac{ie^2}{m_e^2\omega_0^3} \left(\frac{\nabla n_e^{(0)} \cdot \vec{E}}{1 - \frac{\omega_p^2}{\omega_0^2}} \right) \vec{E}, \quad (3.2)$$

where $n_e^{(0)}$ is the unperturbed electron density, and $\nabla n_e^{(0)}$ is the longitudinal electron density gradient [84]. The second order current density, $\vec{J}_{2\omega}$, now acts as source for second harmonic generation in the plasma. The first term of Eq. 3.2 originates from the gradient of the intensity of the electric field. The second term describes the component of the SH current parallel to the local electric field and is proportional to $\nabla n \cdot \vec{E}$. Since SHG is found to occur predominantly at the critical density (n_{cr}) where $\omega_p = \omega_0$, the second term is expected to dominate. This equation represents the resonant absorption (RA) mechanism for SHG, where a transverse electromagnetic wave can mix with a longitudinal plasma wave at the critical density, generating the nonlinear current $\vec{J}_{2\omega}$. Additionally, while the main portion of this SH wave is reflected, a portion of it can travel up the plasma density profile, exciting longitudinal plasma waves at $4n_{cr}$, which can mix to create a 3rd harmonic wave. This process can continue up to the maximum density of the plasma, thereby creating higher-order harmonics.

The second mechanism for harmonic generation is effective in a plasma having very steep density gradients of $L/\lambda_0 < 0.1$, where L is the plasma scale length, and λ_0 is the laser wavelength. These plasmas are well-approximated by a simple step profile and are assumed to be overdense ($n_e \gg n_c$), such that they act as a mirror reflecting incident light. The interaction of this plasma with light generates a periodic motion of the plasma mirror. A generalized model for this motion, known as the oscillating mirror model, was described by Bulanov et al. [85]. The model assumes that ions can be treated as a stationary background because they are much heavier, and the duration of the light pulse is sufficiently short. Furthermore, the electrons that are pushed and pulled by the electromagnetic force generate a collective motion of the reflecting surface constituting an oscillating mirror. Although the mirror motion is highly complex, for simplicity we consider a harmonic motion for the position of the mirror as $\xi(t) = \xi_s \sin \omega_0 t$ [86]. The reflected electric field is therefore emitted from this harmonically moving surface, and, omitting constant phase factors, can be approximated by

$$E_r = E_L \sin(\omega_0 t_{\text{ret}}), \quad (3.3)$$

where $t_{\text{ret}} = t - \frac{\xi(t)}{c}$ is the retarded time at the observation point. Substituting for $\xi(t)$, we find

$$E_r = E_L \sin\left(\omega_0 t - \frac{\omega_0}{c} \xi_s \sin \omega_0 t\right), \quad (3.4)$$

which shows the characteristic anharmonic wave form. Analysis of this field allows one to compute the harmonic spectrum, which can be expressed in terms of Bessel functions, consisting of harmonics at multiples of the oscillator driving frequency. For obliquely incident p-polarized light, it can be shown that this electron boundary is driven at ω and 2ω resulting in even and odd harmonics. For s-polarized light, oscillations are driven only in multiples of 2ω generating only

odd harmonics [87]. S-polarized light can still generate even harmonics through a mechanism unrelated to phase modulation but instead due to the charge distribution set up by the oscillating electron boundary in the presence of a static ion background. In this case an electric dipole sheet is formed in which obliquely incident s-polarized light can drive oscillations at 2ω that will radiate SH light [87].

While there are a considerable number of experiments exploring laser-induced HG from solid targets, many of the results are conflicting. Some of these inconsistencies are a result of the differences in the experimental parameters such as pulse duration and intensity, while others remain unexplained. One of the more extensively studied problems is the effect of a preformed plasma on HG efficiency. This preplasma is generated by either an intrinsic prepulse of the laser system or by a controlled pulse, split from the original beam. A general consensus can be found between previous experiments if the results are split into two groups governed by their intensity range. In experiments with intensities less than $\sim 5 \times 10^{16} \text{ W/cm}^2$ there is an optimum delay between the prepulse and the main pulse for SHG, usually around 5-10 picoseconds [73, 74, 88, 89, 90, 91, 92]. It has been determined that on this time scale the plasma can expand to an optimum electron density gradient scale length at the critical density for resonance absorption. Most of these studies found enhancement of the harmonic emission by a factor of $\sim 2-3$ compared to a single pulse of equal intensity. For intensities greater than $\sim 10^{17} \text{ W/cm}^2$ plasma formation before the main pulse is detrimental to HG, commonly resulting in an exponential decrease in efficiency with increasing scale length of the plasma [93, 94, 95]. The authors of these studies explain that harmonics are created on a steep density gradient that is destroyed by the expansion of the plasma.

Many experiments have also investigated the effect of the polarization state of the driving laser on HG efficiency. According to Eq. 3.2, the dominating second term is dependent on $\nabla n \cdot \vec{E}$. Since the gradient of the electron density is normal to the surface, only the p-polarized component of the electric vector will contribute to the generation of the second harmonic. For an s-polarized laser, the much less efficient first term of Eq. 3.2 is responsible for SHG. Transverse gradients of the electric field due to finite spot size and intensity inhomogeneities in the focal region will give some p-polarized characteristic to s-polarized light, which will give some contribution to the overall SHG. Particle-in-cell (PIC) simulations predict that light polarized in the plane of incidence (p-polarized) should be ~1-2 orders of magnitude more effective in producing harmonics than light polarized perpendicular to the plane of incidence (s-polarized) [86]. The results of experiments on the dependence of HG on laser polarization have shown extreme differences, some yielding multiple orders of magnitude higher production for p-polarized lasers [92, 96], while others have shown little or no difference at all [97]. The majority of the literature does show, however, that p-polarized light is generally ~4-25 times more effective than s-polarized light at moderate intensities (10^{15} - 10^{16} W/cm²) [73, 74, 90, 98, 99, 100, 101]. It has been determined that at higher intensities harmonic generation is much less dependent on laser polarization [99, 102]. Some attention has also been given to the polarization of the harmonics. The first term of Eq. 3.2 dictates an SH emission that follows the polarization of the laser, whereas the second term allows only p-polarized emission. Therefore, for a purely s- or p-polarized laser only p-polarized emission is expected, whereas for an a mixed polarization beam a mix of polarizations is predicted. This prediction has been found to hold in moderate intensity experiments for pulse durations <500 fs [73, 74], but for experiments with longer pulse durations or higher intensities the polarization of the harmonics was found to more closely

follow the laser polarization with a varying amount of residual p-polarized light [96, 100, 101, 102].

Another important aspect of HG is the angular distribution of the HG emission. Eq. 3.2 predicts that HG should be emitted in the direction of the specular reflection of the fundamental beam, which follows from the conservation of the wave vector components parallel to the surface [74]. Again, theory was upheld in experiments with shorter pulse duration lasers at moderate intensities [73, 74, 92, 96, 101], whereas it has been found that at higher intensities the HG emission gradually becomes more diffuse [95, 99, 102, 103]. Chambers et al. showed that the introduction of a prepulse can cause significant broadening of the angular distribution of harmonics as well [104]. Deviation from the predicted HG efficiency and emission properties have most commonly been attributed to a rippling of the critical surface caused by the extreme radiation pressure of the incident light impinging on the expanding plasma, effectively blurring the distinction between s- and p-polarized light and reflecting light over a broad angular distribution.

In an attempt to better characterize the HG processes in the moderate intensity regime ($10^{14} - 10^{16} \text{ W/cm}^2$), we have tried to explain the discrepancies between the previous experiments. We use a controlled, fixed energy, ~65 femtosecond prepulse split from the main pulse. The delay of this pulse can be controlled so as to investigate different plasma parameters. We show how HG efficiency and emission characteristics depend on laser polarization, intensity, and the interaction of light with an expanding plasma profile.

3.2 Experimental Methods

The apparatus used in these experiments is shown schematically in Figure 12. Pulses of ~65 fs duration were generated by a Ti:Sapphire laser (Spectra Physics Tsunami oscillator and Spitfire amplifier). The output of the regenerative amplifier had a peak intensity at 800 nm and a bandwidth of 24 nm (full width at half maximum), falling to 1% at 770 and 830 nm. A half-wave plate and polarizer were used to reduce the pulse energy, E , to within the range of 1 - 100 μJ , with a shot-to-shot variation of less than 3%. This pulse was then split into two equal sub-pulses by a Mach-Zehnder type interferometer. In this setup, the main pulse is first split by a beam splitter. One of the arms of the interferometer contains a translation stage which can vary the path length such that one of the sub-pulses must travel a longer distance before they are recombined by a second beam splitter. The interferometer enabled the two sub-pulses to be separated in time by a maximum of 110 ps. The energy of each sub-pulse is controlled by a variable neutral density filter within each arm of the interferometer. One of the interferometer arms also contains a half-wave plate to change the polarization of its sub-pulse. Once the sub-pulses are recombined the pulse pair is directed through a second half-wave plate where the final polarization state is selected. In this way the energy and polarization of each sub-pulse can be varied independently. The pulses are then focused onto a Si(111) sample by a microscope objective lens (10x, $NA = 0.25$). The radius of the focused beam, ω_0 , was measured with a scanning knife edge and was found to have a value of $1.8 \pm 0.2 \mu\text{m}$. This quantity is the Gaussian radius of the electric field, corresponding to an irradiance of

$$I(r) = I_0 e^{-2r^2/\omega_0^2}, \quad (3.5)$$

and a peak fluence of

$$F = 2E \cos \theta_{in} / \pi \omega_0^2, \quad (3.6)$$

where θ_{in} is the angle of incidence. The sample was mounted on an automated sub- μm precision xyz translation stage. The stage advanced $100 \mu\text{m}$ between laser shots to expose a fresh surface for each pulse, with an average of 10 shots taken for each data point.

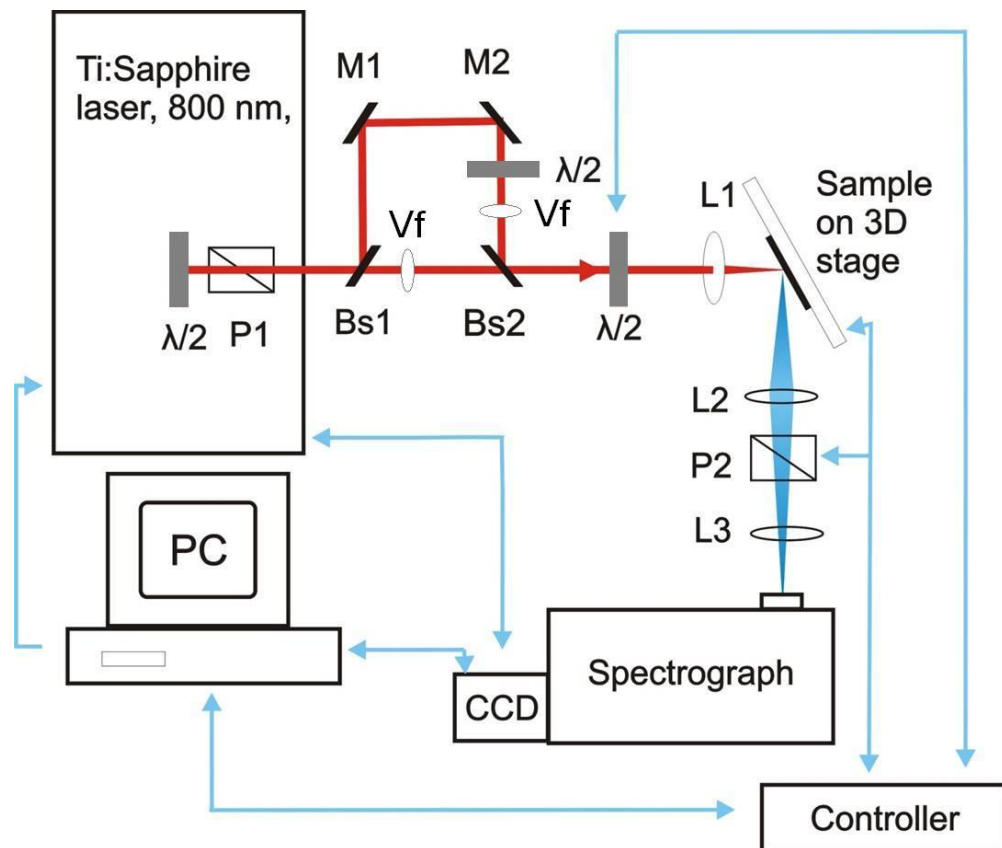


Figure 12 Schematic drawing of the experimental apparatus including half-wave plates ($\lambda/2$), polarizers (P1 and P2), beam splitters (Bs1 and Bs2), variable neutral density filters (Vf1 and Vf2), interferometer mirrors (M1 and M2), and lenses (L1, L2, and L3).

A 1 inch lens, allowing a half-cone angle of $\sim 12^\circ$ measured from the target, focused the light emitted from the laser-induced plasma onto an $800 \mu\text{m}$ entrance slit of a spectrograph (Spectrapro 2300i, Princeton Instruments), in which the spectrum was dispersed by a 300 lines/mm grating blazed at 500 nm, and was recorded with a non-gated, thermoelectrically cooled CCD (PIXIS 400, Princeton Instruments) camera. A notch filter (Chroma Technology, E690SPUV6) was used to block scattered laser light. The filter transmitted $>85\%$ of the emitted light between 390 nm and 595 nm and rejected the laser light with transmittances of 1.1×10^{-6} , 2.2×10^{-6} , and 2.2×10^{-5} at 770, 800, and 830 nm, respectively.

3.3 Results

Figure 13 shows a typical plot of SHG signal versus delay between the prepulse and main pulse, using Si(111) as the target. Here the prepulse was s-polarized with an intensity of $3.1 \times 10^{15} \text{ W/cm}^2$, and the main pulse had twice the intensity. The maximum SH signals for each condition are normalized to unity. In the case of detection at the angle of specular reflection, the intensity of the SH signals for both s- and p-polarized pulses have a steep rise at ~ 10 ps delay. The signal then drops within ~ 7 ps and levels out to a value slightly higher than that obtained a few ps before the steep rise. For nonspecular detection a much weaker dependence on delay is seen. At early times ($t < 10$ ps) the signal remains fairly constant and then begins to rise steadily up to a maximum value around 30 ps. For an s-polarized main pulse the signal plateaus at this maximum for the duration of the experiment up to 60 ps. The p-polarized main pulse exhibits more similar behavior to that found for specular detection, except that the peak in SHG is much broader and occurs at a much later time. Also, the drop in signal after the maximum is less extreme than for specular detection. In order to analyze SHG behavior at very early times in the plasma evolution, the delay time step size was reduced to 133 fs. Figure 14 shows this delay

scan, using BK7 glass as the solid source material, with equal prepulse and main pulse intensities of $4.7 \times 10^{15} \text{ W/cm}^2$. Both pulses had the same polarization, and the signal was recorded at the specular angle. For p-polarized pulses, a sharp spike was seen at $\sim 400 \text{ fs}$ with a FWHM of only 140 fs . When s-polarized pulses were used, the early spike was no longer seen and the behavior was similar to that of the SH generated on Si. This result reproduces well the experiment performed by von der Linde et al. [74]. Experiments using Si showed similar behavior, but the early spike was much less intense in this case.

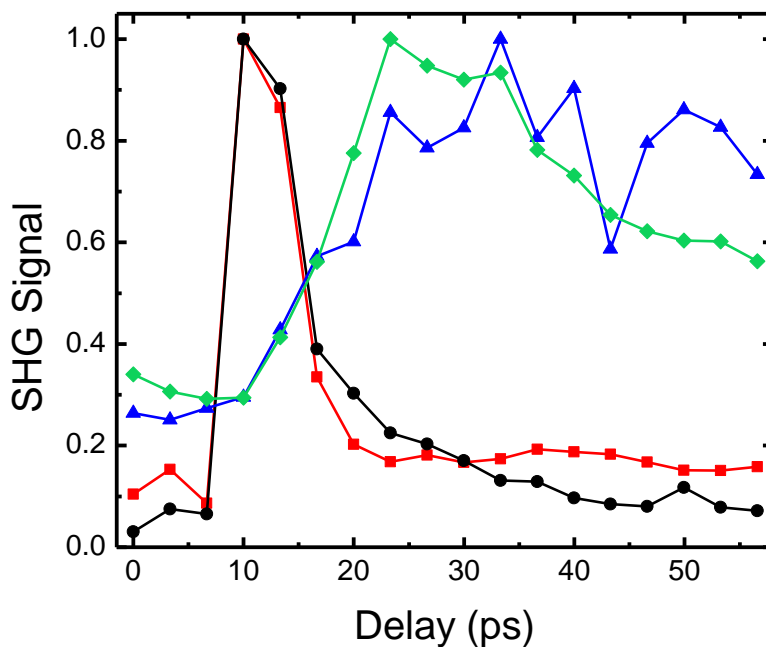


Figure 13 SHG signal (at 400 nm) with Si target recorded using double pulses with a variable delay and step size of 3.3 ps. The first pulse was always s-polarized with an intensity of $3.1 \times 10^{15} \text{ W/cm}^2$ and the delayed pulse had twice that intensity. The signal was recorded at the specular angle for an s- (red squares) and p-polarized (black circles) delayed pulse, or detected 30° from the specular angle for an s- (blue triangles) or p-polarized (green diamonds) delayed pulse. The maximum signal for each data set is normalized to unity.

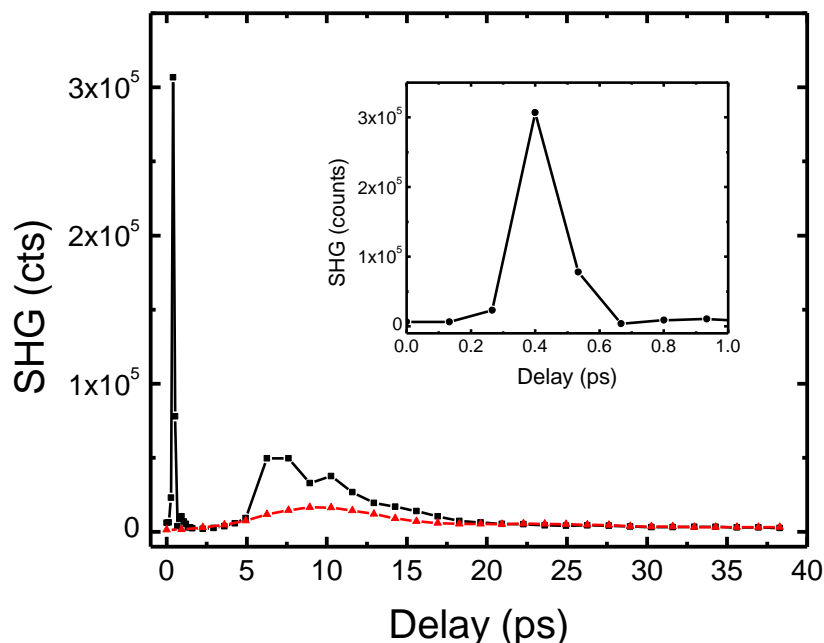


Figure 14 SHG signal with BK7 target recorded with double pulses with a variable delay and a step size of 133 fs, recorded at the specular angle. Both pulses had an intensity of $4.7 \times 10^{15} \text{ W/cm}^2$. The polarization of both pulses was either s- (red triangles) or p-polarized (black squares). The inset shows the behavior of the SHG signal for p-polarized pulses separated by less than 1 ps.

The enhancement of SHG efficiency with double pulses compared to single pulses was found to be strongly intensity dependent. Figure 15 shows that in the specularly detected double pulses were ~ 36 and ~ 16 times more effective than single pulses in the lower intensity regime of our experiments for p- and s-polarized pulses, respectively. At higher intensities this enhancement dropped to ~ 10 and ~ 6 for p- and s-polarized pulses. The optimum delay time between pulses for SHG was also seen to vary with laser intensity, as seen in Figure 16, increasing to longer delay times as the laser intensity was increased past $\sim 10^{16} \text{ W/cm}^2$. This

effect was observed with Si targets as well as 500 nm Ag films coated on an Al substrate. For s-polarized pulses the difference between Si and Ag targets is not significant, but for p-polarized pulses the optimum delay for SHG is longer for the Ag sample with $I > 7 \times 10^{15} \text{ W/cm}^2$.

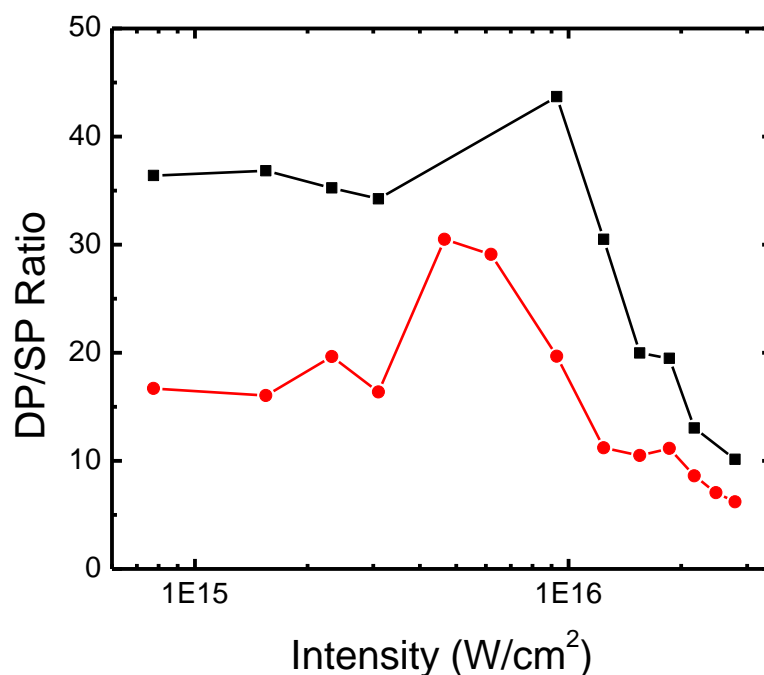


Figure 15 Ratio of SH signal at varying intensity with Si target detected at the specular angle using s- (red circles) and p-polarized (black squares) double to single pulses of equal total intensity. For double pulses the first pulse was always s-polarized with an intensity of $3.1 \times 10^{15} \text{ W/cm}^2$.

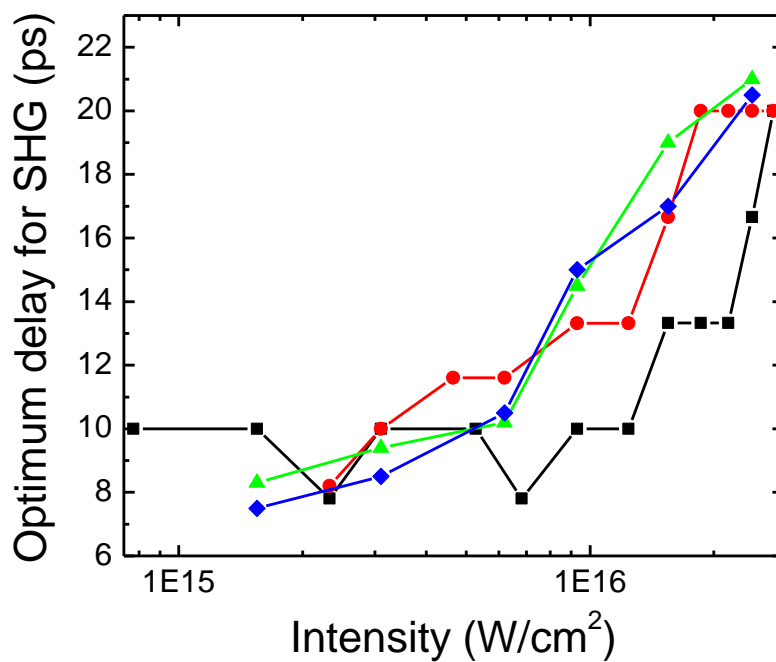


Figure 16 Delay between double pulses for maximum SHG with the same conditions as Figure 15 using a Si target with s- (red circles) and p-polarized (black squares) or a Ag target with s- (blue diamonds) and p-polarized (green triangles) laser pulses.

As expected, p-polarized light was more effective than s-polarized light at generating SH. For single pulses this ratio was ~4:1, in good agreement with previous experiments. For double pulses detected in the specular direction, this ratio more than doubled to 9:1 at the optimum delay for SHG. In the nonspecular direction the dependence on laser polarization was much weaker, where it was found that p-polarized light was only twice as effective as s-polarized light for SHG. In the specular direction this ratio maximized at the optimum delay between the pulses for SHG. At other delays p-polarized pulses were generally 2-5 times more efficient than s-polarized ones. For nonspecular detection no obvious maxima were seen with respect to delay. These ratios remained fairly constant throughout the investigated intensity range.

Figure 17 shows the dependence of the SHG signal ($I_{2\omega}$) on the intensity of the laser (I_ω) at an incidence angle of 30° . In panel (a) only a single pulse was used as the intensity was varied from 7.8×10^{14} to 2.8×10^{16} W/cm². The detector was placed at the angle of specular reflection for the fundamental beam. For both s- and p-polarized laser pulses it was found that $I_{2\omega}$ varied quadratically with I_ω up to the maximum intensity. This is in good agreement with previous experiments without a prepulse, where the dependence on I_ω^n usually gave values of n between 1.5 and 2.5 [73, 74, 97, 98, 99, 101]. Panel (b) shows the same dependence of $I_{2\omega}$ on I_ω , but in this case a pair of pulses were used. The detection geometry was also specular here. The prepulse was always s-polarized and the intensity was fixed at 3.1×10^{15} W/cm², while the main pulse was varied through the same intensity range as in the single pulse case. For each data point the delay between the prepulse and the main pulse was varied from 0 to 60 ps in 1.67 or 3.33 ps increments. The data points represent the maximum SHG signal obtained during the scan through different delays using the value in the longer delay regime (5-50 ps), as opposed to the very short delay spike observed in the inset of Figure 14, which was found to have significant variations in intensity. It is seen that for $I_\omega < 10^{16}$ W/cm² $I_{2\omega}$ varies quadratically with I_ω but at higher intensities the slope decreases significantly. Panel (c) shows the same experimental parameters as in panel (b), but with the detector placed 30° from the angle of specular reflection. Although here the dependence on I_ω^n gives a value of n slightly less than 2 for intensities less than 10^{16} W/cm², the difference is not significant. Similar behavior for specular detection is seen at higher intensities, but here the SHG signal intensity seems to change very little as the intensity of the 2nd pulse is increased. In the nonspecular direction the SH emission for single pulses was barely detectable over the continuum background of the plasma emission.

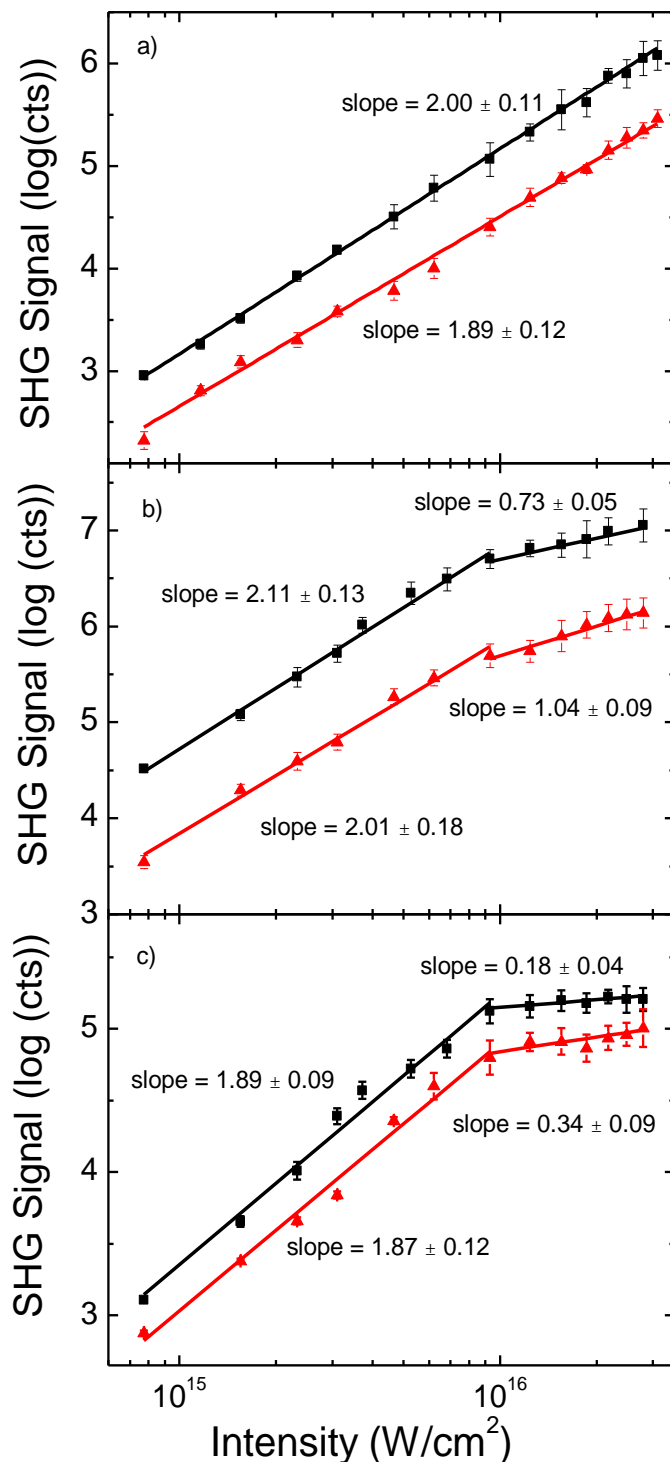


Figure 17 SH signal with Si sample detected at the specular angle for single pulses (panel a), double pulses (panel b), and detected 30° from the specular angle with double pulses (panel c). The symbols are the experimental data using s- (red triangles) and p-polarized (black squares) pulses. The lines correspond to the best linear fit of the data from which the indicated slopes are calculated.

The SH emission characteristics also showed an interesting dependence on the experimental parameters. Making the reasonable assumption that the SH emission retains the original Gaussian shape of the laser pulse after focusing, it is possible to determine the expected angular distribution of a specularly reflected SH beam. SHG is a second-order nonlinear process, already shown to vary with the incident laser intensity as I^2 . Therefore, the divergence, θ_0 , should be proportional to $\theta_0^{1/2}$ of the reflected fundamental and can be calculated as

$$\theta_0 = \frac{2\theta}{\sqrt{\ln \frac{I_s}{I_{ns}}}} \quad (3.7)$$

where θ is the angle of detection in radians, with respect to the specular angle, and I_s and I_{ns} are the intensities of the SH emission measured at the specular and nonspecular angles, respectively. An intrinsic divergence is introduced by the focusing of the incident laser, and for the SH it is calculated to be 0.19 radians. We tested this value by moving the sample to a position much further than the focal distance of the lens, essentially reducing the on-target fluence below the plasma formation threshold. When no plasma was seen to be formed, a SH emission interpreted as being generated at the surface of the target was clearly seen. The angular distribution was measured by scanning the SH signal, produced by a single pulse, across the entrance slit of the spectrometer using a precision micrometer stage. Figure 18 shows the result of this measurement as well as the calculated angular distribution assuming a Gaussian beam focused through our lens with an NA of 0.25. The agreement is fairly good, and the divergence was found to be invariant to changes in intensity or even the use of double pulses. In comparison, Figure 19 shows the divergence of the SH generated by double pulses calculated using Eq. 3.7. It is obvious that the divergence is significantly larger than what would be expected from a well-collimated, specularly-reflected beam. Interestingly, s-polarized pulses have a considerably

higher divergence than p-polarized pulses, and both show a slight decrease with increasing intensity.

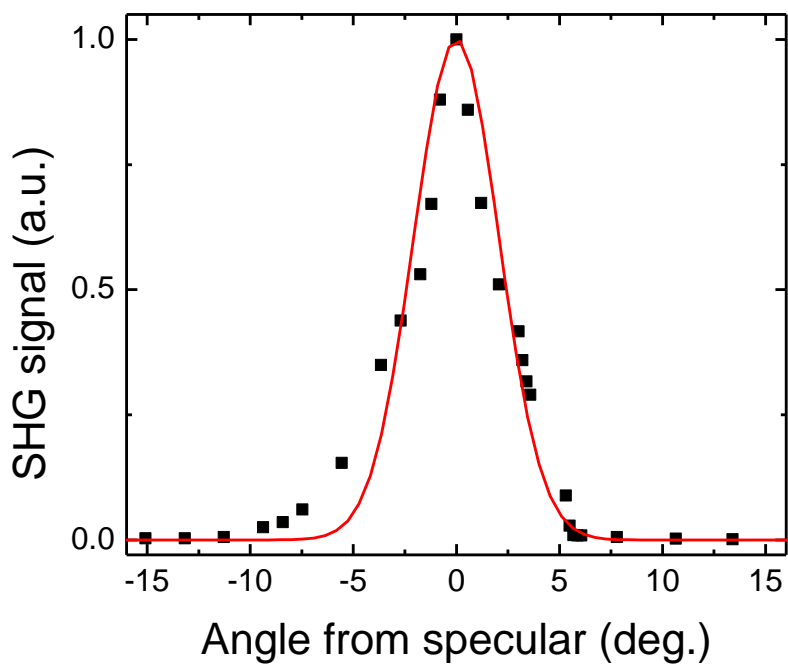


Figure 18 Symbols represent the surface SHG with Si sample recorded at varying angles of detection and normalized to unity. The curve corresponds to the calculated angular distribution of a SH signal, assuming a normalized Gaussian distribution, created at the surface of the target with a divergence introduced by the focusing lens with an NA of 0.25.

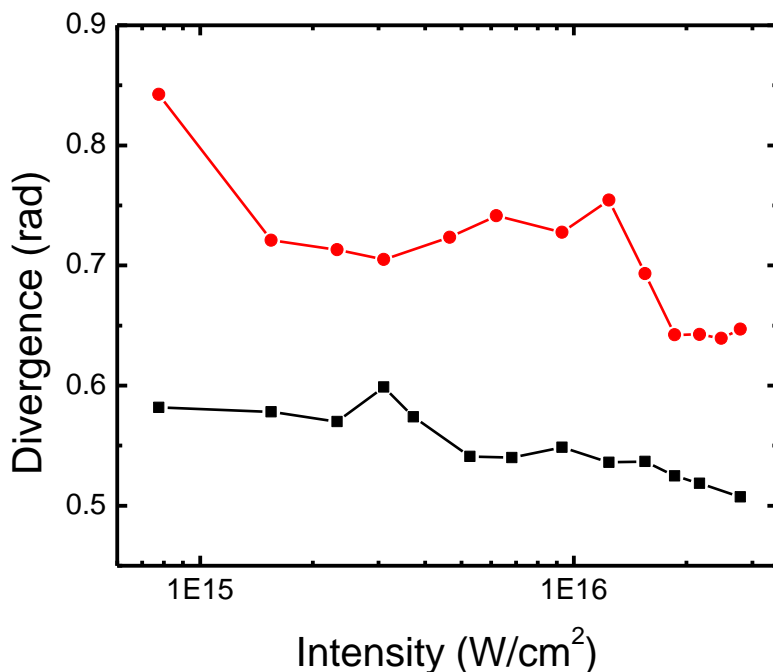


Figure 19 Divergence of the SH signal for s- (red circles) and p-polarized (black squares) double pulses. The delay between pulses was set to the optimum value for SHG. The experimental conditions are the same as in Figure 15. The divergence was calculated using Eq. 3.7.

At the lowest intensities the wavelength of the SH emission was found to be exactly half that of the fundamental wavelength, as expected. As the intensity was increased, the SH was found to blue-shift considerably, as seen in Figure 20. The largest shift was seen for p-polarized pulses measured in the specular direction, with a blue shift greater than 5 nm. For s-polarized pulses or nonspecular detection, the maximum wavelength change was only 3-4 nm. The SH wavelength was also seen to change with the delay between the prepulse and main pulse. Figure 21 shows that blue-shifting of the SH increases nearly linearly with delay between the pulses.

This data was taken at the maximum of laser intensity of $2.8 \times 10^{16} \text{ W/cm}^2$ and detected at the specular angle. The change in wavelength decreased as the intensity of the main pulse was decreased and was less than 1 nm for $I_0 < 1.5 \times 10^{15} \text{ W/cm}^2$. P-polarized pulses showed a much stronger shifting than s-polarized pulses, which did not show any significant shifting until $I_0 > 5 \times 10^{15} \text{ W/cm}^2$. For nonspecular detection, both s- and p-polarized pulses showed little dependence of the SH wavelength on the delay between the pulses, where blue-shifts less than 1 nm were measured.

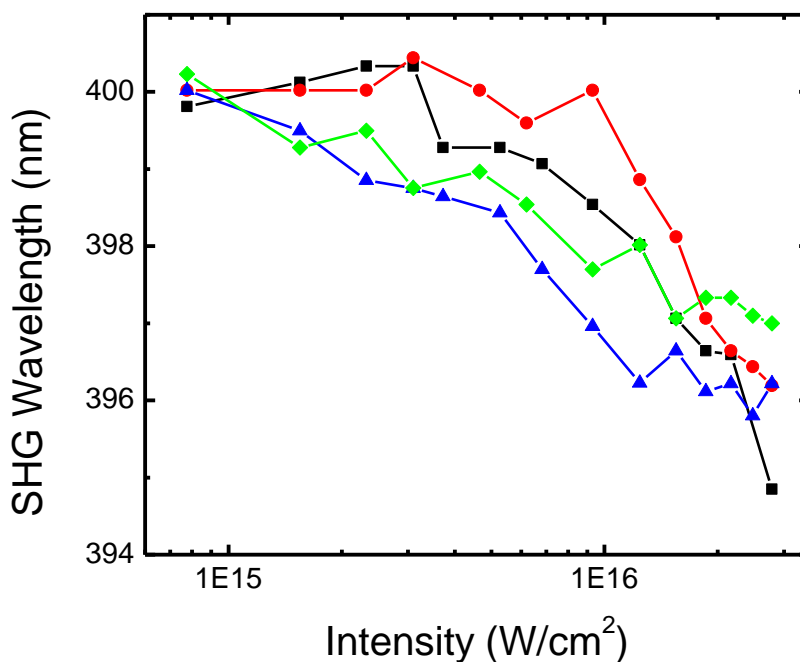


Figure 20 Measurement of the wavelength of the SH emission as a function of fluence using double pulses with an s-polarized first pulse with a constant intensity of $3.1 \times 10^{15} \text{ W/cm}^2$. The data correspond to an average of the SHG wavelength over all delays. The data were recorded at the specular angle with s- (red circles) and p-polarized (black squares) pulses or 30° from specular with s- (green diamonds) and p-polarized (blue triangles) pulses.

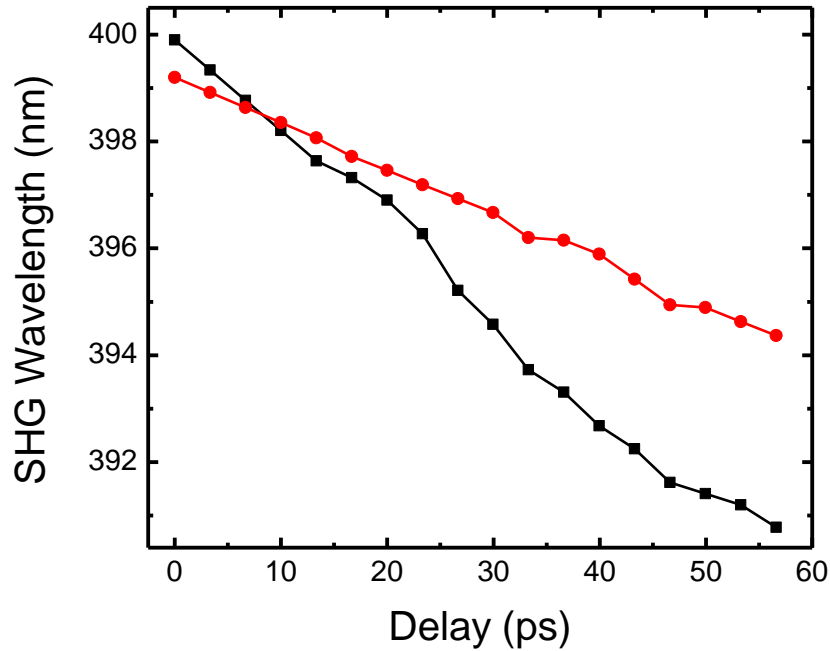


Figure 21 Measurement of the SH emission wavelength using double pulses on a Si target with varying delay. The first pulse was always s-polarized with an intensity of $3.1 \times 10^{15} \text{ W/cm}^2$ while the delayed pulse was s- (red circles) or p-polarized (black squares) with an intensity of $2.8 \times 10^{16} \text{ W/cm}^2$

3.4 Discussion

We now turn to the explanation of the mechanism for SHG in our experiments. The observation that there are two different maxima during the delay scan of SHG indicates that there are at least two different mechanisms creating the SH emission. Since the intensity of the first pulse remains constant, varying the delay of the second pulse essentially controls the conditions of the plasma, such as density and temperature, with which with the second pulse interacts. In

the following discussion, we will focus first on the second, broad maximum in SHG, for which we have the most data.

The expansion velocity of the plasma is usually approximated by the ion acoustic velocity,

$$c_s = \sqrt{\frac{Zk_bT_e}{M}} \quad (3.6)$$

where Z is the ionization state (charge state of the ion) of the plasma, k_b is the Boltzman constant, T_e is the electron temperature, and M is the ion mass. From this assumption one can estimate the density scale length of the plasma, L/λ_0 , from the proportionality $L = c_s t_d$, where λ_0 is the wavelength of the laser, and t_d is delay time between the pulses at the second SH peak. It is well known that the value of L/λ_0 at the critical density of the plasma is a very important factor for determining the efficiency of resonance absorption [23]. Specifically the optimum conditions for resonance absorption are found to occur at [23]

$$\sin\theta \approx 0.8(2\pi L/\lambda)^{-1/3}, \quad (3.7)$$

where θ is the angle of incidence, $L^{-1} = \frac{1}{n_e} \frac{\partial n_e}{\partial z}$, and the electron density, n_e , is measured at the critical density. Assuming an angle of incidence of 30° used in this experiment, Eq. 3.7 predicts $L/\lambda \approx 0.65$.

In the lower intensity regime our results, shown in Figure 16, indicate that a maximum in SHG occurs at ~ 10 ps. If resonant absorption is the cause of this optimal behavior, we would assume that it takes ~ 10 ps for the plasma to expand to a value of $L/\lambda \approx 0.65$. This gives a value for L of ~ 520 nm, for our laser with $\lambda = 800$ nm, which predicts an expansion velocity, $c_s =$

t_d/L , of $\sim 5 \times 10^6$ cm/s. This value is in good agreement with previous estimates [94, 105].

Numerous experiments have been conducted in attempts to determine the functional dependence of the density scale length on time. Quoix et al. [106] used frequency-domain interferometry as well as hydrodynamic simulations for an Al target with a laser pulse of 150 fs and an intensity of 4×10^{15} W/cm² to show that at 8 ps, $L \approx 350$ nm. Unfortunately, 8 ps was the maximum time of their experiment, but extrapolation of their data would put the scale length at ~ 460 nm at 10 ps, in very good agreement with our prediction. The resonant absorption mechanism also fits well with results of other dual-pulse SHG experiments, where a larger angle of incidence led to an earlier optimum delay for absorption than ours [73, 74, 88, 89, 90]. In accordance with Eq. 3.7, a larger angle of incidence results in a shorter scale length for the maximum resonance absorption, and hence less time is needed for the plasma to reach the optimum scale length.

Since the scale length is dependent on the mass of the ion, it is possible to test this hypothesis using a sample of different composition. To do this we used an Ag-coated Al substrate and tested the SHG dependence on delay. Based solely on the mass ratio of Ag and Si and Eq. 3.6, we would expect that the Ag plasma should expand about half as fast as the Si plasma. Figure 16 shows that for a p-polarized laser the delay time for maximum SHG is significantly longer for the Ag sample at higher intensities. The exact ratio varies with intensity, and at a maximum it shows that the plasma expansion is about 50% slower, as expected. It is possible, however, that the plasmas created with these different materials have different ionization states and temperatures, making it difficult to compare expansion velocities directly. For an s-polarized laser the difference between Si and Ag targets is not significant. The explanation for the polarization effect is as of yet unclear.

It is also evident in Figure 16 that the optimum delay for resonance absorption increases with increasing intensity. This variation may be due to the radiation pressure of the laser pushing back the plasma, essentially reducing the plasma scale length. The importance of light pressure in modifying the plasma density profile was first realized by Kidder [107] over 30 years ago. Further theoretical and experimental studies using CO₂ lasers showed that the radiation pressure of the incident laser can counteract the thermal pressure of the plasma, leading to steepening of the plasma density profile [108, 109]. Most of this energy is deposited near the critical surface, resulting in preferential steepening in this region. Using the expression for the pressure exerted by the light on the plasma, given by $P_L = I_0/c$ ($P_L = 1.7$ Mbar for $I_0 = 10^{16}$ W/cm²), and for the plasma thermal pressure, given by $P_e = n_e k_b T_e$, it can be shown that steepening becomes important when the ratio $\frac{41(I_{16})}{n_{23} T_{eV}} > 1$, where I_{16} is the intensity of the laser in units of 10^{16} W/cm², n_{23} is the electron density in units of 10^{23} cm⁻³, and T_{eV} is the electron temperature in units of eV [22]. It is generally accepted that profile steepening occurs in the higher intensity range of our experiment [110]. The optimum delay time begins to significantly increase around 10^{16} W/cm², which means that as soon as the plasma temperature is less than ~2keV, the radiation pressure will start becoming important. Although the plasma temperature is only on the order of a few hundred eV at the delay times we are investigating [111], the duration of the pulse is so short that the effect is probably not significant until this ratio is much greater than unity [86]. Therefore, it is quite possible that at the higher intensities the laser is compressing the density profile, essentially reducing L . This means that the plasma must expand further before the second pulse arrives to reach the optimum scale length for resonant absorption.

The I^2 dependence of the SH is expected from an analysis of the intensity dependence of both mechanisms. The reason why SHG no longer scales quadratically at higher intensities is

still unclear. It is possible that at higher intensities wave-breaking might occur, disrupting the resonantly excited electrostatic wave. At wave breaking amplitudes the electrons are brought into resonance with the wave within a fraction of a plasma period and are accelerated to velocities comparable to the phase velocity of the wave. This results in nonlinear damping of the wave, with most of its energy converted to kinetic energy of electrons. Sandhu et al. [91] found that at intensities of $\sim 10^{16}$ W/cm² there was actually a decrease in SHG at the optimum delay for resonant absorption, which coincided with a significant increase in X-ray production. They attributed this to the damping of the electrostatic wave due to wave-breaking and the subsequent increase in energetic electrons, which are responsible for the X-ray emission. Their intensity for wave breaking matches well with our SHG saturation point. A similar result was seen in a single pulse study by Gizzi et al. [96] in which the polarization of the laser was varied and a decrease in SH emission was seen for purely p-polarized incident light concurrent with an increase in X-ray emission. They also invoked a wave breaking mechanism for these findings.

One large problem still exists for the resonant absorption mechanism to be the cause of this optimum delay time. Resonant absorption requires a component of the electric field to be in the direction of the plasma density gradient in order to induce density oscillations resulting in an electrostatic wave. This means that a purely s-polarized incident beam should not be able to excite these electrostatic waves. We believe that the critical surface is rippled due to a Rayleigh-Taylor-like instability caused by an imbalance of the radiation pressure of the laser with the thermal pressure of the expanding plasma as well as hydrodynamic instabilities inherent in the expanding plasma. These ripples allow density gradients in all directions, such that s-polarized light can effectively participate in the resonant absorption process. Ripple formation has been a commonly invoked consequence of density profile modification by the radiation pressure and has

been shown to produce significant resonant absorption of non-p-polarized light [27, 112, 113, 114]. This mechanism has been invoked in many of the previous experiments where significant SHG by s-polarized light is observed [99, 100, 102]. We tested this hypothesis by measuring the polarization state of the SH emission in which it was found that the polarization state followed that of the incident laser. This polarization dependence is not explainable by either the resonant absorption mechanism or the oscillating mirror model, which both predict that the SH emission should be predominantly p-polarized regardless of the polarization of the fundamental. Further evidence for surface rippling is the apparent diffuse (i.e. non-specular) emission of the SH. Since SHG is essentially a reflection phenomenon, any rippling of the critical surface would result in non-specular emission of the SH signal as well. This is also a common explanation in experiments where diffuse emission occurs [99, 102, 103, 104]. This effect normally becomes important for single pulses with durations greater than 500 fs and intensities around 10^{16} W/cm² or when there is a preformed plasma. The significance of having a preformed plasma is demonstrated by the fact that non-specular emission is significant only for double pulses.

The observation of the SHG maximum at very early delays (~200 fs) has a much clearer explanation. At this early stage in the plasma, the scale length is only a small fraction of the laser wavelength ($L/\lambda < 0.1$) [115, 116]. In these very steep gradients, resonant absorption is no longer effective because the amplitude of the electrostatic wave exceeds the density scale length [110]. These conditions are precisely what are needed for the oscillating mirror mechanism to be effective. Simulations have shown that at the instant a plasma is formed a step-like plasma-vacuum interface exists with electron densities near solid density [86]. This high plasma density prevents efficient harmonic generation, but the efficiency initially grows with L as the plasma expands, until this mechanism becomes inefficient at $L/\lambda > 0.1$ [117]. The rapid expansion of the

plasma could explain the sharp maximum in the SH emission, as the plasma expands from $L/\lambda \sim 0$ to $L/\lambda \sim 0.1$ in the first few hundred femtoseconds. The oscillating mirror model predicts that p-polarized light should be exceedingly more effective than s-polarized light, which is demonstrated by the absence of an SH signal at this early delay for s-polarized experiments. Unlike for the long delay experiments, on this timescale there is not enough time for rippling to occur. While this mechanism is usually invoked in the near relativistic regime for high-order harmonics, it is possible that the low order SH could be created at our intensities. The anharmonic motion of electrons across a steep density gradient is a common explanation in single pulse experiments for SHG in our intensity range [93, 94, 97] and is most likely the explanation of the early spike seen in von der Linde's experiments [74].

The mechanism for blue shifting of the second harmonic signal is most likely due to a self-phase-modulation effect. This effect has been studied for almost forty years since Bloembergen [118] and Yablonovitch [119] first discovered the phenomenon. Self-phase-modulation is a natural outcome of the very rapid production of a free electron gas. Intense fs pulses can cause rapid ionization and therefore a large change in electron density over the duration of the pulse length. As previously discussed, the real part of the index of refraction of the plasma is given by $n_r = (1 - n_e/n_{cr})^{1/2}$. The change in the index of refraction due to an increase in electron density during the ionization of the pulse, results in a blue-shifting of the light according to

$$\Delta\lambda = \frac{\lambda_0}{c} \int_0^L \frac{\partial n(x)}{\partial t} dx, \quad (3.8)$$

where L is the interaction length of the medium through which the pulse travels, and λ_0 is the initial wavelength [120]. The integration of the change in the index of refraction over the spatial

coordinate accounts for the inhomogeneity of the plasma. To actually calculate the expected wavelength shift requires a detailed knowledge of the ionization mechanisms and rates which are beyond the scope of this study. Because the second harmonic signal is generated at the same time as the ionization, its wavelength will be shifted. It follows that as the intensity of the pulse is increased so will the rate of ionization as well as the rate of change of the index of refraction of the plasma, resulting in larger blue-shifts as seen in Figure 20. The dependence of the wavelength shift on delay could be due to the fact that in the time between the two pulses the plasma begins to recombine, and also because low ionization state atoms are being released as a result of ablation. When the second pulse arrives, re-ionizing the recombined and ablation species, it again causes a rapid change in electron density. The electron density will decrease due to recombination as the delay between the pulses increases, resulting in there being a larger fraction of neutral atoms (or ions in low ionization states) available to ionize and a larger change in the index of refraction produced by the second pulse, causing an increase in the wavelength shift, as shown in Figure 21 (We thank Prof. Nathaniel Fisch at Princeton University for suggesting this mechanism). Although the majority of previous experiments concerning plasma-induced blue-shifting are performed with gases, it has been shown that wavelength shifts of 10 nm or greater are readily attainable in our intensity range [121].

4. Femtosecond Laser-Induced Breakdown Spectroscopy Using Temporally Delayed Pulses

4.1 Introduction

The ability of femtosecond (fs) lasers to deposit energy into a material before significant transformation begins has made these radiation sources invaluable in a variety of fields. These lasers have found uses in high precision micromachining [46, 122], 3D microfabrication [123], pulsed laser deposition [124, 125], and medical and biological applications [126, 127]. Aside from these commercial applications, femtosecond lasers have the unique ability to study material processes such as laser absorption, plasma formation, electron-lattice relaxation, phase transformation, and ablation mechanisms with high temporal resolution.

Ultrashort lasers are also becoming increasingly useful in the analytical technique of laser-induced breakdown spectroscopy (LIBS), which has previously been dominated by nanosecond (ns) lasers. While ns lasers have the advantage of more intense spectral lines, fs lasers can provide higher precision [128, 129, 130], increased accuracy [131], and lower background Bremsstrahlung continuum [129, 132]. The increase in accuracy and precision is due to the smaller heat affected zone, which is a consequence of the direct vaporization of the material, rather than ablation occurring through multiple steps, relying on melting and thermal effects. Direct vaporization also makes the ablation process more stoichiometric than when using ns lasers, with pulse durations long enough that they interact with the plasma, ablation plume, and thermally-affected target [131].

Since the LIBS technique is not limited by the number of photons generated for analysis, the main problems with LIBS lie in the sensitivity and limits-of-detection of the measurement [133]. Therefore, to increase the effectiveness of LIBS it is important to maximize the intensity

of the desired atomic emission lines and minimize the background emission. One method for attaining this goal is to split the laser pulse into two sub-pulses and delay the arrival of the second pulse on a variable picosecond timescale to optimize the signal characteristics. This method has been applied to a wide variety of materials, successfully enhancing the analyte signal-to-background ratio ~2-50 times that measured using a single pulse of the same total energy [134, 135, 136, 137, 138]. Other studies, utilizing mass spectrometry, have also found that using double pulses significantly increases the number density and kinetic energy of ions in the ablation plume [139, 140, 141, 142, 143, 144].

One may naively think that the appearance of higher signal intensities and ion yields is due to an increase in the amount of material that is removed by using double pulses versus a single pulse. Contrarily, it has been shown that the use of double pulses does not significantly increase ablation depth or volume, and for pulse separations greater than ~10 ps the second pulse can actually reduce the amount of ablated material created by the first pulse [141, 144, 145, 146]. Consequently, three mechanisms have been previously used to explain the increase in the spectral line emission and ion yield, concurrent with a decrease in ablation efficiency. The first proposed mechanism hypothesizes that the first pulse melts the sample and that the second pulse interacts more strongly with this liquid phase [134, 135, 142, 143]. The second mechanism relies on the fact that the electronic thermal conductivity is proportional to the ratio of the electron and lattice temperatures, such that, as the two components equilibrate, the depth of the thermal energy diffusion changes [139]. In the third mechanism the first pulse creates a plasma with which the second pulse interacts [141, 144, 147, 148]. In this study we hope to increase the understanding of the fundamental processes occurring on a picosecond timescale following the irradiation of a material by an ultrashort laser pulse. We use a multilayer sample of 500 nm of

Ag coated on an Al substrate to examine the spectral characteristics of the plasma and ablation plume. The goal of using this bilayer is to determine if a pair of pulses can penetrate deeper into the sample than a single pulse of the same total energy. By analyzing the plasma emission signal we are able to see what is happening during the plasma evolution as opposed to measuring crater depths long after the excitation.

4.2 Experimental Methods

The experimental setup for this study is nearly identical to that used in the previous chapter on SHG, shown in Figure 12. Briefly, the pulses generated by the Ti:Sapphire laser are directed through a Mach-Zehnder interferometer to create a variably controlled, time-delayed pulse pair, with a maximum delay of 104 ps. The energy and polarization of each sub-pulse can be independently controlled via half-wave plates and variable neutral density filters placed in separate arms of the interferometer. The laser was focused by a 10x, microscope objective lens ($NA = 0.25$). The sample is mounted on a sub- μm precision xyz-translation stage, which is computer controlled to move 100 μm between each shot. Each data point is an average of 10 shots. The light emitted from the laser-induced plasma is collected and focused through a 150 μm slit of a spectrograph (Spectrapro 2300i, Princeton Instruments). The scattered laser light is blocked using a notch filter (Chroma Technology, E690SPUV6).

The main difference from the previous SHG experimental setup is the composition of the sample. Here we used a bilayer sample with a 500 nm layer of Ag coated on a thick Al substrate. The variation in Ag thickness over the entire sample surface is negligible. The thickness for this coating was carefully chosen from a variety of different thicknesses. Ablation experiments were carried out, using single pulses, in our energy range of 1-100 μJ , corresponding to a fluence

range of ~ 20 - 2000 J/cm^2 . It was found, through trial and error, that a thickness of 500 nm of Ag resulted in the ability to see only spectral lines from excited Ag species at low fluence, while at higher fluences, Al lines became apparent as well. This was important, since we wanted to see if double pulses had the ability to excite Al atoms where single pulses could not, and also to be able to investigate the enhancement properties of the spectral lines with respect to fluence.

4.3 Results

Figure 22 shows an example of a single pulse experiment on the 500 nm Ag layer deposited on Al substrate. Here the energy of the pulse is varied, and the spectral intensities of the most intense emission lines (listed in Table II) are plotted at the different fluences. It is evident that the LIBS signal of Al is very weak for fluences below $\sim 1,000 \text{ J/cm}^2$ and that the LIBS signal for Ag varies linearly with fluence over the entire measured range for both s- and p-polarized pulses. In a separate control experiment the signal intensities of the same lines used in Figure 22 were recorded using pure Al and Ag samples. It was found that the Al line was ~ 4 times more intense than the Ag line for single pulses with equal fluence. Taking this calibration into account, the ratio of the Ag/Al line intensities produced from the bilayer sample can be calculated. At fluences capable of producing significant Al emission, the Ag/Al ratio decreases with fluence from ~ 300 at 490 J/cm^2 to ~ 50 at $1,965 \text{ J/cm}^2$. This appears to be a reasonable result, since the Al layer is buried beneath 500 nm of Ag. At lower fluence, the difference in signal intensity using either s- or p-polarized pulses is negligible. At higher fluences, p-polarized pulses give a greater signal. The difference in intensities for the two polarizations increases with fluence, with a maximum augmentation in signal strength for p-polarized pulses of 20% and 60% for Ag and Al, respectively, as compared to s-polarized pulses. This enhancement may be due to plasma absorption mechanisms, predominantly preferring p-

polarized radiation. This hypothesis is supported by the fact that as the intensity is increased a plasma is formed earlier, meaning that more of the pulse is able to interact with the generated plasma.

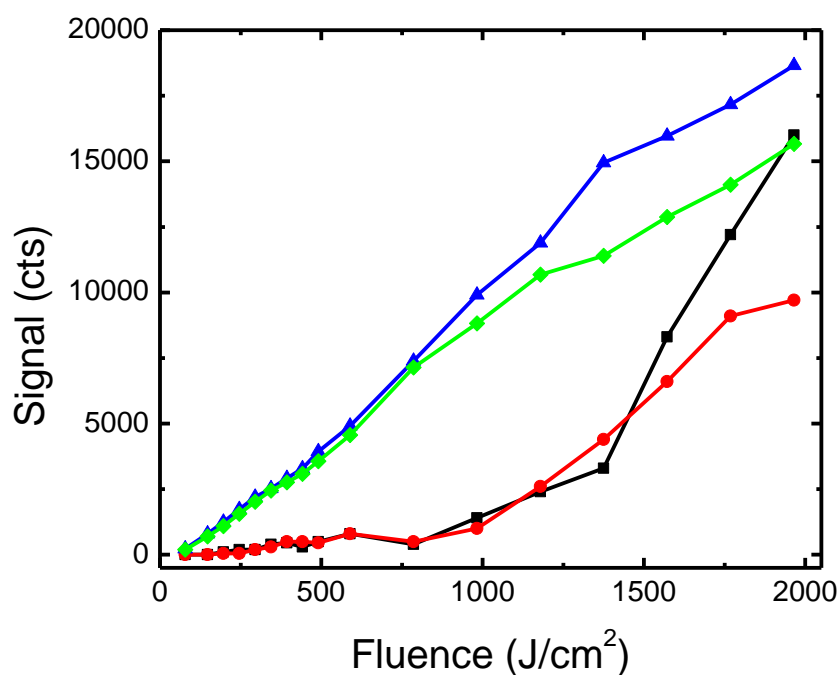


Figure 22 LIBS signal acquired using single pulses on a 500 nm thick coating of Ag on Al. The sample is positioned 30° from normal laser with respect to the laser, and the detector is placed perpendicular to the laser. For Ag using s-polarized (green diamonds) or p-polarized (blue triangles) pulses the data correspond to the strongest spectral emission for Ag in our wavelength range at 546.54 nm. For Al using s-polarized (red circles) or p-polarized (black squares) the data correspond to the strongest spectral emission for Al in our wavelength range at 396.15 nm. The signal for Ag is divided by a factor of 10 to facilitate a visual comparison between the two species.

An example of the full spectra using single or double pulses with a total fluence of $1,965 \text{ J/cm}^2$ is shown in Figure 23. Here the delay of the double pulses is set to its maximum value of 104 ps. The electronic transitions involved are assigned from the NIST atomic spectra database [149] and are listed in Table 1. The total angular momentum quantum number, J , is included in the table, since some of the transitions arise from the same electronic configurations and differ only in the angular momentum state of the excited electron. It is seen that double pulses increase the total signal of the LIBS spectra, including the background Bremsstrahlung continuum. Overall, this represents an increase in the signal-to-background ratio by a factor of 2 when using double pulses compared to single pulses. This result is in good agreement with experiments performed by previous groups at very high fluence [134, 135, 138].

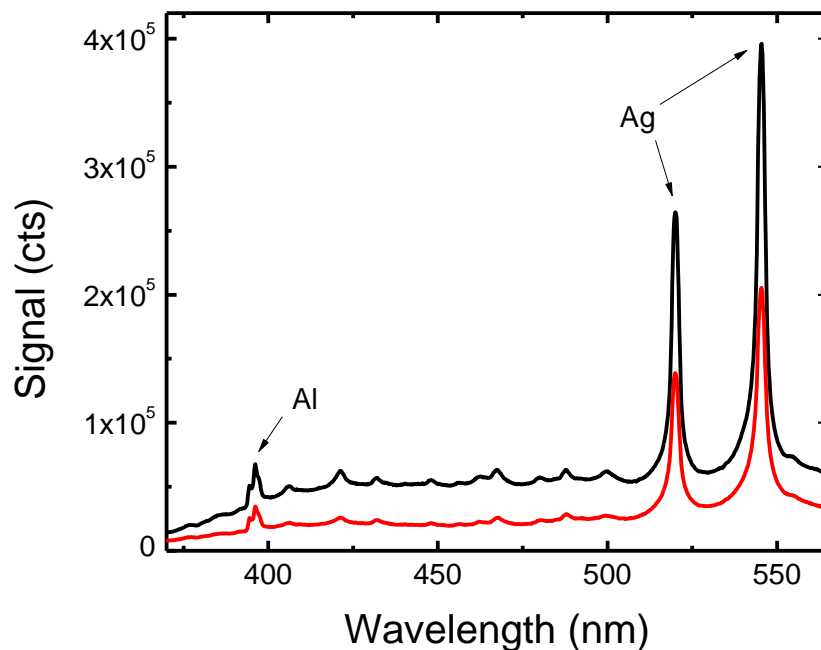


Figure 23 LIB spectra of bilayer sample using a p-polarized laser with a fluence of $1,965 \text{ J/cm}^2$. The incidence and detection geometry are the same as in Figure 22. The black and red curves correspond to double pulses separated by 104 ps or a single pulse, respectively, with the same total energy. The transitions of the labeled peaks are listed in Table II.

Table II ELECTRONIC TRANSITIONS OF ALUMINUM AND SILVER

Ion	Wavelength (nm)	Configuration	J
Al I	394.40	$3s^23p - 3s^24s$	$1/2 - 1/2$
Al I	396.15	$3s^23p - 3s^24s$	$3/2 - 1/2$
Ag I	520.91	$4d^{10}5p - 4d^{10}5d$	$1/2 - 3/2$
Ag I	546.54	$4d^{10}5p - 4d^{10}5d$	$3/2 - 5/2$

Figure 24 shows a more dramatic enhancement effect, characteristic of the lower fluence regime, for single vs. double pulses with both s- and p-polarization. The wavelength range of these spectra is smaller to show the enhancement effects on lines of similar strength. The additional Ag spectral lines are given in Table II [149]. The enhancement ratio (ER), defined as the background-corrected signal created by double pulses divided by that of single pulses, ranges from 2-4 depending on the spectral line and laser polarization. P-polarized laser excitation also shows a higher ER than for s-polarization. This is due to the fact that while s- and p-polarized excitation in the single pulse configuration gives similar total signal intensity, p-polarized double pulses give 30-50% higher signal intensity for all wavelengths including that of the continuum. The advantage of using double pulses is clearly illustrated in the quality of the LIB spectra, in that the atomic emission peaks are much more easily distinguishable against the continuum background signal. Interestingly, the enhancement of the peaks is qualitatively similar for both Ag and Al.

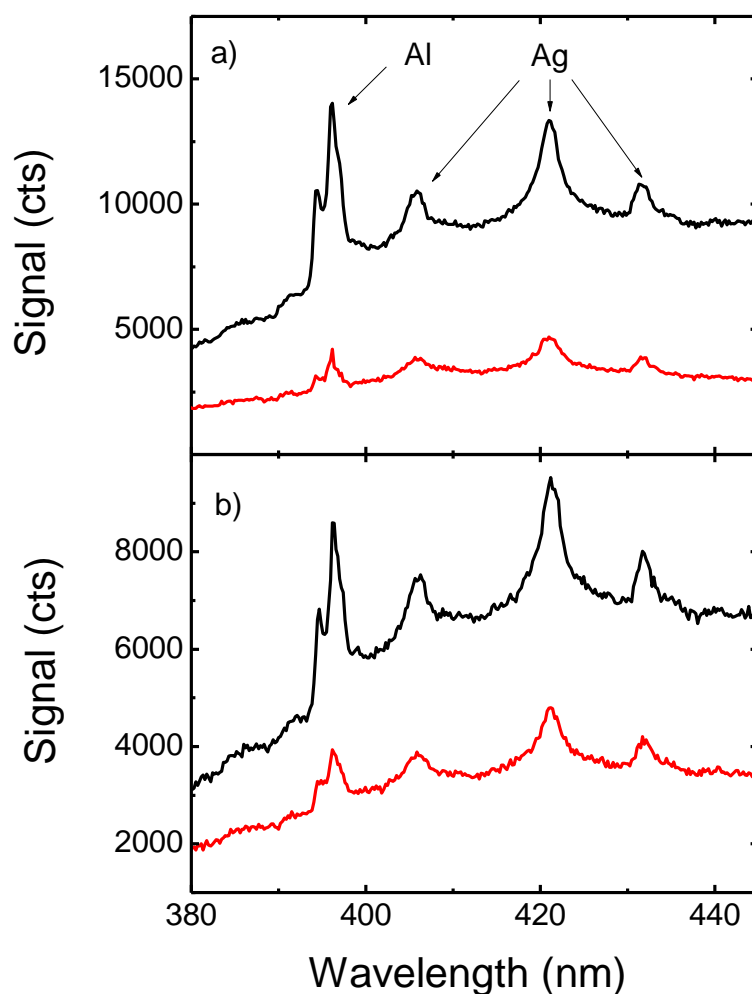


Figure 24 LIB spectra taken with a fluence of 588 J/cm^2 with p-polarized (panel a) and s-polarized (panel b) using single (red curve) and double (black curve) pulses. The incidence and detection geometry is the same as Figure 22. Additional Ag spectral lines are given in Table III.

Table III ADDITIONAL ELECTRONIC TRANSITIONS OF SILVER

Ion	Wavelength (nm)	Configuration	J
Ag I	405.85	$4d^{10}5p - 4d^{10}6d$	$1/2 - 3/2$
Ag I	421.62	$4d^{10}5p - 4d^{10}6d$	$3/2 - 5/2$
Ag I	431.32	$4d^{10}5s5p - 4d^95s6s$	$5/2 - 7/2$

In an attempt to elucidate the mechanism for double pulse enhancement, the ER was measured for the Ag/Al bilayer as a function of delay between the pulses. Figure 25 shows the result of this measurement using both p- and s-polarized pulses at a fluence of 588 J/cm^2 . The data show a clear trend of a quickly increasing enhancement up to 20-30 ps, at which time the ER reaches a plateau, changing very little from 40 ps to the maximum attainable delay of 104 ps. This trend is reproduced for both Ag and Al, and is in good agreement with previous studies by Gordon et al. [134] and Pinon et al [136]. Again, p-polarized pulses show a distinctively higher ER than s-polarized ones. For delays less than 20 ps the difference in ER using p- or s-polarized pulses is a monotonically increasing function of delay, at which point it plateaus on a similar timescale as that of the ER. In the long delay limit, p-polarized pulses show a nearly 50% increase in ER for both Ag and Al as compared to s-polarized pulses. It is also seen that Al has a slightly higher ER than Ag with a difference ranging from 15-25% at pulse separations greater than 20 ps. Fitting of the ER to the functional form of $(1 - e^{(-|t|/\tau)})$, as in [134], gives a time constant, τ , of roughly 20 ps for both Al and Ag using p- or s-polarized pulses.

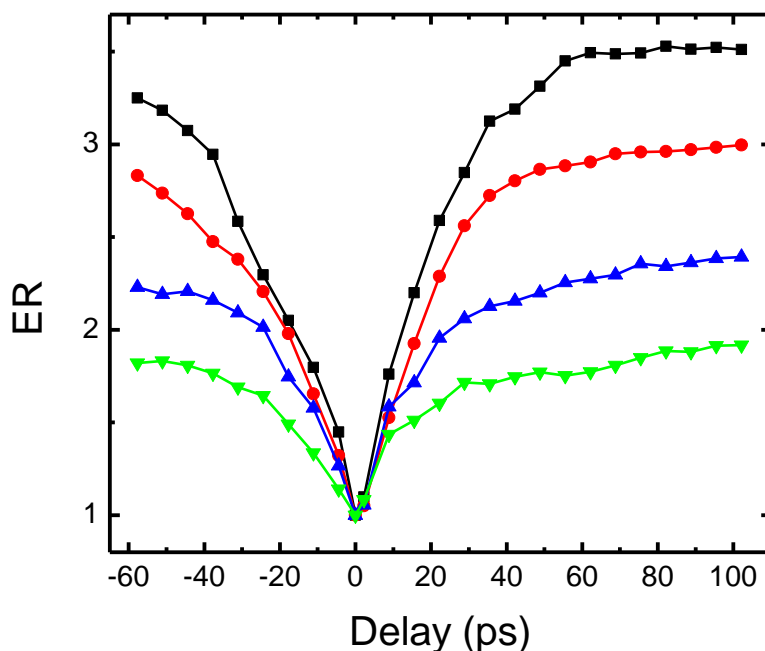


Figure 25 Enhancement ratio (ER), between single and double pulses, of the signal intensity for the Ag line at 546.54 nm and the Al line at 396.15. The data were recorded at a fluence of 588 J/cm². The incidence and detection geometry is the same as that of Figure 22. The data correspond to the use of p/s-polarized pulses for Al (black squares/blue triangles) and Ag (red circles/green triangles).

The dependence of the ER on fluence was also examined. Figure 26 shows the ER measured at the maximum delay of 104 ps using s-polarized pulses. For fluences less than 500 J/cm² it was not possible to accurately measure the ER of Al since the signal intensity was barely above the background level. In the lower fluence regime the ER for Ag rapidly drops from a maximum value of ~9 at the lowest fluence of 49 J/cm² to ~2 at 500 J/cm², where it remains fairly constant at a value slightly less than 2 up to the highest fluence. This behavior is in good agreement with previous results [135, 137, 138]. The ER of Al is always slightly higher than

that of Ag, but the difference is generally smaller at higher fluences. For comparison, the ER of a pure Al sample was also determined.

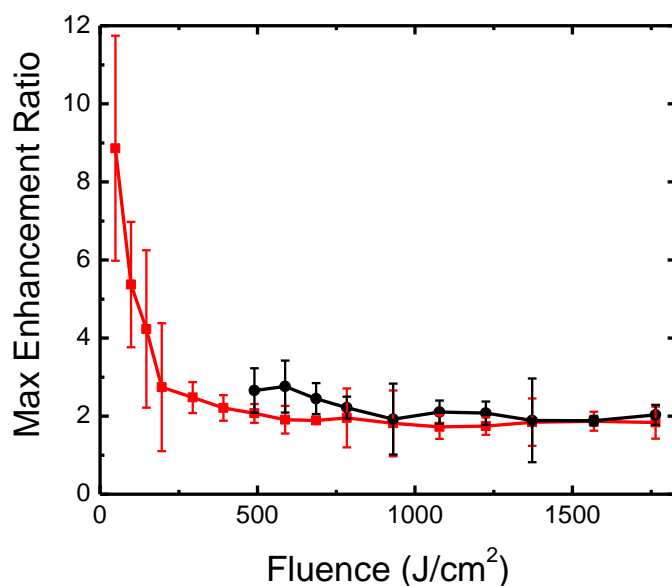


Figure 26 ER obtained at a delay of 104 ps as a function of fluence. The signals analyzed for Ag (red squares) and Al (black circles) are the same as in Figure 25. The error bars represent the standard deviation of the measurement.

The behavior of the enhancement for pure Al was remarkably different than that seen using the bilayer, as shown in Figure 27. At the fluences less than ~ 100 J/cm² the trend in ER was similar to that of the bilayer but was found to only be slightly higher than unity. The

enhancement ratio decreased with increasing fluence, and at the highest fluence measured (490 J/cm²), in this experiment, it was found that a single pulse actually produced higher line intensities than double pulses by a factor of ~1.25. To extend these measurements to lower fluences, we replaced the microscope objective lens with a simple focusing lens, with a spot size nearly ten times greater than that in the previous experiment. This weaker focus allowed measurement of the ER at fluences from 2 to 25 J/cm². At this fluence it was found that there was no noticeable signal from Al when ablating the bilayer sample. Therefore, the experiment on the bilayer with this lens can be approximated as interacting with a pure Ag target. With this lens, a pure Al sample was used to obtain data for the Al emission line enhancement. As shown in Figure 28, the qualitative behavior of the bilayer was recovered in which the ER attained a maximum value of ~10 and ~6 for Ag and Al, respectively, at the lowest fluence. For the pure Al sample, the ER decreased quickly to less than a factor of two at 10 J/cm², whereas the ER for Ag remained high up to ~15 J/cm², finally converging to nearly the same value as that of Al at 25 J/cm².

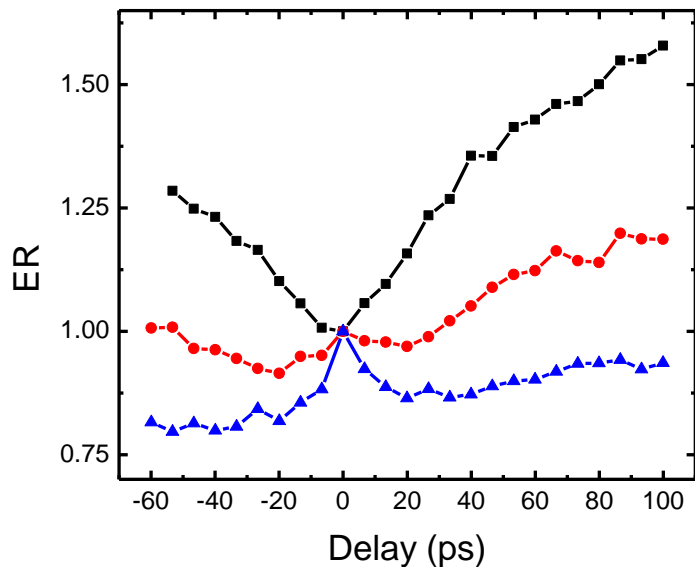


Figure 27 Enhancement ratio (ER), between single and double pulses, using a pure Al sample, of the signal intensity for the Al line at 396.15. The data were recorded at a fluence of 98 J/cm² (black squares), 196 J/cm² (red circles), or 490 J/cm² (blue triangles). The incidence and detection geometry is the same as that of Figure 22.

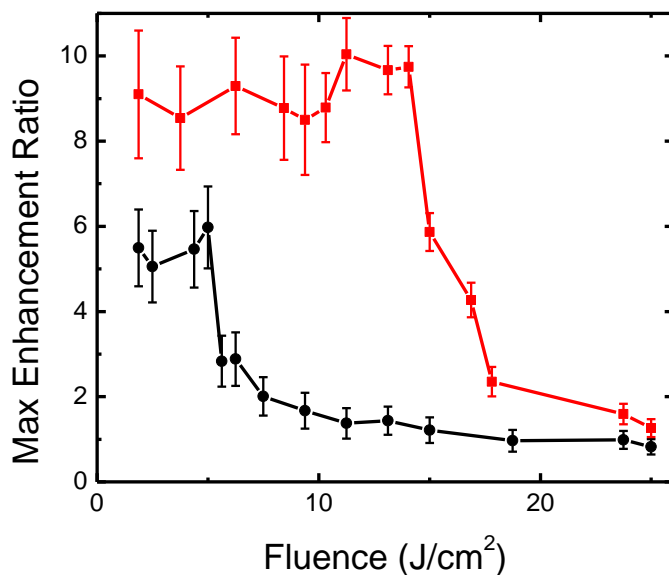


Figure 28 ER obtained at a delay of 104 ps as a function of fluence using a simple focusing lens. The wavelength analyzed for Ag (red squares), using the bilayer sample, and Al (black circles), using the pure Al sample, are the same as in Figure 22. The error bars represent the standard deviation of the measurement.

The time constant, τ , was also measured as a function of fluence. The result of this experiment using the microscope objective lens is shown in Figure 29. Here, again, the time constant for Al was not measurable below 500 J/cm^2 due to the lack of signal. The time constant for Ag varies from $\sim 30\text{-}40 \text{ ps}$ for fluences below 250 J/cm^2 , where it then steadily drops below 20 ps at 500 J/cm^2 . The time constants for both Al and Ag above 500 J/cm^2 show a slow increase from $\sim 15\text{-}20 \text{ ps}$ over the rest of the fluence range. The time constant, τ , was also measured for Al using the simple focusing lens at low fluences. Unfortunately, the maximum delay of 104 ps achievable with our translation stage was not sufficient to observe the plateau region seen in the higher fluence experiments. Although the ER did begin to level out at longer delays, the functional fitting gave values of τ that were longer than 104 ps , making the time constant measurement unreliable.

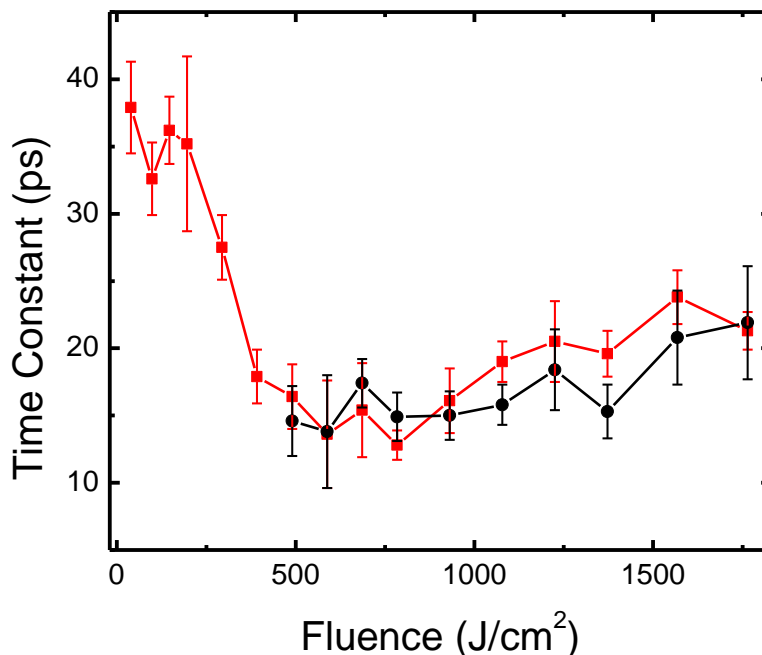


Figure 29 Time constant from the fitting of the function $A(1 - e^{(-t/\tau)})$ to the ER dependence on delay, t , as a function of fluence. The same signals for Ag (red squares) and Al (black squares) were used as in Figure 22. The error bars represent the standard deviation for multiple shots.

The final experiment tested the difference in the spectral signals for pulses separated by times longer than the entire ablation process. To do this, single pulses with a fluence of 100 J/cm² were manually generated and separated by times longer than a few seconds. At this low value of the fluence, a single pulse is incapable of penetrating the Ag film and ablating the substrate. The spectrum from each shot was recorded as shown in Figure 30. For comparison, the spectra of single and double pulses with a total fluence of 200 J/cm² are shown as well. While the first pulse replicates the basic features of the previous spectra, the second pulse in the same spot shows an enormous increase in the Al signal at 396.15, and a decrease in the Ag lines. For pulses separated on the order of 100 ps, the relative intensity (signal/background) of this Al

line is not seen at even the highest fluences. This indicates that even at very low fluences, a single pulse is capable of ablating more than half of the Ag layer, but that the second pulse is unable to sample the underlying material until much longer delays.

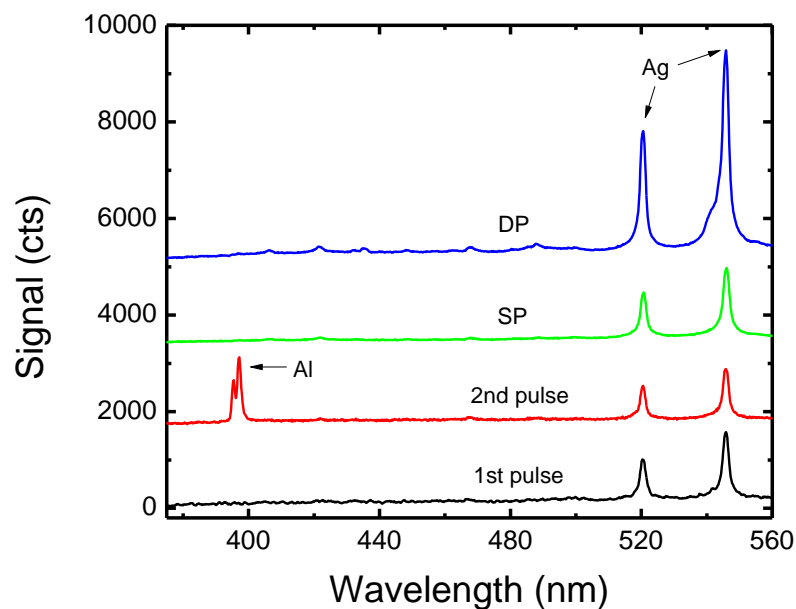


Figure 30 LIB spectra of the Ag/Al bilayer sample. The bottom two traces represent the signal acquired by a single shot of 100 J/cm^2 fired in the same spot separated by a few seconds. The top two curves represent a single shot (SP) and double pulses with a 104 ps delay (DP) with a total fluence of 200 J/cm^2 . The spectra are vertically offset to ease viewing.

4.4 Discussion

It is informative to discuss further the three previously proposed mechanisms for the differences in efficiency of optical emission, ablation, and ion yield when using double pulses as compared to single ones. The first mechanism, known as the liquid absorption model, proposes that the liquid layer generated by the first pulse absorbs energy more efficiently than the solid phase of the target, which would result in a higher energy density and therefore higher temperatures within the material [143]. These higher temperatures would then produce an increase in material removal and generation of excited species, giving an overall enhancement of the emission signal intensity. The liquid absorption mechanism argues that the dependence of the signal enhancement on the delay between the pulses is due to the position of the melt front. After the first pulse, the high temperatures created at the surface propagate into the material melting deeper layers. The initial increase in enhancement with delay is a result of the laser having more liquid to interact with. At some point the liquid layer will exceed the optical penetration depth of the laser and the enhancement will no longer increase [142]. This provided a reasonable explanation of the plateau behavior of the emission signal that is not immediately evident in the plasma reheating model. An explanation for the reduction in ablation efficiency was hypothesized by Singha et al. [135] to be due to the ablation products, created by the second pulse interacting with the ablation plume from the first pulse and then condensing back into the crater. This was evidenced by an increase in amorphous material found within the crater when using double pulses. Another strong argument for this mechanism was the dependence of the ER on fluence. The liquid absorption mechanism predicted that signal enhancement would decrease as the fluence was increased due to increased plasma formation which would block the second pulse from interacting with the liquid phase [135]. Further evidence was given by Hu et al. [134] who showed that at very low fluences the ER actually decreased. They argued that this was

because the lower available energy resulted in a slower melt front and increased resolidification, providing less liquid for the second pulse to interact with.

Although the liquid absorption model provides an adequate prediction of most of the trends in our results, its explanation of the decrease in ablation depth does not coincide with current knowledge of the mechanisms and timescales of ablation. Experiments involving pump-probe microscopy imaging [150, 145] and time-resolved x-ray absorption spectroscopy [151] as well as molecular dynamics simulations [152, 153] all show that the formation of an ablation plume from actual material ejection does not begin until after ~ 30 ps or longer. The liquid absorption mechanism suggests that the ablation plume created by the second pulse would interact with that created by the first pulse, but this interaction could only occur for delays much longer than used in our experiments. Also, the liquid ablation model assumes that at first a deeper crater is formed, due to the better coupling of the laser to the liquid phase. This does not coincide with our results presented in Figure 30, where it was shown that two pulses separated by a very long delay (>1 sec) are able to dig deeper into the sample, where no liquid would be available for the second pulse, than double pulses separated on ps timescale. This was true even for short-delay double pulses with ~ 50 times higher fluence. Although the double pulses are able to enhance the signal, they do not seem to be actually removing more material during the interaction time.

The second mechanism, which has received much less attention, is based on the dependence of the electron thermal conductivity, k_e , on the ratio of the temperatures of the electrons, T_e , and the lattice, T_l . Hohlfeld et al. [154] showed that k_e decreased as the electron and lattice temperatures equilibrated. Noel et al. [139] postulated that at short delays before the electron and lattice could equilibrate, the resulting high k_e would mean that the energy of the

second pulse could penetrate more deeply. This would favor increased nanoparticle production and ablation efficiency. Conversely, as T_e/T_l approaches unity, the electron thermal conductivity would be smaller and the laser energy would be more confined, resulting in a higher temperature gradient favoring increased atomization and smaller ablation depths. The transition from nanoparticle production to atomization would result in a higher optical emission and ion production.

Our experimental results are in sharp contrast with the predictions of the second mechanism. First, the electron conductivity mechanism would predict that k_e , and therefore the confinement of the absorbed energy, should be higher for more intense irradiation. This in turn should cause an increase in atomization and therefore signal enhancement. Instead our results show that the ER actually decreases with increasing fluence. A second consequence of increasing fluence would be to increase the time it takes for the electron and lattice to reach thermal equilibrium and, hence, k_e would remain higher for longer. Again, our results contradict this prediction and show that the time constant associated with the ER versus delay decreases with fluence in the lower intensity regime, and increases only slightly in the higher intensity regime.

The final mechanism, known as the plasma reheating mechanism, was primarily invoked to explain the reduction in ablation efficiency when using double pulses separated by longer than a few ps. Multiple studies have shown that three distinct timescales govern the ablation efficiency of double pulses [141, 144, 147, 155, 148]. For delays less than a few ps the resulting ablation crater depth was equal to that created by a single pulse of same total energy. This is reasonable because the electron-lattice equilibration time, τ_{el} , is on the order of a few ps in metals. This meant that the energy of the first pulse had not been dissipated and no significant

expansion or ablation had occurred by the time the second pulse arrived, such that the energy of the second pulse was absorbed as if the pulses had arrived simultaneously. In the second time domain, the ablation depth for double pulses decreased monotonically with increasing delay up to 10-20 ps, at which point the ablation depth of the double pulse was equal to that created by a single pulse of half the total energy. This indicated that only the first pulse was responsible for ablating the material and that the energy of the second pulse never reached the surface, either being reflected or absorbed by the plasma created by the first pulse. Some studies have shown that the ablation depth of double pulses, separated by more than 10-20 ps, had a smaller ablation depth than a single pulse of half the total energy [144, 146]. This result was explained by Povarnitsyn et al. in terms of the pressures created within the material [146]. They performed a hydrodynamic simulation using a Cu target, mapped the evolution of the pressure within the material, and found that when the first pulse strikes the surface, compressive pressures on the order of tens of GPa are setup. The target responds, creating a rarefaction wave achieving negative pressures within the material on the order of a few GPa after ~20 ps. This negative pressure is responsible for the mechanical spallation of the liquid phase resulting in ablation. When the second pulse arrived later than ~5 ps, it was found that it was absorbed in the nascent ablation plume at the surface of the material. This resulted in the generation of a high-pressure region on the surface and a subsequent shock wave that diminishes the action of the rarefaction wave. The simultaneous enhancement of the plasma and atomic emission, on a similar timescale as the ablation reduction, is attributed to the heating of the plasma, resulting in a plasma with a higher temperature and longer emission lifetime.

Although a complete description of the interaction of double pulses most likely includes a combination of different mechanisms, our results most closely match the predictions of the

plasma reheating model. One of the strongest arguments supporting the plasma reheating mechanism is the trend of the signal enhancement with respect to delay between the pulses. The time constants of the rise of the ER are nearly identical for Al and Ag. One would expect that if the increase in signal intensity were due to an increase in the coupling efficiency of the 2nd pulse to the sample surface, the time constant would be very different for the two layers, inasmuch as it would take much longer to reach the lower Al layer. Instead, the time constant is probably related to the timescale for the formation of the plasma and ablation plumes. Further evidence for this mechanism is found in experiments which have shown that the use of time-delayed double pulses results in a hotter plasma, with longer emission times [137], as well as an increased expansion velocity [140], and luminosity [155]. These plasma characteristics were also seen to increase with delay between the pulses on the same timescale as the signal enhancement in our data.

As previously indicated in Figure 25, Al has a slightly higher ER than Ag for all delays. Since the optical penetration depth in Ag is only ~10 nm [156], and at our intensities the target becomes fully ionized, the Ag layer is much more highly excited than the underlying Al layer, which becomes ionized and excited only through secondary interactions with the plasma. Therefore, at the time of arrival of the second pulse, there is much more unexcited Al than Ag leading to a disproportionate enhancement of the Al signal compared to that of Ag. The effect of fluence on the ER is similarly related to the ability to ionize and excite more of the target material. As the intensity of the pulse is increased, a larger fraction of the material reaches and stays in an excited state, such that the second pulse has less material to excite.

The tendency of the ER time constant to lessen at higher fluences indicates that the formation of the plasma and ablation constituents into an optimum state occurs more quickly.

The fact that the signal enhancement remains fairly constant after ~40 ps, which is also the timescale for the formation of the ablation plume, shows that once material begins to be ejected from the surface the amount of energy that can be absorbed by the plume does not change much. It is only with increasing fluence, expediting the ablation process, that this timescale is shortened.

In conclusion, it seems most probable that the enhancement of the signal intensities in laser-induced breakdown spectroscopy using double pulses is due to the interaction of the 2nd pulse with the plasma created by the 1st pulse. This interaction results in an increase in the number of excited species as well as creating a hotter plasma with a longer emission lifetime. Knowledge of the proper mechanisms governing the ablation and plasma generation processes will undoubtedly improve the usefulness of fs lasers to commercial applications as well as fundamental research.

CONCLUSION

Early studies of light and how it interacted with matter determined the fundamental properties of reflection, refraction, diffraction, and absorption, but the invention of the laser has allowed scientists to explore completely new realms of this interaction where the much higher intensity of laser light gives rise to numerous new phenomena. The laser has revolutionized many aspects of all the scientific fields, as well as creating completely new areas of study that could previously only be analyzed theoretically. The ability of laser light to deposit a large amount of energy into a small volume of a sample and ionize it, resulting in plasma formation and ablation, has led to a close inspection of all how these processes occur. Although the study of plasmas predates the invention of the laser by many years, the ability to create reproducible plasmas on any sample in a controlled laboratory setup is facilitated by the use of a laser. This ability has made laser-induced breakdown spectroscopy (LIBS) an important technique for chemical analysis.

The interest in LIBS has been steadily rising since the mid 1990's where less than ~50 papers, specifically on LIBS, were published annually, to present times where over 500 papers are published each year [7]. This does not account for the many other papers discussing the individual phenomena which occur at each step of the LIBS process. Also, since the year 2000, an international conference dedicated to LIBS is held every two years, showing that there is no doubt that LIBS is becoming a very popular technique, and that it is far from a completed technology. The understanding of processes occurring during the laser-matter interaction such as, absorption, ionization, plasma formation, plasma dynamics, and ablation are still ripe for experimental investigation. The development of ultrashort, high-intensity laser sources has given scientists the ability to study these phenomena on a femtosecond timescale.

CONCLUSION (continued)

The goal of the research presented in this thesis was to solve some of the current problems with LIBS. We first investigated the continuum and discrete plasma emissions and found that the observed partial polarization is due to the reflection of the signal off the molten surface of the sample. Further investigation of this phenomenon may provide a more accurate and time-resolved means of following the phase changes within the sample after irradiation by the laser. The second experiment explored the hydrodynamic evolution of the plasma using a pump-probe technique. By following the generation of the second harmonic as a function of pulse delay, we are able to estimate the expansion velocity and density of the plasma on a sub-picosecond timescale. Changing the intensity of the probe pulse also allows us to study the effects of the competition between the radiation pressure of the light and the thermal pressure of the expanding plasma, as well as the ionization of recombined and ablated species in the plasma. Future experiments employing pump-probe techniques of laser-induced plasmas will invariably provide important information of the processes occurring within these plasmas. Finally, we examined the commonly used technique of dual-pulse LIBS, and determined that the enhancement of the signal intensity was due to the interaction of the second pulse with the plasma. The knowledge of the timescale that the plasma can absorb or block the second pulse from hitting the target is undoubtedly important to the laser machining industry, as well as to spectrochemists optimizing this technique. Further research into the fundamental processes occurring during the interaction of light and matter will inevitably continue for a very long time, and although we may never reach a complete understanding, every piece of the puzzle brings us a little closer and opens the door to new and interesting fields of study.

CITED LITERATURE

- [1] R. J. Weiss, *A Brief History of Light and Those Who Lit the Way*, Singapore: World Scientific Publishers, 1996.
- [2] H. Meyer, *A History of Electricity and Magnetism*, Cambridge: MIT Press, 1971.
- [3] D. Volkov, "About a class of solutions of the Dirac equation," *J. Phys.*, vol. 94, no. 3-4, p. 250, 1935.
- [4] J. Schwinger, "On the classical radiation of accelerated electrons," *Phys. Rev.*, vol. 75, p. 1912, 1949.
- [5] H. Alfvén, "Existence of electromagnetic-hydrodynamic waves," *Nature*, vol. 150, p. 405, 1942.
- [6] J. Nuckolls, L. Wood, A. Thiessen and G. Zimmerman, "Laser compression of matter to super-high densities: Thermonuclear (CTR) applications," *Nature*, vol. 239, p. 139, 1972.
- [7] D. A. Cremers and L. J. Radziemski, *Handbook of Laser-Induced Breakdown Spectroscopy*, New York: Wiley, 2006.
- [8] A. Einstein, "Zur quantentheorie der strahlung (On the quantum mechanics of radiation)," *Physikalische Zeitschrift*, vol. 18, p. 121, 1917.
- [9] T. H. Maiman, "Stimulated optical radiation in ruby," *Nature*, vol. 187, p. 493, 1960.
- [10] P. F. Moulton, "Spectroscopic and laser characteristics of Ti:Al₂O₃," *J. Opt. Soc. B*, vol. 3, p. 125, 1986.
- [11] G. E. Cook, "Pulse compression-key to more efficient radar transmission," *IEEE Proc. IRE*, vol. 48, p. 310, 1960.
- [12] D. Strickland and G. Mourou, "Compression of amplified chirped optical pulses," *Opt. Comm.*, vol. 56, p. 219, 1985.
- [13] G. S. Voronov and N. B. Delone, "Many-photon ionization of the xenon atom by ruby laser

- radiation," *Sov. Phys. JETP*, vol. 23, no. 1, p. 54, 1966.
- [14] P. Agostini, G. Barget, J. Bonnal, G. Mainfray, C. Manus and J. Morellec, "Multiphoton ionization of hydrogen and rare gases," *IEEE J. Quant. Elec.*, vol. 4, no. 10, p. 667, 1968.
- [15] T. J. McIlrath, P. H. Bucksbaum, R. R. Freeman and M. Bashansky, "Above-threshold ionization processes in xenon and krypton," *Phys. Rev. A*, vol. 35, p. 4611, 1987.
- [16] R. R. Freeman and P. H. Bucksbaum, "Investigations of above-threshold ionization using subpicosecond laser pulses," *J. Phys. B: At. Mol. Opt. Phys.*, vol. 24, p. 325, 1991.
- [17] P. Agostini, F. Fabre, G. Mainfray, G. Petite and N. K. Rahman, "Free-free transitions following six-photon ionization of xenon atoms," *Phys. Rev. Lett.*, vol. 42, p. 1127, 1979.
- [18] P. Kruit, J. Kimman, H. G. Muller and M. J. van der Wiel, "Electron spectra from multiphoton ionization of xenon at 1064, 532, and 440 nm," *Phys. Rev. A*, vol. 28, p. 248, 1983.
- [19] L. V. Keldysh, "Ionization in the field of a strong electromagnetic wave," *Sov. Phys. JETP*, vol. 20, no. 5, p. 1307, 1965.
- [20] S. Augst, D. Strickland, D. Meyerhofer, S. Cin and J. Eberly, "Tunneling ionization of noble gases in a high-intensity laser field," *Phys. Rev. Lett.*, vol. 63, p. 2212, 1989.
- [21] T. Auguste, P. Monot, L.-A. Lompre, G. Mainfray and C. Manus, "Multiply charged ions produced in noble gases by a 1 ps laser pulse at 1053 nm," *J. Phys. B: At. Mol. Phys. Opt. Phys.*, vol. 25, p. 4181, 1992.
- [22] P. Gibbon, *Short Pulse Laser Interactions with Matter*, London: Imperial College Press, 2005.
- [23] W. L. Kruer, *The Physics of Laser Plasma Interactions*, New York: Addison-Wesley, 1988.
- [24] F. F. Chen, *Introduction to Plasma Physics*, New York: Plenum Press, 1974.
- [25] L. Spitzer, *Physics of Fully Ionized Gases*, New York: Interscience Publishers, 1962.
- [26] A. A. Vlasov, "On the vibrational properties of an electron gas," *Sov. Phys. JETP*, vol. 8, no. 3, p. 291, 1938.
- [27] K. G. Estabrook, E. J. Valeo and W. L. Kruer, "Two-dimensional relativistic simulations of resonance absorption," *Phys. Fluids*, vol. 18, p. 1151, 1975.

- [28] D. Forslund, J. Kindel, K. Lee, E. Lindman and R. L. Morse, "Theory and simulation of resonant absorption in a hot plasma," *Phys. Rev. A*, vol. 11, p. 679, 1975.
- [29] O. L. Landen, D. G. Sterns and E. M. Campbell, "Measurement of the expansion of picosecond laser-produced plasmas using resonance absorption profile spectroscopy," *Phys. Rev. Lett.*, vol. 63, p. 1475, 1989.
- [30] L. Tonks and I. Langmuir, "Oscillations in ionized gases," *Phys. Rev.*, vol. 33, p. 195, 1929.
- [31] L. D. Landau, "On the vibrations of the electronic plasma," *J. Phys. (USSR)*, vol. 10, p. 25, 1946.
- [32] J. M. Dawson and C. Oberman, "High-frequency conductivity and the emission and absorption coefficients of a fully ionized plasma," *Phys. Fluids*, vol. 5, p. 517, 1962.
- [33] F. Brunel, "Not-so-resonant, resonant absorption," *Phys. Rev. Lett.*, vol. 59, p. 52, 1987.
- [34] P. Gibbon and A. R. Bell, "Collisionless absorption in sharp-edged plasmas," *Phys. Rev. Lett.*, vol. 68, p. 1535, 1992.
- [35] Q. L. Dong, J. Zhang and H. Teng, "Absorption of femtosecond laser pulses in interaction with solid targets," *Phys. Rev. E*, vol. 64, p. 026411, 2001.
- [36] M. K. Grimes, A. R. Rundquist, Y. S. Lee and M. C. Downer, "Experimental identification of "vacuum heating" at femtosecond-laser-irradiated metal surfaces," *Phys. Rev. Lett.*, vol. 82, p. 4010, 1999.
- [37] A. A. Andreev, J. Limpouch and A. N. Semakhin, "Absorption of the energy of a short laser pulse obliquely incident on a highly inhomogeneous plasma," *Bull. Russ. Acad. Sci.*, vol. 58, p. 1056, 1994.
- [38] E. S. Weibel, "Anomalous skin effect in a plasma," *Phys. Fluids*, vol. 10, p. 741, 1967.
- [39] A. A. Andreev, E. G. Gamaliy, V. N. Novikov and V. T. Semakhin, "Heating of a dense plasma by an ultrashort laser pulse in the anomalous skin-effect regime," *Sov. Phys. JETP*, vol. 74, p. 963, 1992.
- [40] W. Rozmus and V. T. Tikhonchuk, "Skin effect and interaction of short laser pulses with dense plasmas," *Phys. Rev. A*, vol. 42, p. 7401, 1990.
- [41] S. K. Sundaram and E. Mazur, "Inducing and probing non-thermal transitions in semiconductors using femtosecond laser pulses," *Nature Mater.*, vol. 1, p. 217, 2002.
- [42] Z. Lin, L. V. Zhigilei and V. Celli, "Electron-phonon coupling and electron heat capacity of metals under conditions of strong electron-phonon nonequilibrium," *Phys. Rev. B*, vol. 77, p. 075133,

2008.

- [43] S. Amoruso, R. Bruzzese, N. Spinelli and R. Velotta, "Characterization of laser-ablation plasmas," *J. Phys. B: At. Mol. Opt. Phys.*, vol. 32, p. R131, 1999.
- [44] E. G. Gamaly, A. V. Rode, B. Luther-Davies and V. T. Tikhonchuk, "Ablation of solids by femtosecond laser: Ablation mechanism and ablation thresholds for metals and dielectrics," *Phys. Plasmas*, vol. 9, p. 949, 2002.
- [45] B. N. Chichkov, C. Momma, S. Nolte, F. von Alvensleben and A. Tunnerman, "Femtosecond, picosecond and nanosecond ablation of solids," *Appl. Phys. A*, vol. 63, p. 109, 1996.
- [46] X. Liu, D. Du and G. A. Mourou, "Laser ablation and micromachining with ultrashort laser pulses," *IEEE J. Quantum Electron.*, vol. 33, no. 10, p. 1706, 1997.
- [47] S. J. Rehse, H. Salimnia and A. W. Miziolek, "Laser-induced breakdown spectroscopy (LIBS): an overview of recent progress and future potential for biomedical applications," *J. Med. Eng. Tech.*, vol. 36, no. 2, p. 77, 2012.
- [48] F. Anabitarte, A. Cobo and J. M. Lopez-Higuera, "Laser-induced breakdown spectroscopy: Fundamentals, applications, and challenges," *ISRN Spec.*, p. 285240, 2012.
- [49] J. P. Singh and S. N. Thakur, *Laser-Induced Breakdown Spectroscopy*, Boston: Elsevier, 2007.
- [50] Y. Liu, S. Singha, T. E. Witt, Y. Cheng and R. J. Gordon, "Observation of near total polarization in the ultrafast laser ablation of Si," *Appl. Phys. Lett.*, vol. 93, p. 161502, 2008.
- [51] Y. Zhao, S. Singha, Y. Liu and R. J. Gordon, "Polarization-resolved laser-induced breakdown spectroscopy," *Opt. Lett.*, vol. 34, p. 494, 2009.
- [52] J. S. Penczak, Y. Liu and R. J. Gordon, "Polarization-resolved laser-induced breakdown spectroscopy of Al," *J. Phys. Chem. A*, vol. 113, p. 13310, 2009.
- [53] Y. Liu, J. S. Penczak and R. J. Gordon, "Nanosecond polarization-resolved laser-induced spectroscopy," *Opt. Lett.*, vol. 35, p. 112, 2010.
- [54] E. Majd, A. S. Arabanian and R. Massudi, "Polarization-resolved laser-induced breakdown spectroscopy by single nanosecond pulsed Nd:YAG laser," *Opt. Lasers Eng.*, vol. 48, p. 750, 2010.
- [55] M. E. Asgill, H. Y. Moon, N. Omenetto and D. W. Hahn, "Investigation of polarization effects for nanosecond laser-induced breakdown spectroscopy," *Spectrochim. Acta B*, vol. 65, p. 1033, 2010.

- [56] J. S. Penczak, Y. Liu and R. J. Gordon, "Polarization and fluence dependence of the polarized emission in nanosecond laser-induced breakdown spectroscopy," *Spectrochim. Acta B*, vol. 66, p. 186, 2011.
- [57] Y. Ralchenko, A. E. Kramida and J. Reader, "NIST Atomic Spectra Database," NIST ASD Team, 2012. [Online]. Available: <http://physics.nist.gov/asd> . [Accessed 19 June 2012].
- [58] K. S. Ojha, P. K. Bajpai and R. Gopal, "Reinvestigation of silicon dimer in 360-540 nm region," *Journal of the International Academy of Physical Sciences*, vol. 15, no. 1, p. 105, 2011.
- [59] R. Hergenoder, M. Miclea and V. Hommes, "Controlling semiconductor nanoparticle size distributions with tailored ultrashort pulses," *Nanotechnology*, vol. 17, p. 4065, 2006.
- [60] J. Hermann, S. Noel, T. E. Itina, E. Axente and M. E. Povarnitsyn, "Correlation between ablation efficiency and nanoparticle generation during the short-pulse laser ablation of metals," *Laser Phys.*, vol. 18, p. 374, 2008.
- [61] H. M. Milchberg and J. C. Weisheit, "Polarization of recombination radiation from non-equilibrium plasmas," *Phys. Rev. A*, vol. 26, p. 1023, 1982.
- [62] J. Bonse, G. Bachelier, J. Siegel and J. Solis, "Time and space resolved dynamics of melting, ablation, and solidification phenomena induced by femtosecond laser pulses in germanium," *Phys. Rev. B*, vol. 74, p. 134106, 2006.
- [63] K. Sokolowski-Tinten, J. Bialkowski and D. von der Linde, "Ultrafast laser-induced order-disorder transitions in semiconductors," *Phys. Rev. B*, vol. 51, p. 14186, 1995.
- [64] K. Sokolowski-Tinten, J. Bialkowski, A. Cavalleri, D. von der Linde, A. Oparin, J. Meyer-ter-Vehn and S. I. Anisimov, "Transient states of matter during short pulse laser ablation," *Phys. Rev. Lett.*, vol. 81, p. 224, 1998.
- [65] T. Y. Choi, D. J. Hwang and C. P. Grigoropoulos, "Ultrafast laser-induced crystallization of amorphous silicon films," *Opt. Eng.*, vol. 42, p. 3383, 2003.
- [66] J. P. Callan, A. M.-T. Kim, C. A. Roesner and E. Mazur, "Universal dynamics during and after ultrafast laser-induced semiconductor-to-metal transitions," *Phys. Rev. B*, vol. 64, p. 073201, 2001.
- [67] S. Singha, Z. Hu and R. J. Gordon, "Ablation of materials with dual femtosecond laser pulses," *J. Appl. Phys.*, vol. 104, p. 113520, 2008.

- [68] J. M. Stone, *Radiation and Optics*, New York: McGraw-Hill Book Company, 1963.
- [69] G. E. Jellison Jr. and D. H. Lowndes, "Measurements of the optical properties of liquid silicon and germanium using nanosecond time-resolved ellipsometry," *Appl. Phys. Lett.*, vol. 51, p. 352, 1987.
- [70] N. H. Burnett, H. A. Baldis, M. C. Richardson and G. D. Enright, "Harmonic generation in CO₂-laser target interaction," *Appl. Phys. Lett.*, vol. 31, p. 172, 1977.
- [71] R. L. Carman, D. W. Forslund and J. M. Kindel, "Observation of harmonics in the visible and ultraviolet created in CO₂-laser produced plasmas," *Phys. Rev. A*, vol. 24, p. 2649, 1981.
- [72] R. L. Carman, D. W. Forslund and J. M. Kindel, "Visible harmonic emission as a way of measuring profile steepening," *Phys. Rev. Lett.*, vol. 46, p. 29, 1981.
- [73] T. Engers, W. Fendel, H. Schuler, H. Schulz and D. von der Linde, "Second-harmonic generation in plasmas produced by femtosecond pulses," *Phys. Rev. A*, vol. 43, no. 8, p. 4564, 1991.
- [74] D. von der Linde, H. Schulz, T. Engers and H. Schuler, "Second harmonic generation in plasmas produced by intense femtosecond pulses," *IEEE J. Quant. Elec.*, vol. 76, no. 13, p. 2388, 1992.
- [75] M. M. Murnane, H. C. Kapteyn, M. D. Rosen and R. W. Falcone, "Ultrafast X-ray pulses from laser produced plasmas," *Science*, vol. 251, p. 531, 1991.
- [76] U. Teubner, W. Theobald, C. Wulker and E. Forster, "X-ray spectra from high-intensity subpicosecond laser produced plasmas," *Phys. Plasmas*, vol. 2, p. 972, 1995.
- [77] L. Plaja, L. Roso, K. Rzazewski and M. Lewenstein, "Generation of attosecond pulse trains during the reflection of a very intense laser on solid surfaces," *J. Opt. Soc. Am. B*, vol. 15, p. 1904, 1998.
- [78] D. von der Linde, "Generation of high order optical harmonics from solid surfaces," *Appl. Phys. B: Lasers Opt.*, vol. 68, p. 315, 1999.
- [79] W. Theobald, R. Habner, C. Wulker and R. Sauerbrey, "Temporally resolved measurement of electron densities with high harmonics," *Phys. Rev. Lett.*, vol. 77, p. 298, 1996.
- [80] W. Theobald, R. Habner, R. Kingham, R. Sauerbrey, R. Fehr, D. O. Gericke, M. Schlanges, W.-D. Kraeft and K. Ishikawa, "Electron densities, temperatures, and the dielectric function of femtosecond-laser-produced plasmas," *Phys. Rev. E*, vol. 59, p. 3544, 1999.
- [81] U. Teubner, K. Eidmann, U. Wagner, U. Andiel, F. Pisani, G. D. Tsakiris, K. Witte, J. Meyer-ter-Vehn, T. Schlegel and E. Forster, "Harmonic emission from the rear side of thin overdense foils irradiated with intense ultrashort pulses," *Phys. Rev. Lett.*, vol. 92, p. 185001, 2004.

- [82] H. Merdji, P. Salieres, L. Lederoff, J.-F. Hergott, B. Carre, D. Joyeux, D. Descamps, J. Norin, C. Lynga, A. L'Huillier, C.-G. Wahlstrom, M. Bellini and S. Huller, "Coherence properties of high-order harmonics: Applications to high-density laser-plasma diagnostics," *Laser Part. Beams*, vol. 18, p. 495, 2000.
- [83] Y. R. Shen, *The Principles of Nonlinear Optics*, New York: Wiley, 1984.
- [84] Y. Q. Liu, J. Zhang, Z. M. Sheng, X. Y. Peng and Z. Jin, "Absorption and second harmonic emission from interaction of femtosecond laser pulses with microspherical droplets," *Opt. Comm.*, vol. 281, p. 1244, 2008.
- [85] S. V. Bulanov, N. M. Naumova and F. Pegoraro, "Interaction of an ultrashort, relativistically strong laser pulse with an overdense plasma," *Phys. Plasmas*, vol. 1, p. 745, 1994.
- [86] U. Teubner and P. Gibbon, "High-order harmonics from laser-irradiated plasma surfaces," *Rev. Mod. Phys.*, vol. 81, p. 445, 2009.
- [87] D. von der Linde and K. Rzazewski, "High-order optical harmonic generation from solid surfaces," *Appl. Phys. B*, vol. 63, p. 499, 1996.
- [88] A. Ishizawa, T. Kanai, T. Ozaki and H. Kuroda, "Enhancement of high-order harmonic generation efficiency by double pulse lasers," *J. Phys. IV France*, vol. 11, pp. Pr2-369, 2001.
- [89] A. Ishizawa, T. Kanai, T. Ozaki and H. Kuroda, "Enhancement of high-order harmonic generation efficiency from solid-surface plasma by controlling the electron density gradient of picosecond laser-produced plasmas," *IEEE J. Quant. Elec.*, vol. 37, no. 3, p. 384, 2001.
- [90] I. B. Foldes, J. S. Bakos, Z. Bakonyi, T. Nagy and S. Szatmari, "Harmonic generation in plasmas of different density gradients," *Phys. Lett. A*, vol. 258, p. 312, 1999.
- [91] A. S. Sandhu, G. R. Kumar, S. Sengupta, A. Das and P. K. Kaw, "Laser-pulse-induced second-harmonic and hard X-ray emission: Role of plasma-wave breaking," *PRL*, vol. 95, p. 025005, 2005.
- [92] M. Zepf, G. D. Tsakiris, G. Pretzler, I. Watts, D. M. Chambers, P. A. Norreys, U. Andiel, A. E. Dangor, K. Eidmann, C. Gahn, A. Machacek, J. S. Wark and K. Witte, "Role of the plasma scale length in the harmonic generation from solid targets," *Phys. Rev. E*, vol. 58, no. 5, p. R5253, 1998.
- [93] S. Kohlweyer, G. D. Tsakiris, C. -G. Wahlstrom, C. Tillman and I. Mercer, "Harmonic generation from solid-vacuum interface irradiated at high laser intensities," *Opt. Comm.*, vol. 117, p. 431, 1995.

- [94] A. Tarasevitch, A. Orisch, D. von der Linde, P. Balcou, G. Rey, J. -P. Chambaret, U. Teubner, D. Klopfel and W. Theobald, "Generation of high-order spatially coherent harmonics from solid targets by femtosecond lasers," *Phys. rev. A*, vol. 62, p. 023816, 2000.
- [95] R. S. Majoribanks, L. Zhao, F. W. Budnik, G. Kulcsar, A. Vitcu, H. Higaki, R. Wagner, A. Maksimchuk, D. Umstadter, M. C. Downer and M. C. Downer, "Laser-plasma harmonics with high-contrast pulses and designed pulses," *Doanld Umstadter Publications*, vol. Paper 61, p. 342, 1998.
- [96] L. A. Gizzi, D. Giulietti, A. Giulietti, P. Audebert, S. Bastiani, J. P. Geindre and A. Mysyowicz, "Simultaneous measurements of hard X-rays and second-harmonic emission in fs laser-target interactions," *PRL*, vol. 76, no. 13, p. 2278, 1996.
- [97] I. B. Foldes, J. S. Bakos, G. Veres, Z. Bakonyi, T. Nagy and S. Szatmari, "Harmonic generation in a UV laser plasma," *IEEE J. Quant. Elec.*, vol. 2, no. 3, p. 776, 1996.
- [98] R. A. Ganeev, Z. A. Chakera, M. Raguramiya, A. K. Sharma, P. A. Naik and P. D. Gupta, "The study of spectral, temporal, and spatial characteristics of harmonics generated at solid surfaces," *Opt. Spectrosc.*, vol. 89, no. 6, p. 967, 2000.
- [99] R. A. Ganeev, A. Ishizawa, T. Kanai, T. Ozaki and H. Kuroda, "Polarization peculiarities of femtosecond laser induced harmonic generation from solid surface plasma," *Opt. Comm.*, vol. 227, p. 175, 2003.
- [100] G. Veres, J. S. Bakos, I. B. Foldes, K. Gal, Z. Juhasz, G. Kocsis and S. Szatmari, "Polarization of harmonics generated by ultrashort KrF-laser pulses on solid surfaces," *Europhys. Lett.*, vol. 48, no. 4, p. 390, 1999.
- [101] R. A. Ganeev, J. A. Chakera, M. Raghuramaiah, A. K. Sharma, P. A. Naik and P. D. Gupta, "Polarization effects in harmonic generation from solid surfaces," *J. Opt. B: Quantum Semiclass. Opt.*, vol. 3, p. S112, 2001.
- [102] E. Racz, I. B. Foldes, G. Kocsis, G. Veres, K. Eidmann and S. Szatmari, "On the effects of surface rippling on the generation of harmonics in laser plasmas," *Appl. Phys. B*, vol. 82, p. 13, 2006.
- [103] A. Ishizawa, T. Kanai, T. Ozaki and H. Kuroda, "The spatial distribution of high-order harmonics from solid surface plasmas," *IEEE J. Quant. Elec.*, vol. 36, no. 6, p. 665, 2000.
- [104] D. M. Chambers, P. A. Norreys, A. E. Dangor, R. S. Majoribanks, S. Moustazis, D. Neely, S. G. Preston, J. S. Wark, I. Watts and M. Zepf, "Feasibility study of high harmonic generation from short wavelength lasers interacting with solid targets," *Opt. Comm.*, vol. 148, p. 289, 1998.

- [105] P. Blanc, P. Audebert, F. Fallies, J.-P. Geindre, J.-C. Gauthier, A. Dos Santos, A. Mysyrowicz and A. Antonetti, "Phase dynamics of reflected probe pulses from sub-100-fs laser-produced plasmas," *J. Opt. Soc. Am. B*, vol. 13, no. 1, p. 118, 1996.
- [106] C. Quoix, G. Hamoniaux, A. Antonetti, J.-C. Gauthier, J.-P. Geindre and P. Audebert, "Ultrafast plasma studies by phase and amplitude measurements with femtosecond spectral interferometry," *J. Quant. Spectrosc. Radiat. Transfer*, vol. 65, p. 455, 2000.
- [107] R. E. Kidder, in *Proceedings of Japan-U.S. Seminar on Laser Interaction with Matter*, Tokyo, 1975.
- [108] D. W. Forslund, J. M. Kindel, K. Lee, E. L. Lindman and R. L. Morse, "Theory and simulation of resonant absorption in a hot plasma," *Phys. Rev. A*, vol. 11, p. 679, 1975.
- [109] K. G. Estabrook, E. J. Valeo and W. L. Kruer, "Two-dimensional relativistic simulations of resonance absorption," *Phys. Fluids*, vol. 18, p. 1151, 1975.
- [110] P. Gibbon and E. Forster, "Short-pulse laser-plasma interactions," *Plasma Phys. Control. Fusion*, vol. 38, p. 769, 1996.
- [111] U. Teubner, P. Gibbon, E. Forster, F. Fallies and P. Audebert, "Subpicosecond KrF laser plasma interaction at intensities between 10^{14} and 10^{17} W/cm²," *Phys. Plasmas*, vol. 3, p. 2679, 1996.
- [112] F. David and R. Pellat, "Resonant absorption by a magnetic plasma at a rippled critical surface," *Phys. Fluids*, vol. 23, p. 1682, 1980.
- [113] K. Estabrook, "Critical surface bubbles and corrugations and their implications to laser fusion," *Phys. Fluids*, vol. 19, no. 11, p. 1733, 1976.
- [114] R. A. Cairns, "Resonant absorption at a rippled critical surface," *Plasma Phys.*, vol. 20, p. 991, 1978.
- [115] J.-P. Geindre, P. Audebert, A. Rousse, F. Fallies, J.-C. Gauthier, A. Mysyrowicz, A. Dos Santos, G. Hamoniaux and A. Antonetti, "Frequency-domain interferometer for measuring the phase and amplitude of a femtosecond pulse probing a laser-produced plasma," *Opt. Lett.*, vol. 19, no. 23, p. 1997, 1994.
- [116] K. Eidmann, J. Meyer-ter-Vehn, T. Schlegel and S. Huller, "Hydrodynamic simulation of subpicosecond laser interaction with solid-density matter," *Phys. Rev. E*, vol. 62, no. 1, p. 1202, 2000.
- [117] A. Tarasevitch, C. Wunsche and D. von der Linde, "High-order harmonics from plasma surfaces," in *Strong Field Laser Physics*, New York, Springer Science + Business Media, 2008, p. 301.

- [118] N. Bloembergen, "The influence of electron plasma formation on superbroadening in light filaments," *Opt. Comm.*, vol. 8, no. 4, p. 285, 1973.
- [119] E. Yablonovitch, "Self-phase modulation and short-pulse generation from laser-breakdown plasmas," *Phys. Rev. A*, vol. 10, no. 5, p. 1888, 1974.
- [120] S. C. Rae and K. Burnett, "Detailed simulations of plasma-induced spectral blueshifting," *Phys. Rev. A*, vol. 46, no. 2, p. 1084, 1992.
- [121] W. M. Wood, G. Focht and M. C. Downer, "Tight focusing and blue shifting of millijoule femtosecond pulses from a conical axicon amplifier," *Opt. Lett.*, vol. 13, no. 11, p. 984, 1988.
- [122] H. Varel, D. Ashkenasi, A. Rosenfeld, M. Wahmer and E. Campbell, "Micromachining of quartz with ultrashort pulses," *Appl. Phys. A*, vol. 65, p. 367, 1997.
- [123] A. Marcinkevicius, S. Juodkazis, M. Watanabe, M. Miwa, S. Matsuo, H. Misawa and J. Nishii, "Femtosecond laser-assisted three-dimensional microfabrication in silica," *Opt. Lett.*, vol. 26, no. 5, p. 277, 2001.
- [124] A. A. Voevodin, M. S. Donley and J. S. Zabinski, "Pulsed laser deposition of diamond-like carbon wear protective coatings: a review," *Surf. Coat. Technol.*, vol. 92, no. 1-2, p. 42, 1997.
- [125] M. Okoshi, K. Higashikawa and M. Hanabusa, "Pulsed laser deposition of ZnO thin films using a femtosecond laser," *Appl. Surf. Sci.*, Vols. 154-155, p. 424, 2000.
- [126] D. X. Hammer, G. D. Noojin, R. J. Thomas, C. E. Clary, B. A. Rockwell, C. A. Toth and W. P. Roach, "Intraocular laser surgical probe for membrane disruption by laser-induced breakdown," *Appl. Opt.*, vol. 36, no. 7, p. 1684, 1997.
- [127] A. V. Rode, E. G. Gamaly, B. Luther-Davies, B. T. Taylor, J. Dawes, A. Chan, R. M. Lowe and P. Hannaford, "Subpicosecond laser ablation of dental enamel," *J. Appl. Phys.*, vol. 92, p. 2153, 2002.
- [128] J. Scaffidi, J. Pender, W. Pearman, S. R. Goode, B. W. Colston Jr, J. C. Carter and S. M. Angel, "Dual-pulse laser-induced breakdown spectroscopy with combinations of femtosecond and nanosecond lasers," *Appl. Opt.*, vol. 42, p. 6099, 2003.
- [129] K. L. Eland, D. N. Stratis, D. M. Gold, S. R. Goode and S. M. Angel, "Energy dependence of emission intensity and temperature in LIBS plasma using femtosecond excitation," *Appl. Spectrosc.*, vol. 55, p. 286, 2001.

- [130] J. Scaffidi, S. M. Angel and D. A. Cremers, "Emission enhancement mechanism in dual-pulse LIBS," *Anal. Chem.*, vol. 78, p. 24, 2006.
- [131] R. E. Russo, X. L. Mao, C. Liu and J. Gonzalez, "Laser assisted plasma spectrochemistry: Laser ablation," *J. Anal. At. Spectrom.*, vol. 19, p. 1084, 2004.
- [132] J. B. Sirven, B. Bousquet, L. Canioni and L. Sarger, "Time-resolved and time-integrated single-shot laser-induced plasma experiments using nanosecond and femtosecond laser pulses," *Spectrochim. Acta Part B*, vol. 59, p. 1033, 2004.
- [133] F. Colao, V. Lazic, R. Fantoni and S. Pershin, "A comparison of single and double pulse laser-induced breakdown spectroscopy of aluminum samples," *Spectrochim. Acta Part B*, vol. 57, p. 1167, 2002.
- [134] Z. Hu, S. Singha, Y. Liu and R. J. Gordon, "Mechanism for the ablation of Si(111) with pairs of ultrashort laser pulses," *Appl. Phys. Lett.*, vol. 90, p. 131910, 2007.
- [135] S. Singha, R. J. Gordon and Z. Hu, "Fluorescence enhancement ratio dropdown at low fluences during femtosecond double pulse laser ablation," *Chin. Phys. Lett.*, vol. 25, no. 7, p. 2653, 2008.
- [136] V. Pinon, C. Fotakis, G. Nicolas and D. Anglos, "Double pulse laser-induced breakdown spectroscopy with femtosecond laser pulses," *Spectrochim. Acta Part B*, vol. 63, p. 1006, 2008.
- [137] V. Pinon and D. Anglos, "Optical emission studies of plasma induced by single and double femtosecond laser pulses," *Spectrochim. Acta Part B*, vol. 64, p. 950, 2009.
- [138] J. Guo, T. Wang, J. Shao, T. Sun, R. Wang, A. Chen, Z. Hu, M. Jin and D. Ding, "Emission enhancement ratio of the metal irradiated by femtosecond double-pulse laser," *Opt. Comm.*, vol. 285, p. 1895, 2012.
- [139] S. Noel, E. Axente and J. Hermann, "Investigation of plumes produced by material ablation with two time-delayed femtosecond laser pulses," *Appl. Surf. Sci.*, vol. 255, p. 9738, 2009.
- [140] V. I. Babushok, F. C. DeLucia Jr, J. L. Gottfried, C. A. Munson and A. W. Miziolek, "Double pulse laser ablation and plasma: Laser induced breakdown spectroscopy signal enhancement," *Spectrochim. Acta Part B*, vol. 61, p. 999, 2006.
- [141] S. Amoruso, R. Bruzzese, X. Wang, G. O'connell and J. G. Lunney, "Multidiagnostic analysis of ultrafast laser ablation of metals with pulse pair irradiation," *J. Appl. Phys.*, vol. 108, p. 113302, 2010.

- [142] M. Spyridaki, E. Koudoumas, P. Tzanetakis, C. Fotakis and R. Stoian, "Temporal pulse manipulation and ion generation in ultrafast laser ablation of silicon," *Appl. Phys. Lett.*, vol. 83, p. 1474, 2003.
- [143] E. Koudoumas, M. Spyridaki, R. Stoian, A. Rosenfeld, P. Tzanetakis, I. V. Hertel and C. Fotakis, "Influence of pulse temporal manipulation on the properties of laser ablated Si ion beams," *Thin Solid Films*, Vols. 453-454, p. 372, 2004.
- [144] T. Donnelly, J. G. Lunney, S. Amoruso, R. Bruzzese and X. Wang, "Double pulse ultrafast laser ablation of nickel in vacuum," *J. Appl. Phys.*, vol. 106, p. 013304, 2009.
- [145] T. Y. Choi and C. P. Grigoropoulos, "Plasma and ablation dynamics in ultrafast laser processing of crystalline silicon," *J. Appl. Phys.*, vol. 92, p. 4918, 2002.
- [146] M. E. Povarnitsyn, T. E. Itina, K. V. Khishchenko and P. R. Levashov, "Suppression of ablation in femtosecond double pulse experiments," *Phys. Rev. Lett.*, vol. 103, p. 195002, 2009.
- [147] T. Y. Choi, D. J. Hwang and C. P. Grigoropoulos, "Femtosecond laser induced ablation of crystalline silicon upon double beam irradiation," *Appl. Surf. Sci.*, Vols. 197-198, p. 720, 2002.
- [148] I. H. Chowdhury, X. Xu and A. M. Weiner, "Ultrafast double-pulse ablation of fused silica," *Appl. Phys. Lett.*, vol. 86, p. 151110, 2005.
- [149] Y. Ralchenko, A. E. Kramida and J. Reader, "NIST Atomic Spectra Database," NIST ASD Team, 2012. [Online]. Available: <http://physics.nist.gov/asd>. [Accessed 20 March 2013].
- [150] D. von der Linde and K. Sokolowski-Tinten, "The physical mechanisms of short-pulse laser ablation," *Appl. Surf. Sci.*, Vols. 154-155, p. 1, 2000.
- [151] K. Oguri, Y. Okano, T. Nishikawa and H. Nakano, "Dynamics of femtosecond laser ablation studied with time-resolved x-ray absorption fine structure imaging," *Phys. Rev. B*, vol. 79, p. 144106, 2009.
- [152] X. Xu, C. Cheng and I. Chowdhury, "Molecular dynamics study of phase change mechanisms during femtosecond laser ablation," *J. Heat Trans.*, vol. 126, p. 727, 2004.
- [153] P. Lorazo, L. J. Lewis and M. Meunier, "Thermodynamic pathways to melting, ablation and solidification in absorbing solids under pulsed irradiation," *Phys. Rev. B*, vol. 73, p. 134108, 2006.
- [154] J. Hohlfeld, S.-S. Wellershoff, J. Gudde, U. Conrad, V. Jahnke and E. Matthias, "Electron and lattice dynamics following optical excitation of metals," *Chem. Phys.*, vol. 251, p. 237, 2000.

- [155] A. Semerok and C. Dutouquet, "Ultrashort double pulse laser ablation of metals," *Thin Solid Films*, Vols. 453-454, p. 501, 2004.
- [156] D. E. Roberts, A. du Plessis and L. R. Botha, "Femtosecond laser ablation of silver foil with single and double pulses," *Appl. Surf. Sci.*, vol. 256, p. 1784, 2010.

VITA

NAME

- John S. Penczak

EDUCATION

- B.S., Chemistry, Illinois State University, Normal, Illinois, 2006.
- B.S., Physics, Illinois State University, Normal, Illinois, 2006.
- Ph.D., Physical Chemistry, University of Illinois at Chicago, 2013.

ASSISTANTSHIPS

- Teaching Assistantship, University of Illinois at Chicago, 2007-2009
- Research Assistantship, University of Illinois at Chicago, 2009-2013

HONORS

- Dean's Scholar Award, University of Illinois at Chicago, 2010-2011

PROFESSIONAL MEMBERSHIPS

- American Chemical Society
- Society for Applied Spectroscopy

PUBLICATIONS

- 1.) Penczak, John S.; Liu, Yaoming; and Gordon, Robert J., "Polarization Resolved Laser-Induced Breakdown Spectroscopy of Al," Journal of Physical Chemistry A. 113, 13310-13317, 2009.
- 2.) Liu, Yaoming; Penczak, John S.; and Gordon, Robert J., "Nanosecond and Femtosecond Polarization Resolved Laser-Induced Breakdown Spectroscopy (PRLIBS) of Aluminum," in Conference on Lasers and Electro-Optics/International Quantum Electronics Conference, Optical Society of America, 2009.
- 3.) Liu, Yaoming; Penczak, John S.; and Gordon, Robert J., "Nanosecond Polarization-Resolved Laser-Induced Breakdown Spectroscopy," Optics Letters, 35, 112-114, 2010.
- 4.) Penczak, John S.; Liu, Yaoming; and Gordon, Robert J., "Polarization and Fluence Dependence of the Polarized Emission in Nanosecond Laser-Induced Breakdown Spectroscopy," Spectrochimica Acta B, 66, 186-188, 2011.
- 5.) Penczak, John S.; Liu, Yaoming; Schaller, Richard. D; Rich, Daniel H.; Gordon, Robert J.; "The mechanism for continuum polarization in laser induced breakdown spectroscopy," Spectrochimica Acta B, 74-75, 3-10, 2012.

VITA(continued)

PRESENTATIONS

(CONFERENCE POSTERS)

- 1.) Penczak, John S.; Liu, Yaoming; and Gordon, Robert J. "Controlling the Polarized Emission of a Laser-Generated Plasma," Poster presented at the Gordon Research Conference: Quantum Control of Light and Matter at Mount Holyoke College, 2009.
- 2.) Liu, Yaoming; Singha, Sima; Witt, Tana E.; Zhao, Youbo; Penczak, John S.; and Gordon, Robert J. "Observation of a Giant Polarization Effect in the Ultrafast Laser Ablation of Si," University of Illinois at Chicago Student Poster Session, 2009.
- 3.) Penczak, John S.; Liu, Yaoming; and Gordon, Robert J. "Nanosecond and Femtosecond Polarization-Resolved Laser Induced Breakdown Spectroscopy," American Chemical Society Conference in San Francisco, March, 2010.
- 4.) Penczak, John S.; Liu, Yaoming; and Gordon, Robert J. "Nanosecond and Femtosecond Polarization-Resolved Laser Induced Breakdown Spectroscopy," Applied Spectroscopy Student Poster Session at University of Illinois at Chicago, April, 2010.
- 5.) Penczak, John S.; Liu, Yaoming; and Gordon, Robert J. "Nanosecond and Femtosecond Polarization-Resolved Laser Induced Breakdown Spectroscopy," University of Illinois at Chicago Student Poster Session, April, 2011.